REPORT DOCUMENTATION PAGE

Form Approved
OMB No. 0704-0188

1. AGENCY USE ONLY (Leave blank)	2. REPORT DATE	3. REPORT TYPE AND DATES COVERED
	28 July 97	Final 01 Nov 94 - 31 May 97

4. TITLE AND SUBTITLE
Flowfield Dependent Mixed Explicit - Implicit (FDMEI) Algorithm Toward

5. FUNDING NUMBERS
F49620 — 95-1-0006

6. AUTHOR(S)
T. J. Chung

AFOSR-TR-97
0327

7. PERFORMING ORGANIZATION NAME(S) AND ADDRESS(ES)
University of Alabama Huntsville
Huntsville, AL 35899

9. SPONSORING / MONITORING AGENCY NAME(S) AND ADDRESS(ES)
Air Force Office Of Scientific Research
Aerospace & Materials Sciences Directorate
110 Duncan Avenue, Suite B-115
Bolling AFB DC 20332-0001
NA

10. SPONSORING / MONITORING AGENCY REPORT NUMBER
95-1-0006

11. SUPPLEMENTARY NOTES

12a. DISTRIBUTION / AVAILABILITY STATEMENT
APPROVED FOR PUBLIC RELEASE
DISTRIBUTION IS UNLIMITED

12b. DISTRIBUTION CODE

19971002 013

13. ABSTRACT *(Maximum 200 words)*

This report covers the results of the research on new concepts and formulations aimed toward direct numerical simulation(DNS) dealing with high speed flows. The research was motivated by the fact that it is desirable to develop a CFD program which can be applied to all speed regimes, both compressible and incompressible, both viscous and inviscid, and both laminar and turbulent flows, ideal for shock wave turbulent boundary layer interactions in hypersonics. The popular notion that DNS will resolve all turbulent microscales can be applied to incompressible flows. For compressible flows with shock waves interacting with turbulent boundary layers, however, difficulties arise in dealing with complex physical phenomena such as transition from laminar to turbulent flows, relaminalization, interactions between viscous and inviscid flows, and high temperature gradients close to the wall, particularly in hypersonics. No currently available CFD techniques are capable of resolving these physical phenomena simultaneously even in DNS.

14. SUBJECT TERMS
DNS, Turbulence

15. NUMBER OF PAGES
83

16. PRICE CODE

17. SECURITY CLASSIFICATION OF REPORT	18. SECURITY CLASSIFICATION OF THIS PAGE	19. SECURITY CLASSIFICATION OF ABSTRACT	20. LIMITATION OF ABSTRACT
U	U	U	Unlimited

FLOWFIELD-DEPENDENT MIXED EXPLICIT-IMPLICIT(FDMEI) ALGORITHM TOWARD DIRECT NUMERICAL SIMULATION IN HIGH SPEED FLOWS

T. J. Chung
Department of Mechanical & Aerospace Engineering
The University of Alabama in Huntsville

SUMMARY

This report covers the results of the research on new concepts and formulations aimed toward direct numerical simulation(DNS) dealing with high speed flows. The research was motivated by the fact that it is desirable to develop a CFD program which can be applied to all speed regimes, both compressible and incompressible, both viscous and inviscid, and both laminar and turbulent flows, ideal for shock wave turbulent boundary layer interactions in hypersonics. The popular notion that DNS will resolve all turbulent microscales can be applied to incompressible flows. For compressible flows with shock waves interacting with turbulent boundary layers, however, difficulties arise in dealing with complex physical phenomena such as transition from laminar to turbulent flows, relaminalization, interactions between viscous and inviscid flows, and high temperature gradients close to the wall, particularly in hypersonics. No currently available CFD techniques are capable of resolving these physical phenomena simultaneously even in DNS.

The purpose of the FDMEI approach is to overcome these difficulties by introducing the flowfield-dependent implicitness parameters which are ***calculated*** from changes of Mach numbers, Reynolds numbers, Peclet numbers, and Damköhler numbers(if reacting) between adjacent nodal points and between time steps. These implicitness parameters imply current flowfields changing in space and time designed to alter the magnitudes of every term in the Navier-Stokes system of equations, reflecting the parabolic, hyperbolic, and elliptic nature of the actual flowfield. For example, far away from the wall, the initial form of the Navier-Stokes system of equations automatically changes into a hyperbolic form of the Euler equations as dictated by the flowfiel-dependent implicitness parameters. By the same token, the viscous terms become activated as boundary layers are approached and they become dominant close to the wall, again automatically dictated by the flowfield-dependent implicitness parameters. Such phenomena can be clearly observed when the contours of these flowfield-dependet implicitness parameters are plotted, which are shown to be representative of the flowfield themselves.

The essence of the FDMEI scheme is to follow the physics and as a result the numerics are generated accordingly. This is contrary to all other existing computational schemes in which numerics are predetermined for the fixed physics under investigation. Unfortunately, howevser, physics change significantly as a function of space and time for which the predetermined numerics are no longer suitable. This occurs when the program desinged for incompressible flows is to cope with compressible flows in different regions of the domain and vise versa, or for laminar flows to handle turbulent flows and vise versa.. Such computational schemes will not be successful even in DNS mech refinements. The emphasis of FDMEI is upon not only the ability to deal with all situations of fluid dynamical physics but also the computational accuracy if and when the computer is available for DNS calculations. In the mean time, the FDMEI approach can be used for non-DNS problems with accuracy much superior to any other CFD methods available today.

The results of the research on FDMEI are summarized in three journal publications attached herein.

1. Yoon, K. T. and Chung, T. J., "Three Dimensional Mixed Explicit-Implicit Generalized Galerkin Spectral Element Methods for High-Speed Turbulent Compressible Flows", Computer Methods in Applied Mechanics and Engineering, Vol. 135, pp 343-367, 1996.

2. Chung, T. J., "A New Computational Approach with Flowfield-Dependent Implicitness Algorithm for Applications to Supersonic Combustion", in Avanced Computational and Analysis of Combustion, Ed. G. D. Roy, S. M. Frolov, and P. Givi, Moscow: ENAS Publishers, pp. 466-489, 1997.

3. Yoon, K. T., Moon, S. Y., Garcia, S. A., Heard, G. W., and Chung, T. J., "Flowfield-Dependent Mixed Explicit-Implicit(FDMEI) Methods for High and Low Speed and Compressible and Incompressible Flows", Computer Methods in Applied Mechanics and Engineering, Vol. 148, 1997.

As a consequence of this research, the following important conslusions and recommendations are provided: (1) As shown in Appendix A of Reference 3 above, the FEMEI scheme leads to all existing computational methods if the flowfield-dependent implicitness parameters are fixed to certain arbitrary numbers between zero and one, indicating that all existing methods are the special cases of FDMEI, (2) The FDMEI scheme provides a single computer code which can be applied to all physical phenomena in fluid dynamics, (3) Due to limited computational resources and limited number of research personnel, benchmark validations included only small portions of CFD problems in this report. The future research should include higher Mach numbers and Reynolds numbers, detailed studies of transition to and from turbulent flows, high temperature gradients, compressibility effects, dilatational thermal dissipation, and finally the firm establishment of the FDMEI technology benefiting the CFD community in general.

ELSEVIER

Comput. Methods Appl. Mech. Engrg. 135 (1996) 343–367

Computer methods in applied mechanics and engineering

Three-dimensional mixed explicit–implicit generalized Galerkin spectral element methods for high-speed turbulent compressible flows

K.T. Yoon[1], T.J. Chung*

Department of Mechanical and Aerospace Engineering, The University of Alabama in Huntsville, Huntsville, AL 35899, USA

Received 24 May 1995

Abstract

In high speed flows the interactions of shock waves with turbulent boundary layers are important design considerations because of the complex flowfields resulting in increased adverse pressure gradients, skin friction and temperatures. Unsteadiness and three-dimensional flowfield structure are also characteristic of shock wave turbulent boundary layer interactions. Such physical phenomena require sophisticated numerical schemes in the solution of governing equations. The purpose of this paper, therefore, is to introduce an accurate and efficient approach—the Mixed Explicit–Implicit Generalized Galerkin Spectral Element Method (MEI-GG-SEM) with Legendre polynomial spectral elements in which flowfield dependent implicitness parameters provide automatically adequate computational requirements for compressible and incompressible flows or high speed and low speed flows. This is in contrast to the traditional approach in which all-speed-regime analysis requires a separate hyperbolic-elliptic pressure equation for pressure correction if the flow becomes incompressible. In the MEI-GG-SEM scheme, mesh refinements are carried out adaptively until shock waves are resolved, followed then by the adaptive increase of Legendre polynomial degrees until turbulence microscales are resolved, in which the traditional turbulence modeling is no longer required, aimed toward direct numerical simulation. In order to demonstrate the validity of the theory and numerical procedure, two-dimensional flat plate and compression corner high speed flows are investigated, followed by a three-dimensional sharp leading edged fin for swept shock wave turbulent boundary layer interactions. Comparisons of the present study with experimental measurements and other numerical studies show favorable agreement.

1. Introduction

The last decade has seen unprecedented technological innovations in computational fluid dynamics, prompted particularly by the increase in technical requirements of aerospace research. Namely, the flowfields due to high velocities, compressibility, shock waves, turbulence and high temperature have been the focus of intensive research in the past [1–9].

When shock waves interact with turbulent boundary layers in external or internal flows, special considerations are required due to widely disparate time and length scales, corresponding to different physical phenomena—namely, turbulence microscales and shock wave surface discontinuities. Here, we are faced with the smallest time and length scales which may severely affect the computational requirements. To cope with such requirements, various numerical strategies have been developed using finite difference methods (FDM) and finite element methods (FEM). Incorporated or implemented into either FDM or FEM are the finite volume methods (FVM) and spectral element methods (SEM).

* Corresponding author. UA System Distinguished Professor.
[1] Graduate Research Assistant.

PII S0045-7825(96)01066-3

Modeling of turbulence has been the controversial subject. Closure models, probability density functions (PDF), large eddy simulation (LES), direct numerical simulation (DNS) and other methods have been reported.

The purpose of the present study is to introduce an unstructured adaptive spectral element method in dealing with combined turbulence and shock waves for both internal and external flows of aerospace vehicles. This work is motivated by the fact that DNS can be achieved via adaptive h-p methods, combining the mesh refinement (h-method) with spectral polynomial degrees of freedom (p-method). It is well known that the most crucial aspect of turbulent flows is microscales involved in boundary layers (viscous sublayer, buffer zone and turbulent core). This is where the spectral polynomial degrees of freedom can be increased as desired since the mesh refinement alone is incapable of resolving the microscale requirements. In this way, turbulence modeling techniques can be avoided. Furthermore, the current practice in DNS to use extensive refinements in finite difference discretization may also be avoided. Babuska and his co-workers [10–13] and Oden and his co-workers [14–17] contributed to the advancement of FEM h-p adaptive methods. Their applications have not been extended to shock waves interacting with turbulent boundary layers. In what follows, the p-version of the finite element method is referred to as the spectral element method with Legendre polynomials. Although the term 'spectral element method' was used by other investigators, the basic approach in the present study is significantly different from the earlier work [25–27].

Chung and his co-workers [18–24] have studied finite element strategies as applied to shock wave turbulent boundary layer interactions in non-reacting and reacting flows. The main emphasis in the present study is to establish the basic theory and computational strategies of MEI-GGM involved in the Legendre polynomial spectral element method and to present preliminary computational results. Development of theory and formulation include irregular node connectivity of Legendre polynomials of various orders. Comparisons with experimental results have demonstrated superiority of the direct numerical simulation over the standard K-ε model with compressibility effects [19, 20]. One of the most important aspects of the proposed method is the mixed explicit–implicit (MEI) scheme in which flowfield dependent implicitness parameters as calculated from local Mach number and Reynolds number provide automatic adjustments of computational processes required for compressible and incompressible flows or high speed and low speed flows. This is in contrast to other computational schemes in which the hyperbolic-elliptic pressure equation must be solved separately to provide pressure corrections when the compressible flow becomes incompressible.

In what follows we discuss the governing equations and solutions of Navier–Stokes system of equations via Mixed Explicit–Implicit Generalized Galerkin Methods (MEI-GGM) in Section 2, direct numerical simulation with spectral element methods in Section 3, calculations of DNS perturbation variables in Section 4, calculations of flowfield-dependent implicitness parameters in Section 5, numerical applications in Section 6, and conclusions in Section 7.

2. Governing equations and solutions of Navier–Stokes system of equations

A convenient form of governing equations for compressible viscous flows may be written in terms of conservation variables as follows:

$$\frac{\partial \boldsymbol{U}}{\partial t}+\frac{\partial \boldsymbol{F}_i}{\partial x_i}+\frac{\partial \boldsymbol{G}_i}{\partial x_i}=\boldsymbol{B} \tag{1}$$

where

$$\boldsymbol{U}=\begin{bmatrix}\rho\\ \rho v_j\\ \rho E\end{bmatrix},\quad \boldsymbol{F}_i=\begin{bmatrix}\rho v_i\\ \rho v_i v_j+p\delta_{ij}\\ (\rho E+p)v_i\end{bmatrix},\quad \boldsymbol{G}_i=\begin{bmatrix}0\\ -\tau_{ij}\\ -\tau_{ij}v_j+q_i\end{bmatrix},\quad \boldsymbol{B}=\begin{bmatrix}0\\ \rho F_j\\ \rho F_j V_j\end{bmatrix}$$

with standard definitions given by

$$\tau_{ij} = \mu\left(v_{i,j} + v_{j,i} - \frac{2}{3} v_{k,k}\delta_{ij}\right) \qquad E = \varepsilon + \frac{1}{2} v_i v_i \qquad \varepsilon = c_p T - p/\rho$$

$$\mu = \mu_\infty \frac{T_\infty + S_0}{T + S_0}\left(\frac{T}{T_\infty}\right)^{3/2} \qquad S_0 = 110\,\mathrm{K} \qquad q_i = -kT_{,i}$$

$$p = \rho RT \qquad k = \frac{c_p \mu}{Pr}$$

The solution of governing equations will be carried out using the generalized Galerkin approach with test and trial functions given by isoparametric and Legendre polynomials by means of mixed explicit–implicit schemes. In general, explicit schemes are inexpensive but less accurate in comparison with implicit schemes for regions of high pressure or velocity gradients. In case of rapid variations of gradients throughout the domain, it is often desirable to devise a scheme in which implicitness can be adjustable in accordance with gradients, more implicit for the region of high gradients and less implicit or fully explicit for the region of low gradients. It is our objective to obtain amounts of explicitness and implicitness based on the flowfield dependent parameters such as TVD limiters in FDM.

To this end, we expand U^{n+1} in Taylor series about U^n by introducing the implicitness parameters s_1 and s_2 for the first and second derivatives of U with respect to time [18–20], respectively.

$$U^{n+1} = U^n + \Delta t \frac{\partial U^{n+s_1}}{\partial t} + \frac{\Delta t^2}{2}\frac{\partial^2 U^{n+s_2}}{\partial t^2} + O(\Delta t^3) \tag{2}$$

with

$$\frac{\partial U^{n+s_1}}{\partial t} = \frac{\partial U^n}{\partial t} + s_1 \frac{\partial \Delta U^{n+1}}{\partial t} \qquad 0 \leq s_1 \leq 1 \tag{3a}$$

$$\frac{\partial^2 U^{n+s_2}}{\partial t^2} = \frac{\partial^2 U^n}{\partial t^2} + s_2 \frac{\partial^2 \Delta U^{n+1}}{\partial t^2} \qquad 0 \leq s_2 \leq 1 \tag{3b}$$

Substituting (3) into (2) yields

$$\Delta U^{n+1} = \Delta t\left(\frac{\partial U^n}{\partial t} + s_1 \frac{\partial \Delta U^{n+1}}{\partial t}\right) + \frac{\Delta t^2}{2}\left(\frac{\partial^2 U^n}{\partial t^2} + s_2 \frac{\partial^2 \Delta U^{n+1}}{\partial t^2}\right) + O(\Delta t^3) \tag{4}$$

It follows from (1) that

$$\frac{\partial U}{\partial t} = -\frac{\partial F_i}{\partial x_i} - \frac{\partial G_i}{\partial x_i} + B \tag{5}$$

Here, F_i is a function of U and G_i is a function of U and its gradient $U_{,k}$ so that we denote the convective Jacobian a_i, dissipative Jacobian b_i and dissipative gradient Jacobian c_{ik} as

$$a_i = \frac{\partial F_i}{\partial U} \qquad b_i = \frac{\partial G_i}{\partial U} \qquad c_{ik} = \frac{\partial G_i}{\partial U_{,k}}$$

Note that if the source term B includes variables such as reaction rates then it would be necessary to consider the source term Jacobian.

The second derivative of U with respect to time may now be written in terms of these Jacobians.

$$\frac{\partial^2 U}{\partial t^2} = (a_i + b_i)\frac{\partial}{\partial x_i}\left(\frac{\partial F_j}{\partial x_j} + \frac{\partial G}{\partial x_j} - B\right) + c_{ik}\frac{\partial^2}{\partial x_i\,\partial x_k}\left(\frac{\partial F_j}{\partial x_j} + \frac{\partial G_j}{\partial x_j} - B\right) \tag{6}$$

Substituting (5) and (6) into (4) and neglecting the third-order spatial derivatives associated with c_{ik} yield

$$\Delta U^{n+1} = \Delta t\left[-\frac{\partial F_i^n}{\partial x_i} - \frac{\partial G_i^n}{\partial x_i} + B^n - s_1\left(\frac{\partial \Delta F_i^{n+1}}{\partial x_i} + \frac{\partial \Delta G_i^{n+1}}{\partial x_i} - \Delta B^{n+1}\right)\right] + \frac{\Delta t^2}{2}\left[(a_i + b_i)\frac{\partial}{\partial x_i}\left(\frac{\partial F_j^n}{\partial x_j} + \frac{\partial G_j^n}{\partial x_j} - B^n\right) + s_2(a_i + b_i)\frac{\partial}{\partial x_i}\left(\frac{\partial \Delta F_j^{n+1}}{\partial x_j} + \frac{\partial \Delta G_j^{n+1}}{\partial x_j} - \Delta B^{n+1}\right)\right] + O(\Delta t^3) \tag{7}$$

In order to provide implicitness to diffusion behavior differently from convection, we reassign s_1 and s_2 associated with G_i, respectively, as follows

$$s_1\,\Delta G_i \;\Rightarrow\; s_3\,\Delta G_i \qquad s_2\,\Delta G_i \;\Rightarrow\; s_4\,\Delta G_i \tag{8a,b}$$

with the various implicitness parameters defined as

s_1 = first-order convection implicitness parameter

s_2 = second-order convection implicitness parameter

s_3 = first-order diffusion implicitness parameter (8c)

s_4 = second-order diffusion implicitness parameter

The roles of these implicitness parameters are significant, closely related to the flowfield such Mach numbers and Reynolds numbers. This subject will be elaborated upon in Section 5.

Substituting (8a,b) into (7) leads to the residual, neglecting the source term B,

$$R = \Delta U^{n+1} - s_1\,\Delta t\,a_i\frac{\partial \Delta U^{n+1}}{\partial x_i} + s_3\,\Delta t\left(b_i\frac{\partial \Delta U^{n+1}}{\partial x_i} + c_{ij}\frac{\partial^2 \Delta U^{n+1}}{\partial x_i\,\partial x_j}\right) - s_2\frac{\Delta t^2}{2}(a_i a_j + b_i a_j)\frac{\partial^2 \Delta U^{n+1}}{\partial x_i\,\partial x_j} - s_4\frac{\Delta t^2}{2}(a_i b_j + b_i b_j)\frac{\partial^2 \Delta U^{n+1}}{\partial x_i\,\partial x_j} + \Delta t\left(\frac{\partial F_j^n}{\partial x_j} + \frac{\partial G_j^n}{\partial x_j}\right) - \frac{\Delta t^2}{2}\left\{(a_i + b_i)\frac{\partial}{\partial x_i}\left(\frac{\partial F_j^n}{\partial x_j} + \frac{\partial G_j^n}{\partial x_j}\right)\right\} + O(\Delta t^3) = 0 \tag{9}$$

where all Jacobians a_i, b_i and c_{ij} are assumed to remain constant spatially within each time step and to be updated at subsequent time steps.

The Galerkin integral of (9) may now be carried out as follows [21]:

$$\int_\Omega \Phi_\alpha R(U, F_i, G_i)\,d\Omega = 0 \tag{10}$$

where Φ_α refers to the global isoparametric corner node test functions, and the conservation variables are interpolated by the trial functions Φ_α as

$$U(x,t) = \Phi_\alpha(x)U_\alpha(t) \qquad F_i(x,t) = \Phi_\alpha(x)F_{\alpha i}(t) \qquad G_i(x,t) = \Phi_\alpha(x)G_{\alpha i}(t) \tag{11}$$

Substituting (11) into (9) and (10) yields

$$(A_{\alpha\beta}\delta_{rs} + B_{\alpha\beta rs})\,\Delta U_{\beta s}^{n+1} = H_{\alpha r}^n + N_{\alpha r}^n \tag{12}$$

with

$$A_{\alpha\beta} = \int_\Omega \Phi_\alpha \Phi_\beta\,d\Omega$$

$$B_{\alpha\beta rs} = \int_\Omega \left\{\Delta t[-s_1 a_{irs}\Phi_{\alpha,i}\Phi_\beta - s_3(b_{irs}\Phi_{\alpha,i}\Phi_\beta + c_{ijrs}\Phi_{\alpha,i}\Phi_{\beta,j})] + \frac{\Delta t^2}{2}[s_2(a_{irq}a_{jqs} + b_{irq}a_{jqs}) + s_4(a_{irq}b_{jqs} + b_{irq}b_{jqs})]\Phi_{\alpha,i}\Phi_{\beta,j}\right\} d\Omega + \int_\Gamma \left\{\Delta t\,\overset{*}{\Phi}_\alpha[s_1 a_{irs}\overset{*}{\Phi}_\beta - s_3(b_{irs}\overset{*}{\Phi}_\beta + c_{ijrs}\overset{*}{\Phi}_{\beta,j})] - \frac{\Delta t^2}{2}\overset{*}{\Phi}_\alpha[s_2(a_{irq}a_{jqs} + b_{irq}a_{jqs}) + s_4(a_{irq}b_{jqs} + b_{irq}b_{jqs})]\overset{*}{\Phi}_{\beta,j}\right\} n_i\,d\Gamma$$

$$H^n_{\alpha r} = \int_\Omega \left\{ \Delta t[\Phi_{\alpha,i}\Phi_\beta(F^n_{\beta ir} + G^n_{\beta ir}) + \Phi_\alpha \Phi_\beta B^n_{\beta r}] - \frac{\Delta t^2}{2}(a_{irs} + b_{irs})[\Phi_{\alpha,i}\Phi_{\beta,j}(F^n_{\beta js} + G^n_{\beta js}) - \Phi_{\alpha,i}\Phi_\beta B^n_{\beta r}] - \frac{\Delta t}{2}\Phi_\alpha \Phi_\beta B^n_{\beta r} \right\} d\Omega$$

$$N^n_{\alpha r} = -\int_\Gamma \overset{*}{\Phi}_\alpha \left[\Delta t(F^n_{ir} + G^n_{ir}) - \frac{\Delta t^2}{2}(a_{irs} + b_{irs})(F^n_{js,j} + G^n_{js,j}) \right] n_i \, d\Gamma$$

where $\overset{*}{\Phi}_\alpha$ indicates the Neumann boundary interpolation function with unity if applied and zero otherwise. Note also that boundary terms in $B_{\alpha\beta rs}$ are assembled only into boundary nodes of $B_{\alpha\beta rs}$. For three dimensions, $i, j, k = 1, 2, 3$ associated with the Jacobian imply directional identification of each Jacobian matrix (a_1, a_2, a_3, b_1, b_2, b_3, c_{11}, c_{12}, c_{13}, c_{21}, c_{22}, c_{23}, c_{31}, c_{32}, c_{33}) with $r, s = 1, 2, 3, 4, 5$ denoting entries of each of the 5×5 Jacobian matrices. It should be warned, however, that these Jacobian matrices must be multiplied precisely as dictated by summing through repeated indices, not through matrix multiplications as a whole. Indices can be reduced similarly for 2-D.

It is interesting to note that all implicitness parameters can be shown to be functions of flowfields between upstream and downstream, and that the covection implicitness parameters s_1 and s_2 associated with the first term in $B_{\alpha\beta rs}$ are analogous to the total variation diminishing (TVD) limiters in the FDM literature (see Appendix A). With an adequate choice of these implicitness parameters, acceptable resolutions of shock waves have been verified.

On the other hand, the diffusion implicitness parameters s_3 and s_4 are capable of alleviating and accommodating the stiffness involved in turbulent diffusion or finite rate chemistry (if reacting). No analogy can be shown since they do not exist in other numerical schemes. It should also be noted that interactions between convection and diffusion are achieved by means of the terms associated with the products $a_{irq}b_{jqs}$ and $b_{irq}a_{jqs}$. These terms are particularly important for shock wave turbulent boundary layer interactions where the effect of convection upon diffusion and vice versa is crucial in order to resolve turbulence microscales as disturbed by shock wave interactions. We shall refer to these terms as convection–diffusion interaction terms.

If the high speed compressible flow far from the wall becomes the low speed incompressible flow in the vicinity of the wall, we question how pressure can be calculated where the perfect gas law is no longer valid. To this end we integrate the steady state incompressible momentum equation

$$\int \left(p + \frac{1}{2}\rho v_j v_j \right)_{,i} dx_i = \int (\mu v_{i,jj} + \rho \epsilon_{ijk} v_j \omega_k) \, dx_i$$

or

$$p + \frac{1}{2}\rho v_i v_i = P_0 + Q \tag{13}$$

where P_0 is the constant of integration and

$$Q = \frac{1}{n}\int (\mu v_{i,jj} + \rho \epsilon_{ijk} v_j \omega_k) \, dx_i \quad (n = \text{spatial dimension})$$

where ω_i is the component of vorticity vector. Eq. (13) as related to the perfect gas law leads to

$$P_0 = \rho(c_p T - E + v_i v_j) - Q \tag{14a}$$

or

$$P_0 = \rho RT + \frac{1}{2}\rho v_i v_i - Q \tag{14b}$$

If the constant of integration or stagnation pressure as given by (14) indeed remains constant, then this implies that the compressible flow has turned into an incompressible flow. If P_0 as calculated from (14) does not remain a constant, then the incompressible flow has been changed back to compressible flow.

This approach allows the use of the conservation form of the Navier–Stokes system of equations throughout the domain with compressible and incompressible elements being treated accordingly via flowfield dependent implicitness parameters without resorting to the separate hyperbolic-elliptic pressure equation for pressure correction when the flow becomes incompressible.

3. DNS via unstructured spectral element methods (*h-p* version)

Our objective here is to resolve time and length scales involved in turbulence interacting with shock waves using adaptive unstructured *h-p* finite elements, refered to as spectral element methods. One approach is to refine the mesh (*h*-methods) until further refinement is unproductive, at which time the spectral degrees of freedom (*p*-methods) are increased in order to reduce errors as desired, such as in the region of turbulent viscous sublayer. However, the more desirable approach is to optimize between the mesh refinement and spectral orders. Thus, the most crucial aspect of the *h-p* methods is to determine the best possible change in the mesh structure to reduce the local error to a minimum. Should h (mesh size) be decreased or should p (polynomial or spectral degrees of freedom) be increased? Although some work in optimization between the *h*- and *p*-processes has been reported [14–16], the subject of optimization appears to be an open question. Thus, our approach in this study is to refine the mesh until shock waves are adequately computed and then resort to the *p*-version with higher-order Legendre polynomials in order to resolve turbulence microscales. Toward this end, the error indicator θ may be defined in terms of density for shock waves and velocity for turbulence. Some of the options are given as follows:

$$\theta = h \overset{\max}{\Omega_e} |\rho|_{H^2} / |\rho|_{H^1} \tag{15a}$$

$$\theta = h \overset{\max}{\Omega_e} |v_i|_{H^2} / |v_i|_{H^1} \tag{15b}$$

where h is the mesh parameter and various Sobolev space (H^m) seminorms are defined as

$$|\rho|_{H^1} = \left(\int_{\Omega_e} \frac{\partial \rho}{\partial x_i} \frac{\partial \rho}{\partial x_i} \, d\Omega \right)^{1/2} \qquad |\rho|_{H^2} = \left(\int_{\Omega_e} \frac{\partial^2 \rho}{\partial x_i \, \partial x_j} \frac{\partial^2 \rho}{\partial x_i \, \partial x_j} \, d\Omega \right)^{1/2} \tag{16a}$$

$$|v_i|_{H^1} = \left(\int_{\Omega_e} \frac{\partial v_i}{\partial x_j} \frac{\partial v_i}{\partial x_j} \, d\Omega \right)^{1/2} \qquad |v_i|_{H^2} = \left(\int_{\Omega_e} \frac{\partial^2 v_i}{\partial x_j \, \partial x_k} \frac{\partial^2 v_i}{\partial x_j \, \partial x_k} \, d\Omega \right)^{1/2} \tag{16b}$$

The choice among these options depends on various physical aspects of the given problem, whether local errors are dominated by density, velocity components, their gradients, or second derivatives. For the purpose of the examples dealt with in Section 6, we utilize Eqs. (15a) and (15b) for the *h*-adaptivity associated with shock waves and the *p*-adaptivity associated with turbulent boundary layers, respectively.

Direct numerical simulations for turbulent flows are achieved by higher spectral orders using Legendre polynomials [10–13, 17]. The spectral element interpolation functions for the corner nodes, edge modes, face modes, and interior modes in a three-dimensional 8-node isoparametric element are shown in Fig. 1.

8 corner node isoparametric functions:

$$\Phi_N^{(C)} = \frac{1}{8}(1 + \xi_N \xi)(1 + \eta_N \eta)(1 + \zeta_N \zeta) \tag{17}$$

12 edge mode Legendre polynomial functions:

$$\Phi_m^{(E1)} = \frac{1}{4}(1 - \eta)(1 - \zeta) G_m(\xi) \qquad \Phi_m^{(E2)} = \frac{1}{4}(1 + \xi)(1 - \zeta) G_m(\eta) \quad \text{etc.} \tag{18}$$

with $m = 2, \ldots, q$; $12(q - 1)$ edge modes; $q \geq 2$

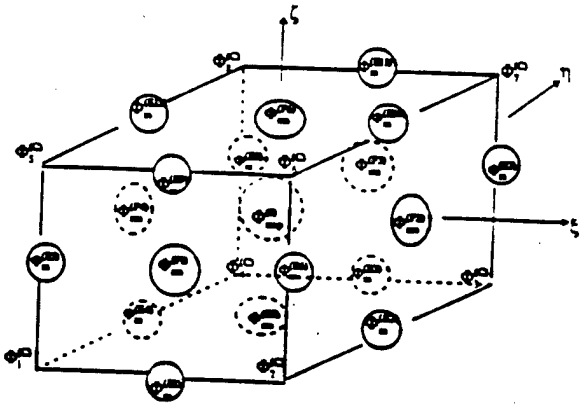

Fig. 1. Spectral element functional representation for Legendre polynomials.

6 face mode Legendre polynomial functions:

$$\Phi_{mn}^{(F1)} = \frac{1}{2}(1-\eta)G_m(\xi)G_n(\zeta) \qquad \Phi_{mn}^{(F2)} = \frac{1}{2}(1+\xi)G_m(\eta)G_n(\zeta) \quad \text{etc.} \tag{19}$$

with $m, n = 2, \ldots, q-2$; $m+n = 4, \ldots, q$; $3(q-2)(q-3)$ face modes; $q \geq 4$

1 interior mode functions (bubble functions):

$$\Phi_{mnp}^{(I)} = G_m(\xi)G_n(\eta)G_p(\zeta) \tag{20}$$

with $m, n, p = 2, \ldots, q-4$; $m+n+p = 6, \ldots, q$; $(q-3)(q-4)(q-5)/6$ interior modes; $q \geq 6$

Here, the highest polynomial order chosen is denoted by q and $G_m(\xi)$ represents the Legendre interpolation functions defined in terms of the Legendre polynomials $L_m(\xi)$,

$$G_m(\xi) = \frac{1}{\sqrt{2(2m-1)}}[L_m(\xi) - L_{m-2}(\xi)] \tag{21}$$

Similar results are obtained for the η and ζ directions. For the purpose of illustration the two-dimensional case of various mixed Legendre polynomial degrees of freedom depicting a possible turbulent microscale distributions is shown in Fig. 2. In addition to the above polynomial space (defined as space 1 (S1) we may use another option of the space (called space 2 (S2)) in which $(q-1)^2$ face modes and $(q-1)^3$ interior modes ($q \geq 2$) are applied [13].

As a consequence of these Legendre polynomials representing the edge, face and interior mode functions, any variable U may be modeled in the form,

$$U = \Phi_N^{(C)} U_N + \Phi_m^{(E)} \hat{U}_m + \Phi_{mn}^{(F)} \hat{U}_{mn} + \Phi_{mnp}^{(I)} \hat{U}_{mnp} \tag{22}$$

where $\hat{U}_m$, $\hat{U}_{mn}$ and $\hat{U}_{mnp}$ are spectral coefficients to be determined by solving the following Galerkin integrals in addition to (11):

$$\int_\Omega \Phi_m^{(E)} R(\Delta U)\, d\Omega = 0 \tag{23a}$$

$$\int_\Omega \Phi_{mn}^{(F)} R(\Delta U)\, d\Omega = 0 \tag{23b}$$

$$\int_\Omega \Phi_{mnp}^{(I)} R(\Delta U)\, d\Omega = 0 \tag{23c}$$

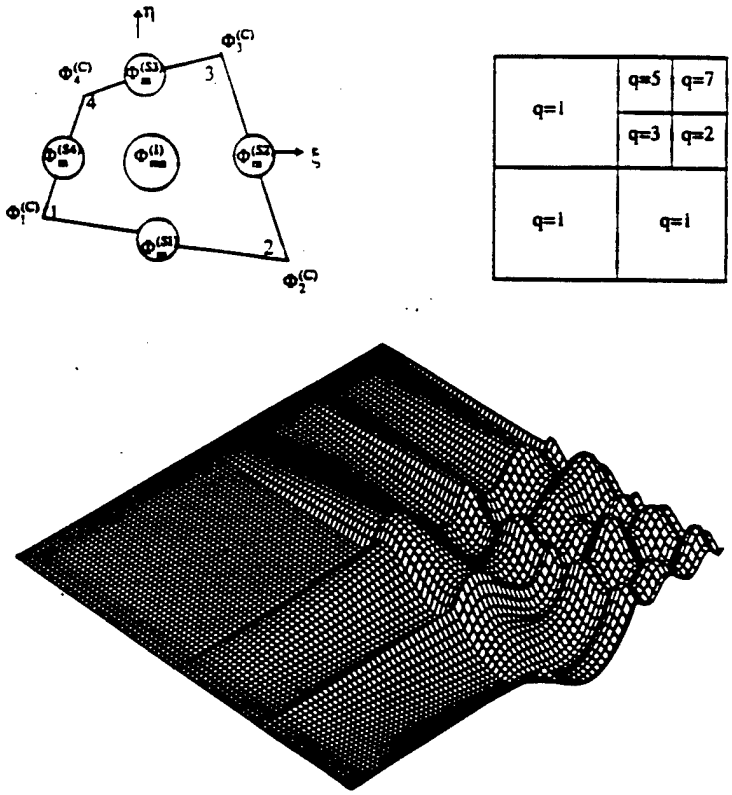

Fig. 2. 2-D Interpolation functions constructed by Legendre polynomial, $\Phi_N^{(C)}$ (corner nodes), $\Phi_m^{(S)}$ (side modes), $\Phi_{mn}^{(I)}$ (interior modes).

Combining (10) and (23a,b,c) leads to the assembled simultaneous algebraic equations in terms of the variables U_α, $\hat{U}_m$, $\hat{U}_{mn}$ and $\hat{U}_{mnp}$.

$$\begin{bmatrix} A_{\alpha\beta}\delta_{rs}+B_{\alpha\beta rs} & A^{\delta}_{\alpha n}\delta_{rs}+B^{\delta}_{\alpha nrs} & A^{\eta}_{\alpha np}\delta_{rs}+B^{\eta}_{\alpha nprs} & A_{\alpha npq}\delta_{rs}+B_{\alpha npqrs} \\ A^{\gamma}_{m\beta}\delta_{rs}+B^{\gamma}_{m\beta rs} & A^{\gamma\delta}_{mn}\delta_{rs}+C^{\gamma\delta}_{mnrs} & A^{\gamma\eta}_{mnp}\delta_{rs}+C^{\gamma\eta}_{mnprs} & A^{\gamma}_{mnpq}\delta_{rs}+C^{\gamma}_{mnpqrs} \\ A^{\xi}_{mk\beta}\delta_{rs}+B^{\xi}_{mk\beta rs} & A^{\xi\delta}_{mkn}\delta_{rs}+C^{\xi\delta}_{mknrs} & A^{\xi\eta}_{mknp}\delta_{rs}+D^{\xi\eta}_{mknprs} & A^{\xi}_{mknpq}\delta_{rs}+D^{\xi}_{mknpqrs} \\ A_{mku\beta}\delta_{rs}+B_{mku\beta rs} & A^{\delta}_{mkun}\delta_{rs}+C^{\delta}_{mkunrs} & A^{\eta}_{mkunp}\delta_{rs}+D^{\eta}_{mkunprs} & A_{mkunpq}\delta_{rs}+E_{mkunpqrs} \end{bmatrix} \times \begin{bmatrix} \Delta U_{\beta s} \\ \Delta\hat{U}^{\delta}_{ns} \\ \Delta\hat{U}^{\eta}_{nps} \\ \Delta\hat{U}_{npqs} \end{bmatrix}^{n+1} = \begin{bmatrix} W_{\alpha r} \\ \hat{W}^{\gamma}_{mr} \\ \hat{W}^{\xi}_{mkr} \\ \hat{W}_{mkur} \end{bmatrix}^{n} \tag{24}$$

with $\gamma, \delta = 1 \rightarrow 12$; $\xi, \eta = 1 \rightarrow 6$; m, k, u, n, p, q = degrees of freedom from edge, face and interior modes; α, β = corner node variables; r, s = conservation variable degrees of freedom. Explicit forms of integrals are shown in Appendix B.

We may initially consider only the corner node equations,

$$(A_{\alpha\beta}\delta_{rs}+B_{\alpha\beta rs})\,\Delta U^{n+1}_{\beta s} = W^{n}_{\alpha r} \tag{25}$$

In this process the MEI computations are carried out with h-adaptivity until all shock waves are resolved. The next step is to resolve microscales using the spectral portion of the computations

$$\begin{bmatrix} A^{\gamma\delta}_{mn}\delta_{rs} + C^{\gamma\delta}_{mnrs} & A^{\gamma\eta}_{mnp}\delta_{rs} + C^{\gamma\eta}_{mnprs} & A^{\gamma}_{mnpq}\delta_{rs} + C^{\gamma}_{mnpqrs} \\ A^{\xi\delta}_{mkn}\delta_{rs} + C^{\xi\delta}_{mknrs} & A^{\xi\eta}_{mknp}\delta_{rs} + D^{\xi\eta}_{mknprs} & A^{\xi}_{mknpq}\delta_{rs} + D^{\xi}_{mknpqrs} \\ A^{\delta}_{mkun}\delta_{rs} + C^{\delta}_{mkunrs} & A^{\eta}_{mkunp}\delta_{rs} + D^{\eta}_{mkunprs} & A_{mkunpq}\delta_{rs} + E_{mkunpqrs} \end{bmatrix} \begin{bmatrix} \Delta\hat{U}^{\delta}_{ns} \\ \Delta\hat{U}^{\eta}_{nps} \\ \Delta\hat{U}_{npqs} \end{bmatrix}^{n+1} = \begin{bmatrix} \hat{W}^{\gamma}_{mr} \\ \hat{W}^{\xi}_{mkr} \\ \hat{W}_{mkur} \end{bmatrix}^{n} - \begin{bmatrix} X^{\gamma}_{mr} \\ X^{\xi}_{mkr} \\ X_{mkur} \end{bmatrix} \tag{26}$$

where

$$X^{\gamma}_{mr} = (A^{\gamma}_{m\beta}\delta_{rs} + B^{\gamma}_{m\beta rs})\,\Delta U_{\beta s}$$

$$X^{\xi}_{mkr} = (A^{\xi}_{mk\beta}\delta_{rs} + B^{\xi}_{mk\beta rs})\,\Delta U_{\beta s}$$

$$X_{mkur} = (A_{mku\beta}\delta_{rs} + B_{mku\beta rs})\,\Delta U_{\beta s}$$

which act as source terms or coupling effect of the corner nodes upon spectral behavior through edge, face and interior modes. The final step is to combine (25) and (26) by

$$(A_{\alpha\beta}\delta_{rs} + B_{\alpha\beta rs})\,\Delta U^{n+1}_{\beta s} = W^{n}_{\alpha r} - Y_{\alpha r} \tag{27}$$

with

$$Y_{\alpha r} = (A^{\delta}_{\alpha n}\delta_{rs} + B^{\delta}_{\alpha nrs})\,\Delta\hat{U}^{\delta}_{ns} + (A^{\eta}_{\alpha np}\delta_{rs} + B^{\eta}_{\alpha nprs})\,\Delta\hat{U}^{\eta}_{nps} + (A_{\alpha npq}\delta_{rs} + B_{\alpha npqrs})\,\Delta\hat{U}_{npqs}$$

Thus, the convergence toward shock wave turbulent boundary layer interactions can be achieved through iterations between (26) and (27). Note that in this process, the convection implicitness parameters s_1 and s_2 are held constant whereas the diffusion implicitness parameters s_3 and s_4 are updated through Reynolds numbers.

Our objective here is to satisfactorily simulate turbulent microscales within an element. All edge, face and interior mode interpolation functions vanish at the corner nodes but exhibit high frequency variations according to the order of Legendre polynomials along the edges, faces and interior domain. It is intended that such Legendre polynomial microscales be capable of simulating the physical microscales of turbulence which are involved in viscous sublayer, buffer zone and turbulent core. The *h*-adaptivity alone is severely limited and naturally we seek a remedy of this situation in the *h-p* adaptivity utilizing the adequate spectral orders required for accuracy. Irregular nodes (hanging nodes) which arise in the process of *h*-adaptivity are treated similarly as in [14]. Furthermore, the advantage of Legendre polynomials is an ease in dealing with edge, face and interior modes which do not require specification of nodes physically located in the element. This is especially beneficial for edge and face modes in establishing boundary continuities. Continuity of variables and gradients along the inter-element boundaries is to be dictated by the higher-order polynomials between the two adjacent elements.

For two-dimensional applications, edge and face modes are merged to side modes as shown in Fig. 2. Consequently, the matrix equation (24) can be reduced so that only side and interior modes are retained.

4. DNS perturbation variables

It is well known that DNS is expected to provide information in turbulence microscale levels at the expense of excessive refinements of domain discretization [6]. The purpose of the present study is, instead, to avoid such refinements by means of implementing high spectral Legendre polynomial orders. The Navier–Stokes solver as introduced here allows unsteady time accurate solutions from which perturbation variables (f') can be calculated as the difference between the Navier–Stokes solution (f) and its time average $\bar{f}$ [22, 23],

$$f' = f - \bar{f} \tag{28}$$

This computation can be conducted throughout the Navier–Stokes integration time steps or upon arrival at quasi-steady state. Strictly speaking, in shock wave turbulent boundary layer interactions a complete steady state is never realized as unsteady eddy motions persist indefinitely, although background flowfields may become steady. This is referred to as the quasi-steady state. The time average of Navier–Stokes solution is performed using the Gaussian quadrature. In this process complicated physical phenomena such as homogeneous and inhomogeneous, isotropic and anisotropic, and non-stationary nature of perturbation flowfields in shock wave turbulent boundary layer interactions can be resolved.

Furthermore, all perturbation variables as calculated from (28) can be transformed via fast Fourier transform to generate power spectral density vs. frequency domain. Various perturbation variables as well as background flowfield data have been examined [24]. As a result of this study, more details of shock wave turbulent boundary layer interactions such as variations of turbulent kinetic energy vs. shock strength, laminar-turbulence transition instability, relaminarization, effects of dilatation, etc., can be rigorously examined in comparison with the previous investigations [6, 28, 29]. Some limited results and discussion of these subjects are presented in [24].

5. Calculations of flowfield-dependent implicitness parameters

The success of the spectral element method (h-p version) described above depends on accurate calculations of flowfield-dependent implicitness parameters. The first-order convection and diffusion implicitness parameters are calculated from the local Mach number and Reynolds number as follows:

$$s_1 = \begin{cases} \min(r, 1) & r \geq \alpha \\ 0 & r < \alpha,\ M_{\min} \neq 0 \\ 1 & M_{\min} = 0 \end{cases} \qquad s_2 = \max(1 - s_1, 0.5) \tag{29}$$

with

$$r = \frac{\Delta M}{M_{\min}} \tag{30}$$

where ΔM is the difference between the maximum and minimum Mach number ($\Delta M = M_{\max} - M_{\min}$) within a finite element, and α is a user-specified small number ($\alpha \cong 0.01$).

$$s_3 = \begin{cases} \min(s, 1) & s \geq \beta \\ 0 & s < \beta,\ \mathrm{Re}_{\min} \neq 0 \\ 1 & \mathrm{Re}_{\min} = 0 \end{cases} \qquad s_4 = \max(1 - s_3, 0.5) \tag{31}$$

with

$$s = \frac{\Delta \mathrm{Re}}{\mathrm{Re}_{\min}} \tag{32}$$

where ΔRe is the difference between the maximum and minimum Reynolds number ($\Delta \mathrm{Re} = \mathrm{Re}_{\max} - \mathrm{Re}_{\min}$) within a finite element and β is a user-specified small number ($\beta \cong 0.01$).

The flowfield dependent implicitness parameters as defined above are capable of allowing various numerical schemes to be automatically generated, as summarized below:

(1) The first-order implicitness parameters s_1 and s_3 control all high gradient phenomena such as shock waves and turbulence. These parameters as calculated from the changes of local Mach numbers and Reynolds numbers within each element are indicative of actual flowfields. The contours of these parameters closely resemble the flowfields themselves, with both s_1 and s_3 being large (close to unity) in which high gradients of variables exist, but small (close to zero) where such gradients are small.

(2) The second-order implicitness parameters s_2 and s_4 are also flowfield dependent. However, their primary role is to provide adequate computational stability (artificial viscosity) as they were originally introduced into the second-order time derivative term of the Taylor series expansion of the conservation flow variables U^{n+1}. Thus, their flowfield dependency is limited by $(s_2, s_4) \geq 0.5$ for adequate computational stability.

(3) The s_1 terms represent convection. This implies that if $s_1 = 0$ then the effect of convection is small. The computational scheme is automatically altered to take this effect into account, with the governing equations being predominantly parabolic.

(4) The s_3 terms are associated with diffusion. Thus, with $s_3 = 0$, the effect of viscosity is small and the computational scheme is automatically switched to that of Euler equations where the governing equations are predominantly hyperbolic.

(5) If the first-order implicitness parameters s_1 and s_3 are non-zero, this indicates a typical situation for hyperbolic, parabolic and elliptic nature of the Navier–Stokes system of equations with convection and diffusion being equally important. This is the case of incompressible flows in low speed. The unique property of the MEI-GGM is its capability to control pressure oscillations adequately without resorting to the separate hyperbolic-elliptic pressure equation for pressure corrections. The capability of MEI-GGM to handle incompressible flows is achieved by a delicate balance between s_1 and s_3 as determined by the local Mach numbers and Reynolds numbers. If the flow is completely incompressible ($M = 0$), the criteria given by (30) leads to $s_1 = 1$, whereas the implicitness parameter s_3 is to be determined according to the criteria given in (32).

6. Application

As benchmark problems two-dimensional shock wave turbulent boundary layer interactions on a flat plate and compressible corner were solved in [31] and demonstrated an excellent comparison with experimental results and other numerical methods [32]. Other benchmark problems including: (1) the flat plate supersonic boundary layer flow, (2) shock wave turbulent boundary layer interactions on a compression corner, and (3) the three-dimensional sharp-leading edged fin for swept-shock wave turbulent boundary layer interactions have been investigated, which are presented below.

6.1. Flat plate supersonic boundary layer flow

Fig. 3 shows a spectral element mesh (gray elements) and the corresponding density contours for Carter's flat plate problem [33]. The spectral elements appear in the boundary layer. The computed wall pressure and skin friction distributions with and without spectral element meshes are compared with Carter's numerical data [33] in Fig. 4. Note that symbols S1 and S2 imply space 1 and space 2

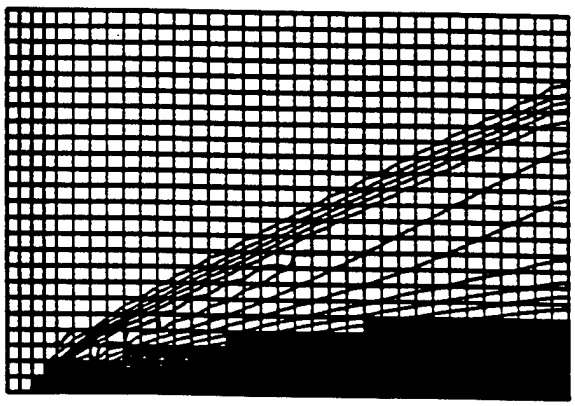

Fig. 3. A spectral mesh (gray elements) and density contours for Carter's flat plate problem with boundary conditions. $M_\infty = 3$, $T_\infty = 390$ R, $T_{wall} = 2.8T_\infty$, $Re_L = 1000$.

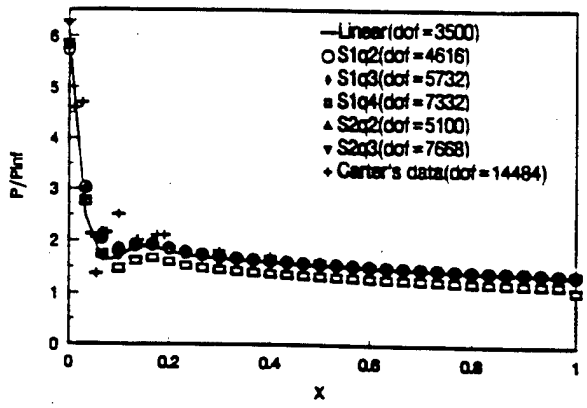

(a) Wall pressure profile for linear and spectral element meshes comparing with Carter's data [33].

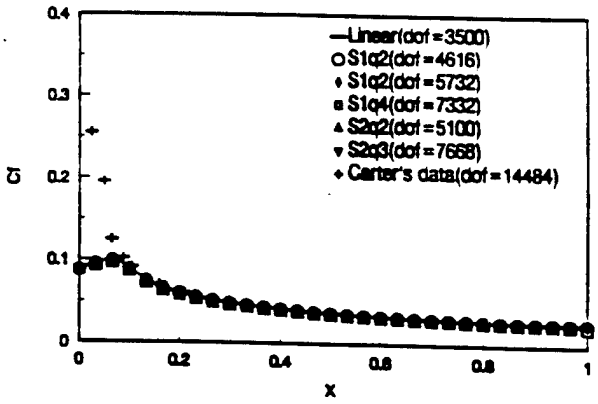

(b) Skin friction profile for linear and spectral element meshes comparing with Carter's data.

Fig. 4. Comparison of wall pressure and skin friction distribution for linear and spectral meshes with Carter's numerical data.

functions of Legendre polynomials, respectively, as defined in Section 4. It is seen that for the laminar flow the spectral element method does provide the results in agreement with other computational methods. However, the spectral elements are more effective when the flowfield contains large gradients in which other computational methods are incapable of resolving large gradients such as in high Reynolds number and high Mach number turbulent flows.

6.2. *Two-dimensional shock wave boundary layer interaction on a compression corner*

In high speed vehicles, deflection of a control surface such as body flaps, elevons and rudders causes the interaction of shock wave with boundary layer, which may cause flow separation, resulting in a significant decrease in flight performance and excessive increase in heating rate. A two-dimensional compression corner experiment by Settles et al. [35] is modeled here as a benchmark problem in shock wave turbulent boundary layer interaction.

Computational geometry and scales corresponding to the experiment are shown in Fig. 5. The freestream conditions are Mach number of 2.85, stagnation pressure of 6.8 atm, stagnation temperature of 268 K, freestream unit Reynolds number of $7.3 \times 10^7/\mathrm{m}$, deflection angle of 16°, and the incoming turbulent boundary layer thickness of 2.3 cm.

Adaptive spectral element mesh configurations are plotted in Fig. 6. The mesh refinement is performed along shock waves while the spectral degree is increased in boundary layer. Convergence of wall pressure for different Legendre polynomial spaces and degrees at $x/\delta = 0.14$ for a typical transient state is plotted in Fig. 7. It appears that the convergence rate of Legendre polynomial space 2 is much

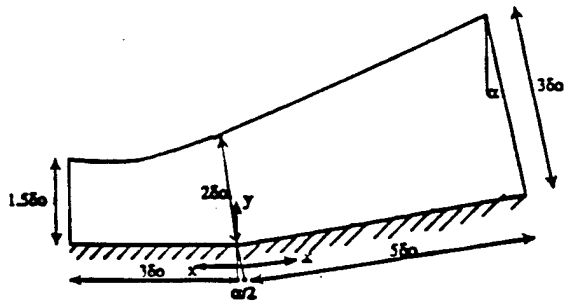

Fig. 5. Computational geometry and scales for 16° compression corner. The freestream conditions corresponding to the Settles' experiment are $M = 2.85$, $P_t = 6.8$ atm, $T_t = 268$ K, $\mathrm{Re}_x = 7.3 \times 10^7$/m, $\delta_0 = 2.3$ cm.

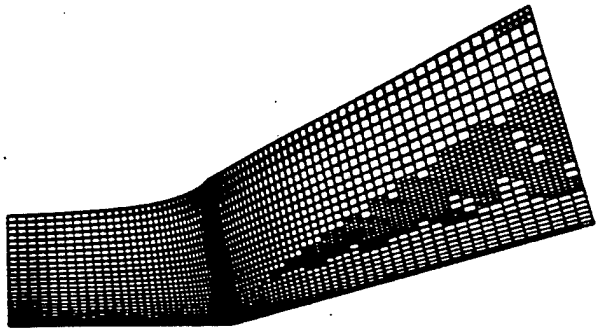

(a) Adaptive mesh configuration (nelem=2558, npoin=2748)

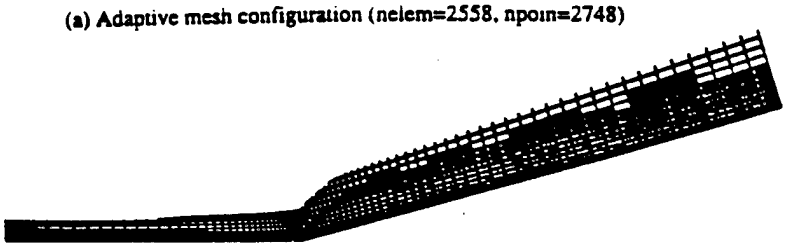

(b) Focus on spectral mesh (gray color) in boundary layer.

Fig. 6. Adaptive spectral element mesh configuration. The mesh is refined along shock waves while the spectral degree is increased in boundary layer.

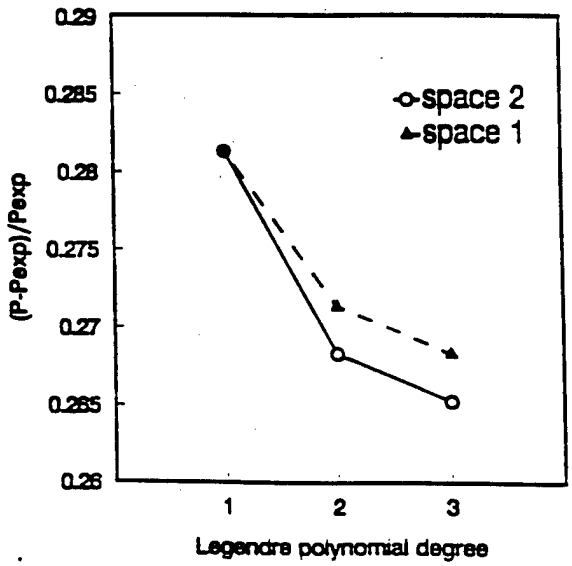

Fig. 7. Convergence of wall pressure for different Legendre polynomial spaces and degrees of $x/\delta = 0.14$ for a typical transient state. It appears that the convergence rate of polynomial space 2 (S2) is much more rapid than that of polynomial space 1 (S1). Also, the higher polynomial degrees are closer to the exact solution, independent of the polynomial spaces.

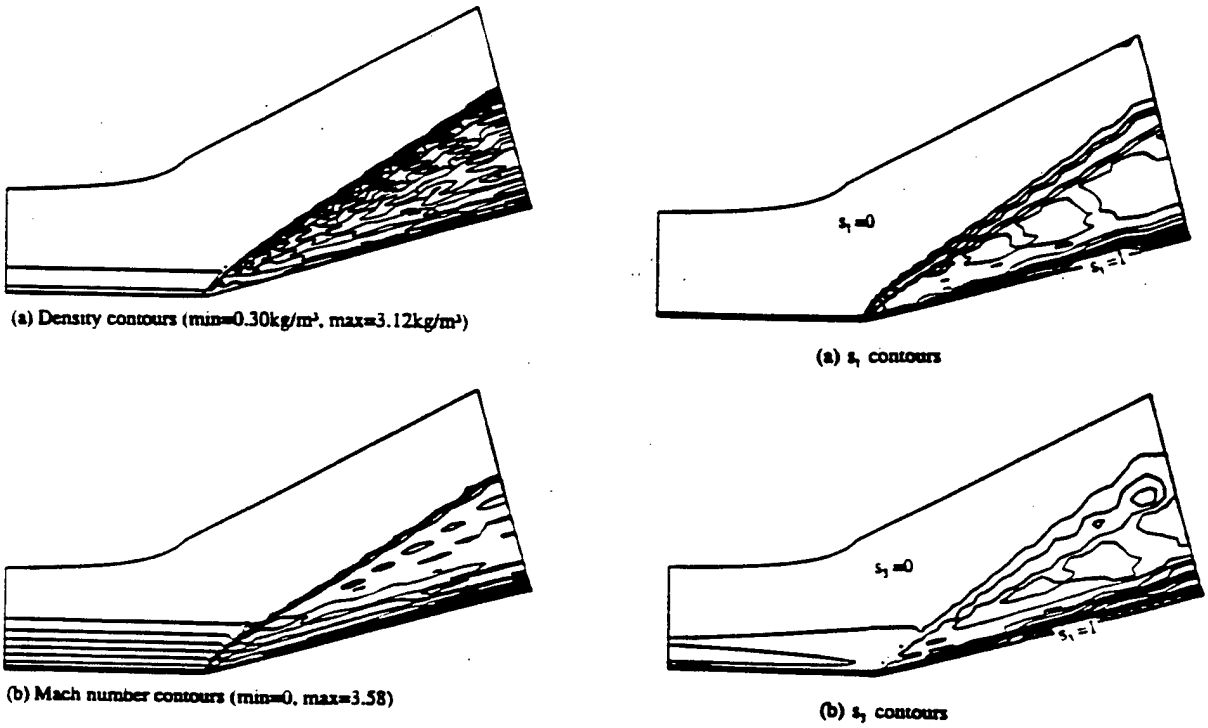

Fig. 8. Density and Mach number contours for shock wave boundary layer interaction on a compression corner.

Fig. 9. First-order convertion and diffusion implicitness parameters (s_1 and s_3) contours. The s_1 and s_3 contours show the trend of flowfield.

more rapid than that of polynomial space 1. Also, the higher polynomial degrees are closer to the exact solution, independent of the polynomial spaces.

Density and Mach number contours are shown in Fig. 8. To show the effect of implicitness parameters upon the flowfield calculations the contours of the first-order implicitness parameters s_1 and s_3 are plotted in Fig. 9. Note that $s_1 = 0$ away from the shock waves and boundary layers, but becomes unity at locations of high gradients (shock waves and boundary layers). By the same token, the implicitness parameter s_3 representing diffusion behaves similarly, being zero and unity at locations of

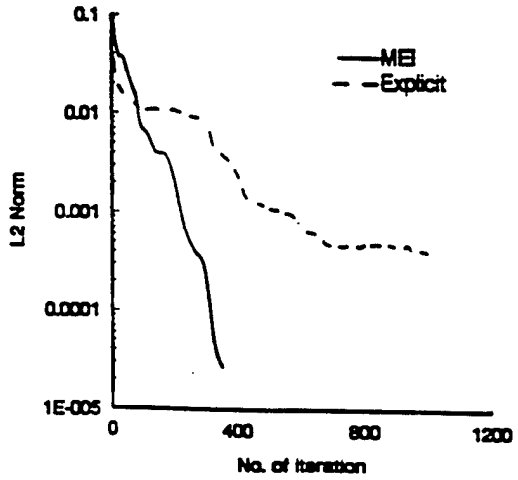

Fig. 10. Convergence history of energy variable for the MEI and explicit schemes. The convergence rate of the MEI scheme is much more rapid than the explicit scheme.

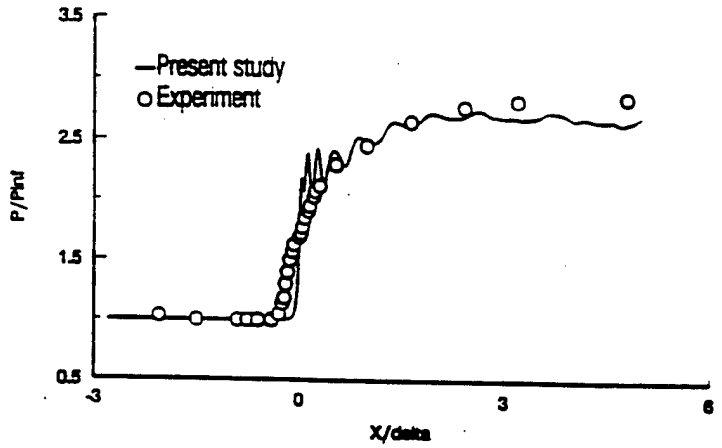

Fig. 11. Comparison of wall pressure for present result and experimental data.

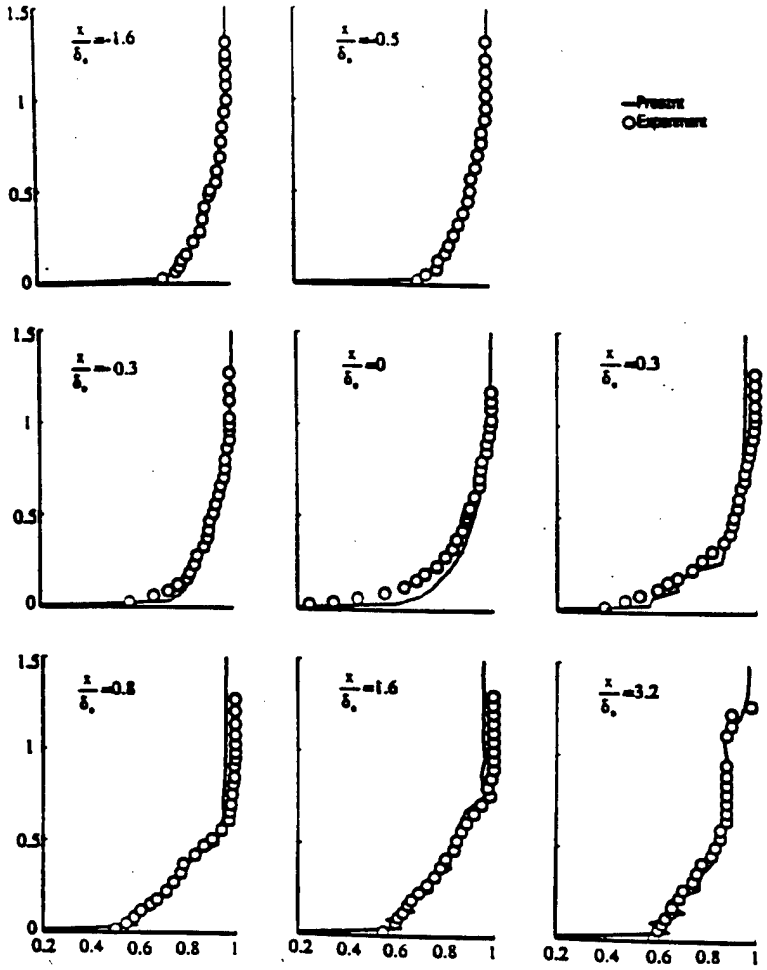

Fig. 12. Comparison of mean streamwise velocity profiles for the present results and Settles' experimental data at several streamwise stations. The plots illustrate the changes in boundary layer velocity profiles. The figure at $x/\delta_0 = 1.6$ is the incoming equilibrium turbulent boundary layer. The location of the shock wave appears as a kink is some velocity profiles downstream of the compression corner. The downstream profiles are seen to recover rapidly from the retarding effects of the imposed adverse pressure gradients.

low gradients and high gradients, respectively. Note that the contours of first-order implicitness parameters s_1 and s_3 resemble the flowfield itself. Here, the second-order implicitness parameters s_2 and s_4, although flowfield dependent to some extent, their primary role is to assure computational stability with their criteria given in (30) and (32). The convergence history of energy variable for MEI and explicit schemes is compared in Fig. 10. The convergence rate of the MEI scheme is much more rapid than the explicit scheme. Fig. 11 shows a comparison of wall pressure for the present study and the Settles' experimental data. It is seen that the present results are in good agreement with the experimental data.

In Fig. 12 mean streamwise velocity profiles are compared with the experimental data at several streamwise stations. The plots serve to illustrate the changes in boundary layer velocity profiles which occur along the length of interaction flowfield. Fig. 12 at $x/\delta_0 = -1.6$ is the incoming equilibrium turbulent boundary layer. The location of the shock wave appears as a kink in some velocity profiles downstream of the compression corner. The downstream profiles are seen to recover rapidly from the retarding effects of the imposed adverse pressure gradients.

6.3. *Three-dimensional shock wave turbulent boundary layer interactions*

The next example is the study of flowfields of a three-dimensional sharp-leading-edged fin for swept shock wave turbulent boundary layer interactions. Fig. 13(a) shows the physical domain for a 3-D sharp fin ($\alpha = 20°$) with a general flowfield structure (Fig. 13(b)) [34]. The inlet boundary conditions and the

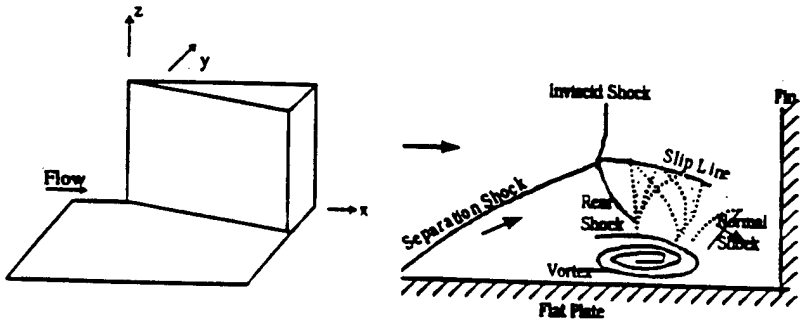

(a) 3-D 20° fin

(b) 20° fin interaction flowfield structures

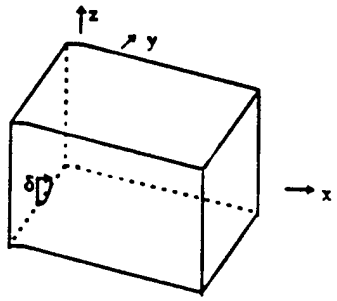

(c) Computational domain

Fig. 13. Computational domain for a 3-D 20° fin and flowfield structure with $M_\infty = 2.93$, $P_\infty = 20.57$ kPa, $T_\infty = 92.39$ K, $Re_\infty = 7 \times 10/\text{m}$. The inlet boundary conditions are obtained from the boundary layer analysis. On the solid surface no slip and adiabatic wall boundary conditions are applied.

corresponding flowfield structure are the same as in [35]. Here, the free stream Mach number and temperature are $M_\infty = 2.93$ and $T_\infty = 92.39$ K, corresponding to the chamber pressure and temperature of 680 kPa and 251 K, respectively, with the Reynolds number of 7×10^8/m. The boundary layer thickness δ_0 at the apex of the fin is 1.4 cm, yielding a Reynolds number $\mathrm{Re}_{\delta_0} = 9.8 \times 10^5$. In order to match the boundary conditions as used for the experiments [35] the flowfield behind the fin is calculated as a flat plate boundary layer such that the computed boundary layer thickness δ_0 is set equal to the experimental value of 1.4 cm. On the solid surfaces no slip and adiabatic wall boundary conditions are applied. On the upper, lateral, and at downstream exit boundaries, the flow variables are set free. Adaptively spaced grid points are 33, 41 and 31 in the streamwise, spanwise and vertical directions, respectively. Spectral elements of Legendre polynomial degree 2 in space 2 are applied in the boundary layer.

Fig. 14 shows the background flowfield based on the geometric configurations and boundary conditions described in Fig. 13, as observed from the front ($x - z$ and $y - z$ faces). As such, no details of the hidden portion are shown. It is noticed that the trend is in reasonable agreement with the results

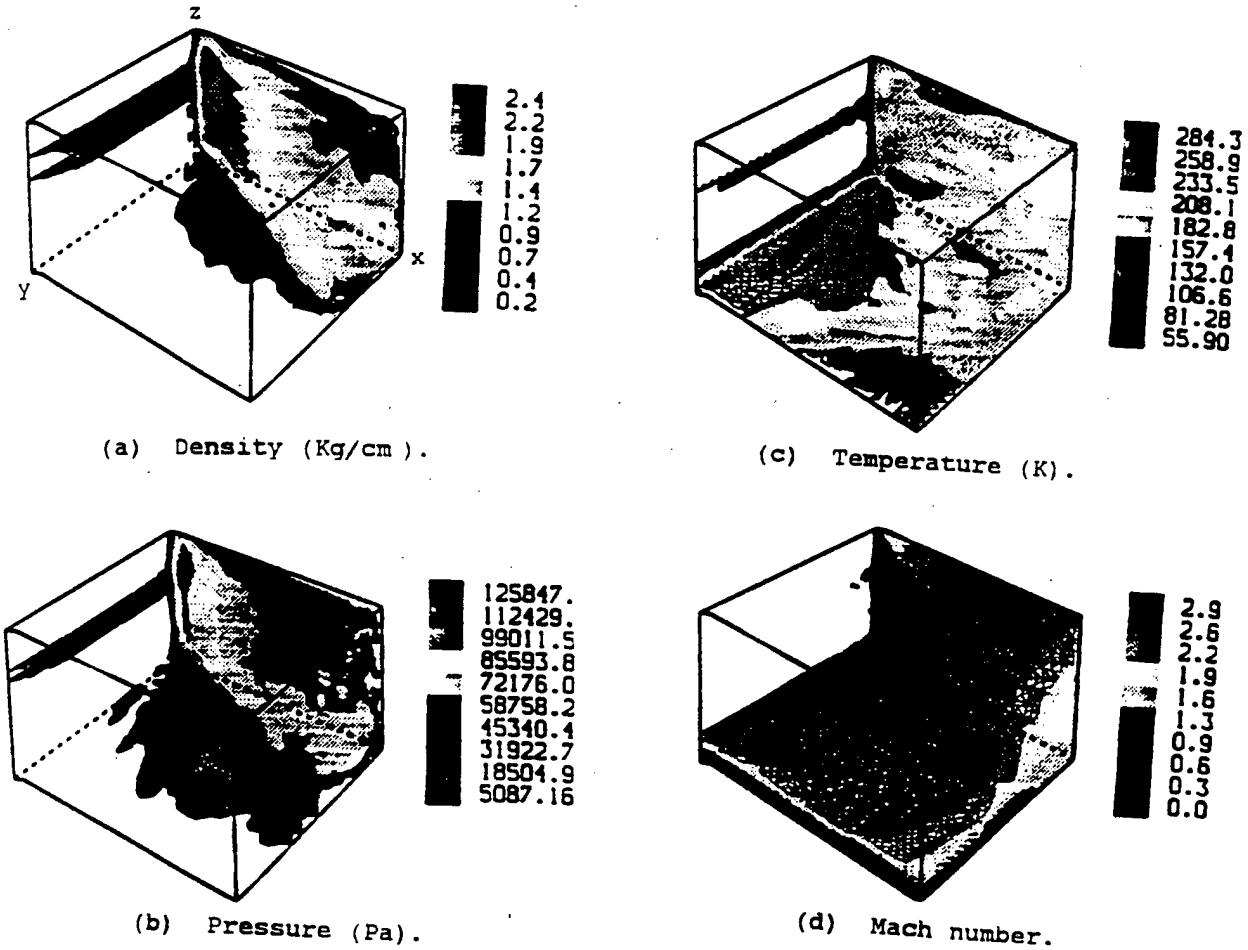

Fig. 14. Background flowfield as observed from the front ($x - z$ plane and $y - z$ plane).

of Narayanswami et al. [36], with density and pressure increasing drastically along the shock waves, the temperature rise being distributed along the flat plate, and Mach number sharply decreasing through the shock waves toward the flat-plate boundary.

Vorticity variations at different planes are shown in Figs. 15–17. The contours of vorticity component in the streamwise planes ($y-z$ planes) in the x-direction with each plane identified as a, b, c, d, e are shown in Fig. 15. The corresponding velocity vectors are plotted on the right-hand side. Clearly, the vortex stretching occurs toward downstream with the evidence of separation shocks, slip lines and vortex centers close to the wall. These physical phenomena become more significant toward downstream in agreement with the skematics shown in Fig. 13(b).

Fig. 16 shows the contours of vorticity component in the spanwise vertical planes ($x\cos\alpha - z$ planes)

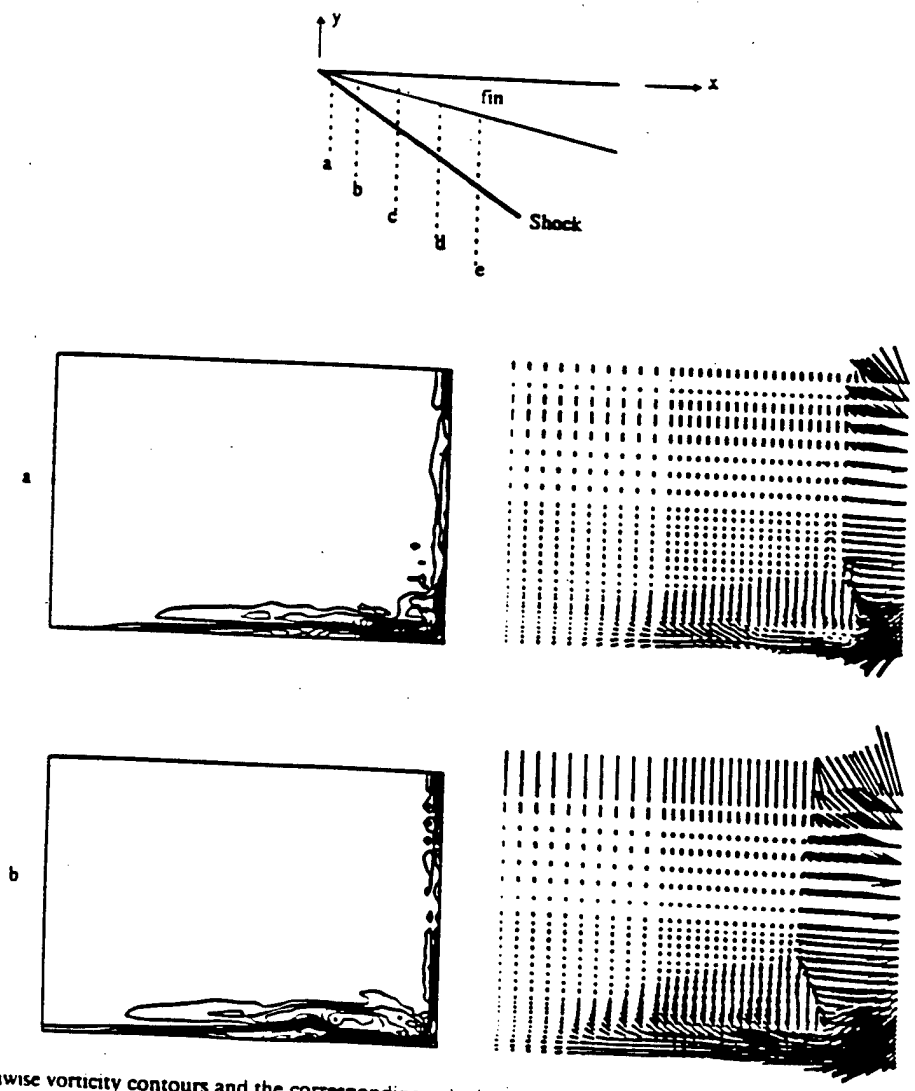

Fig. 15. Streamwise vorticity contours and the corresponding velocity vectors ($t = 0.3965$ ms). The vortex stretching occurs toward downstream with the evidence of separation shocks, slip lines and vortex centers close to the wall.

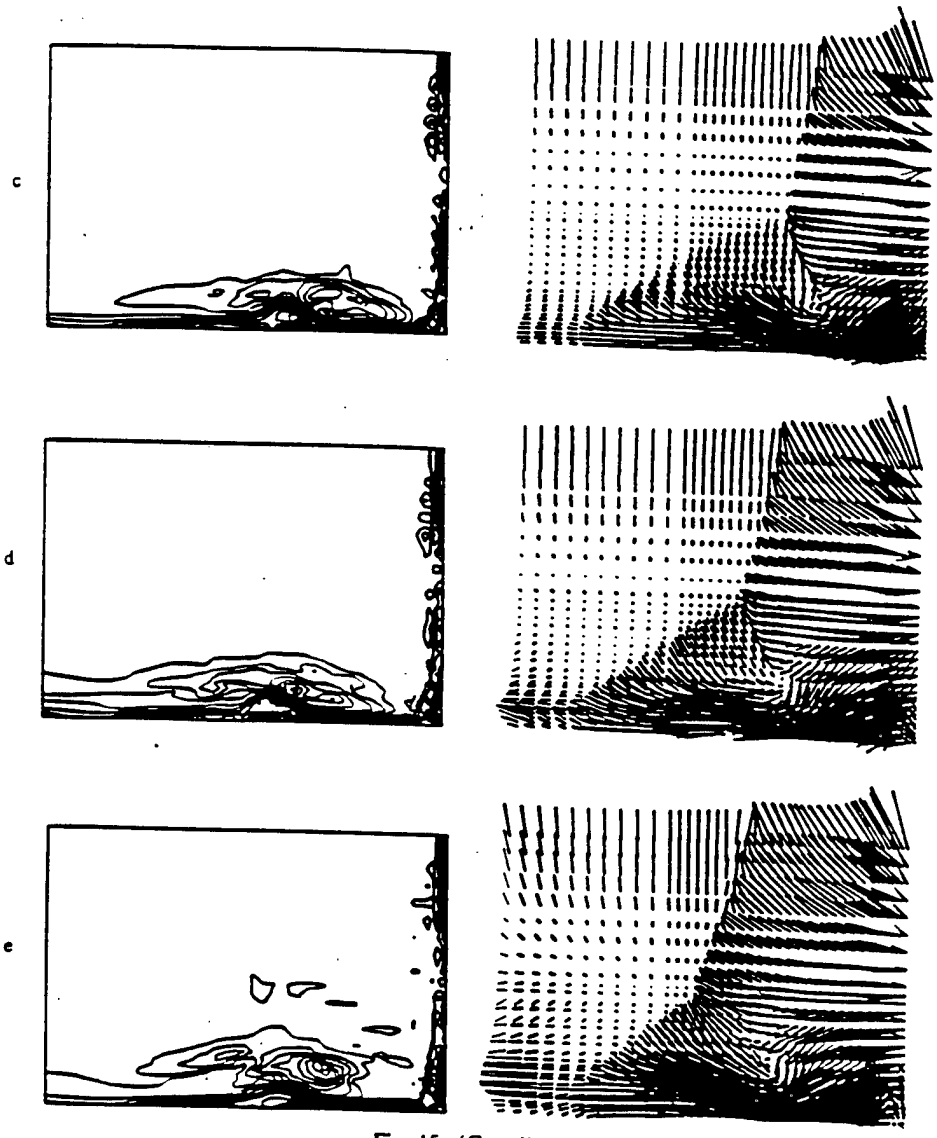

Fig. 15. (Contd)

in the $y\cos\alpha$-direction, with each plane identified as a, b, c, d. The vortex stretching occurs again toward downstream and moving upward away from the shock. The growth of vorticity is concentrated within the boundary layer close to the wall.

In Fig. 17 the spanwise horizontal plane vorticity contours are presented at various locations (a: $2\delta_0$, b: δ_0, c: $0.5\delta_0$) where δ_0 is the boundary layer thickness. It is seen that vorticity increases towards the wall with its intensity increasing toward downstream as expected.

Unsteadiness of the turbulent microscale behavior in the boundary layer as discussed in Section 4 and in [24], detailed spectral convergence behavior, and other aspects of DNS are not included in this paper, but will be reported elsewhere.

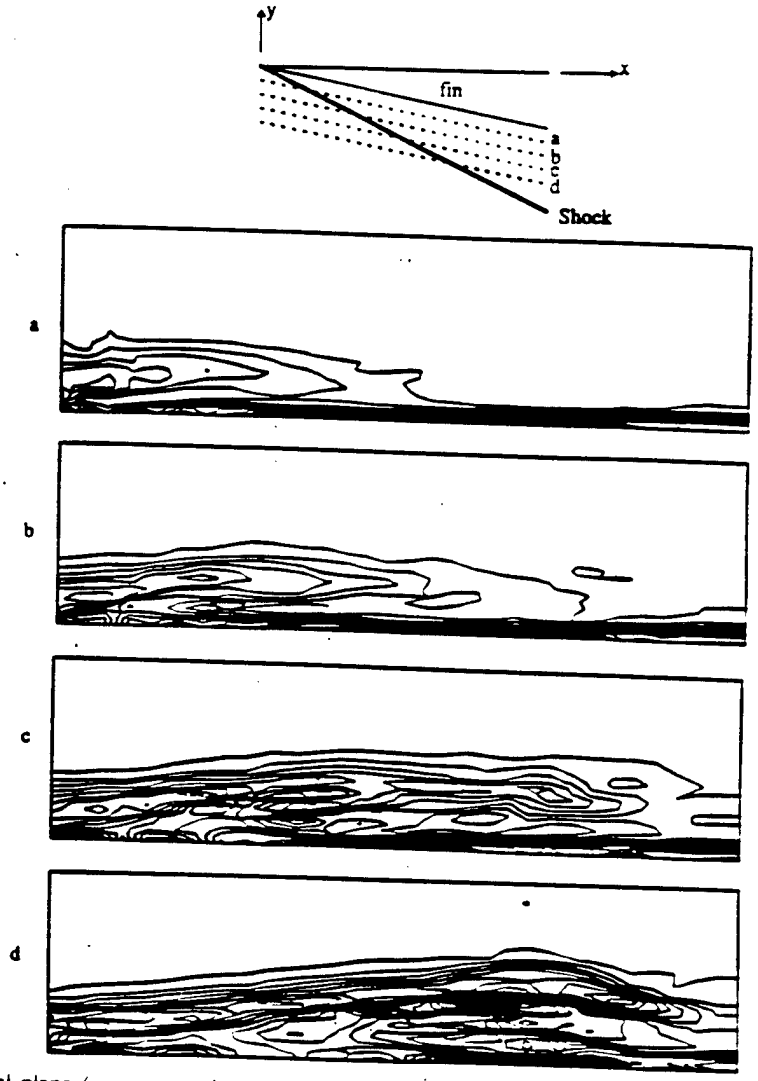

Fig. 16. Spanwise vertical plane ($x\cos\alpha - z$ plane) vorticity contours at various locations ($t = 0.3965$ ms, $0 \le z/\delta_0 \le 2.5$). The vortex stretching occurs again toward downstream and moving upward away from the shock. The growth of vorticity is concentrated within the boundary layer close to the wall.

7. Conclusions

Based on the preliminary results obtained for the direct numerical simulation using the MEI generalized Galerkin Legendre polynomial spectral element method, it appears that our original goal for the initial attempt has been successfully achieved. Elaborate data structure schemes which have been developed are the major factor for these achievements. In addition, the preliminary results for three-dimensional computations of sharp fin wave turbulent boundary layer interactions as well as the 2-D benchmark problems are satisfactory.

There are still many more tasks remaining unexplored. They include: (1) verification of 3-D fluctuations, unsteadiness, and turbulent micro-scales as related to turbulent Mach number, turbulent Prandtl number, and turbulent Reynolds number, (2) characterization of compressibility effects and relaminarization, (3) energy spectrum data versus frequency domain and complete 3-D turbulent

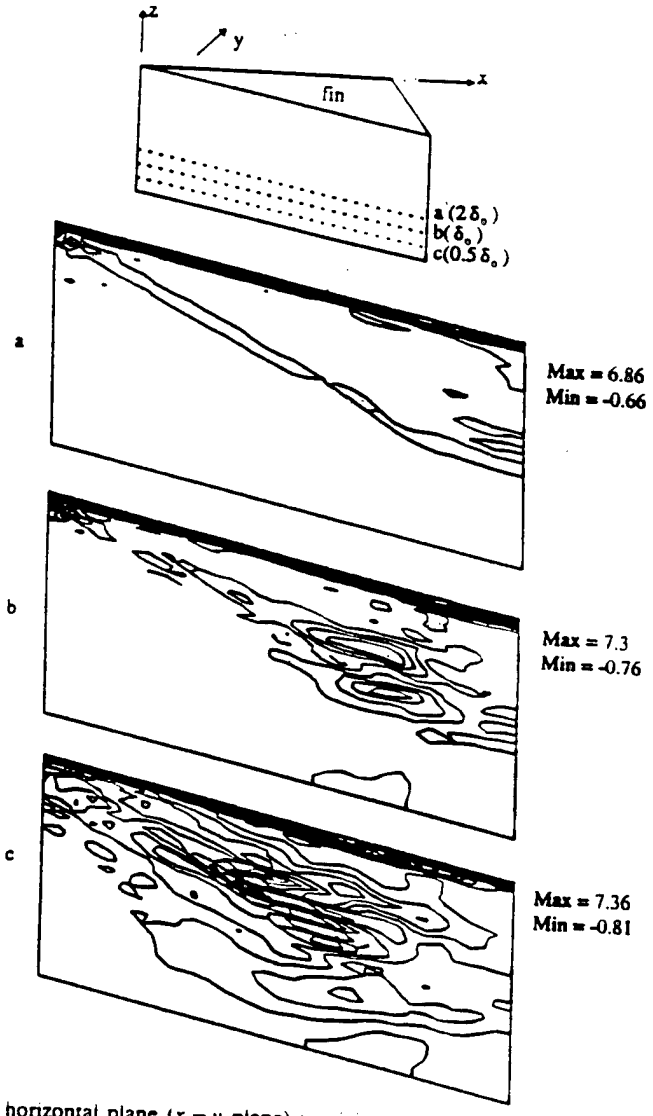

Fig. 17. Spanwise horizontal plane ($x-y$ plane) vorticity contours at various locations ($t = 0.3965$ ms).

statistics. (4) laminar-turbulence transition instability, (5) reliable optimal control of h-p interactions with Legendre polynomials, (6) temporal and spatial dependency of implicitness parameters, among others. They constitute challenging future tasks in years to come. In summary, it is concluded that the direct numerical simulation for turbulent compressible flows with the Legendre polynomial spectral element method appears to be promising.

Acknowledgment

Support of this work by AFOSR Grant F49620-93-1-0020DEF, under the direction of technical monitor Leonidas Sakell, is gratefully acknowledged.

Appendix A

A.1. Analogy between MEI-GGM and FDM-TVD

For simplicity let us write (12) in terms of one-dimensional linear functions and one-dimensional Jacobians a, b and c with all Neumann boundary terms neglected. Integrating (12) by parts we obtain

$$\frac{1}{6\Delta t}(\Delta U_{i-1}^{n+1} + 4\Delta U_i^{n+1} + \Delta U_{i-1}^{n+1}) = \frac{1}{2\Delta x}(s_1 a + s_3 b)(\Delta U_{i+1}^{n+1} - \Delta U_{i-1}^{n+1})$$
$$+ \frac{\Delta t}{2\Delta x^2}[s_2 a^2 - 2s_3 c + \Delta t\, s_2 ba + 2s_4 b(a+b)](\Delta U_{i+1}^{n+1} - 2\Delta U_i^{n+1} + \Delta U_{i-1}^{n+1})$$
$$+ \frac{1}{2\Delta x}(F_{i+1}^n - F_{i-1}^n + G_{i+1}^n - G_{i-1}^n) + \frac{\Delta t}{2\Delta x^2}(a+b)(F_{i+1}^n - 2F_i^n + F_{i-1}^n + G_{i+1}^n - 2G_i^n + G_{i-1}^n) \tag{A.1}$$

Neglecting all diffusion terms and adjusting nodal points arbitrarily, we have

$$\frac{\Delta U_i^{n+1}}{\Delta t} = \frac{s_1 a}{\Delta x}(\Delta U_i^{n+1} - \Delta U_{i-1}^{n+1}) + \frac{s_2 a^2 \Delta t}{2\Delta x^2}(\Delta U_i^{n+1} - 2\Delta U_{i-1}^{n+1} + \Delta U_{i-2}^{n+1})$$
$$+ \frac{1}{\Delta x}(F_i^n - F_{i-1}^n) + \frac{a\Delta t}{2\Delta x^2}(F_i^n - 2F_{i-1}^n + F_{i-2}^n) \tag{A.2}$$

The FDM-TVD for the 1-D Euler equation is written as

$$\frac{dU_i}{dt} = -\frac{a^-}{\Delta x}\left[(U_i - U_{i-1}) + \frac{1}{2}\Psi_{i-1/2}^+(U_i - U_{i-1}) - \frac{1}{2}\Psi_{i-3/2}^+(U_{i-1} - U_{i-2})\right]$$
$$- \frac{a^-}{\Delta x}\left[(U_{i+1} - U_i) + \frac{1}{2}\Psi_{i+1/2}^-(U_{i+1} - U_i) - \frac{1}{2}\Psi_{i+3/2}^-(U_{i+2} - U_{i-1})\right] \tag{A.3}$$

with

$$a^+ = \max(0, a) = \frac{1}{2}(a + |a|) \qquad a^- = \max(0, a) = \frac{1}{2}(a - |a|)$$

Introducing an implicitness parameter s for the time derivative on RHS of (A.3) in the form

$$U_i = U_i^n + s\,\Delta U_i^{n+1} \tag{A.4}$$

Substituting (A.4) into (A.3) and assuming that

$$a^- = 0 \qquad a^+ = a \qquad \Psi_{i-1/2}^+ = \Psi_{i-3/2}^+ = \Psi$$

we obtain

$$\frac{\Delta U_i^{n+1}}{\Delta t} = \frac{sa}{2\Delta x}(\Delta U_i^{n+1} - \Delta U_{i-1}^{n+1}) - \frac{s\Psi a\,\Delta x}{2\Delta x^2}(\Delta U_i^{n+1} - 2\Delta U_{i-1}^{n+1} + \Delta U_{i-2}^{n+1})$$
$$+ \frac{1}{\Delta x}(F_i^n - F_{i-1}^n) - \frac{\Psi\,\Delta x}{2\Delta x^2}(F_i^n - 2F_{i-1}^n + F_{i-2}^n) \tag{A.5}$$

Comparing (A.2) and (A.5) reveals that, with $s_1 = -s/2$, $s_2 = s\,\Delta x\,\Psi/(a\,\Delta t)$, and -1 for the coefficient of $(F_i^n - F_{i-1}^n)$ term, we note that the MEI-GGM formulation and FDM-TVD scheme are analogous; in fact, they are identical under the assumptions made above. The implicitness parameters s_1 and s_2 in the MEI-GGM scheme play the role of TVD limiters, Ψ. However, the implicitness parameters s_3 and s_4, beyond the concept of TVD scheme, together with s_1 and s_2, are expected to govern complex physical phenomena such as turbulent boundary layer interactions with shock waves, finite rate chemistry, widely disparate length and time scales, compressibility effects in high Mach number flows, etc. Note that most of other FDM schemes (such as McCormack or Beam–Warming schemes) arise with proper choices of implicitness parameters in (A.1).

Appendix B

B.1. Integrals of spectral element interpolation functions

$$A^{\delta}_{\alpha n}=\int_{\Omega}\Phi_{\alpha}\hat{\Phi}^{\delta}_{n}\,d\Omega \qquad A^{\eta}_{\alpha np}=\int_{\Omega}\Phi_{\alpha}\hat{\Phi}^{\eta}_{np}\,d\Omega \qquad A_{\alpha npq}=\int_{\Omega}\Phi_{\alpha}\hat{\Phi}_{npq}\,d\Omega \qquad A^{\gamma}_{m\beta}=\int_{\Omega}\hat{\Phi}^{\gamma}_{m}\Phi_{\beta}\,d\Omega$$

$$A^{\gamma\delta}_{mn}=\int_{\Omega}\hat{\Phi}^{\gamma}_{m}\hat{\Phi}^{\delta}_{n}\,d\Omega \qquad A^{\gamma\eta}_{mnp}=\int_{\Omega}\hat{\Phi}^{\gamma}_{m}\hat{\Phi}^{\eta}_{np}\,d\Omega \qquad A^{\gamma}_{mnpq}=\int_{\Omega}\hat{\Phi}^{\gamma}_{m}\hat{\Phi}_{npq}\,d\Omega \qquad A^{\xi}_{mk\beta}=\int_{\Omega}\hat{\Phi}^{\xi}_{mk}\Phi_{\beta}\,d\Omega$$

$$A^{\xi\delta}_{mkn}=\int_{\Omega}\hat{\Phi}^{\xi}_{mk}\hat{\Phi}^{\delta}_{n}\,d\Omega \qquad A^{\xi\eta}_{mknp}=\int_{\Omega}\hat{\Phi}^{\xi}_{mk}\hat{\Phi}^{\eta}_{np}\,d\Omega \qquad A^{\xi}_{mknpq}=\int_{\Omega}\hat{\Phi}^{\xi}_{mk}\hat{\Phi}_{npq}\,d\Omega \qquad A_{mku\beta}=\int_{\Omega}\hat{\Phi}_{mku}\Phi_{\beta}\,d\Omega$$

$$A^{\delta}_{mkun}=\int_{\Omega}\hat{\Phi}_{mku}\hat{\Phi}^{\delta}_{n}\,d\Omega \qquad A^{\eta}_{mkunp}=\int_{\Omega}\hat{\Phi}_{mku}\hat{\Phi}^{\eta}_{np}\,d\Omega \qquad A_{mkunpq}=\int_{\Omega}\hat{\Phi}_{mku}\hat{\Phi}_{npq}\,d\Omega$$

$$B^{\delta}_{\alpha nrs}=\int_{\Omega}\left\{-\Delta t[(s_1a_{irs}+s_3b_{irs})\Phi_{\alpha,i}\hat{\Phi}^{\delta}_{n}+s_3c_{ijrs}\Phi_{\alpha,i}\hat{\Phi}_{n,j}]+\frac{\Delta t^2}{2}(s_2d_{ijrs}+s_4e_{ijrs})\Phi_{\alpha,i}\hat{\Phi}^{\delta}_{n,j}\right\}d\Omega$$

with

$$d_{ijrs}=a_{ir}a_{js}+b_{ir}a_{js} \qquad e_{ijrs}=a_{ir}b_{js}-b_{ir}b_{js}$$

$$B^{\eta}_{\alpha npsr}=\int_{\Omega}\left\{-\Delta t[(s_1a_{irs}+s_3b_{irs})\Phi_{\alpha,i}\hat{\Phi}^{\eta}_{np}+s_3c_{ijrs}\Phi_{\alpha,i}\hat{\Phi}^{\eta}_{np,j}]-\frac{\Delta t^2}{2}(s_2d_{ijrs}+s_4e_{ijrs})\Phi_{\alpha,i}\hat{\Phi}^{\eta}_{np,j}\right\}d\Omega$$

$$B_{\alpha npqrs}=\int_{\Omega}\left\{-\Delta t[(s_1a_{irs}+s_3b_{irs})\Phi_{\alpha,i}\hat{\Phi}_{npq}+s_3c_{ijrs}\Phi_{\alpha,i}\hat{\Phi}_{npq,j}]+\frac{\Delta t^2}{2}(s_2d_{ijrs}+s_4e_{ijrs})\Phi_{\alpha,i}\hat{\Phi}_{npq,j}\right\}d\Omega$$

$$B^{\gamma}_{m\beta rs}=\int_{\Omega}\left\{-\Delta t[(s_1a_{irs}+s_3b_{irs})\hat{\Phi}^{\gamma}_{m,i}\Phi_{\beta}+s_3c_{ijrs}\hat{\Phi}^{\gamma}_{m,i}\Phi_{\beta,j}]+\frac{\Delta t^2}{2}(s_2d_{ijrs}+s_4e_{ijrs})\hat{\Phi}^{\gamma}_{m,i}\Phi_{\beta,j}\right\}d\Omega$$

$$C^{\gamma\delta}_{mnrs}=\int_{\Omega}\left\{-\Delta t[(s_1a_{irs}+s_3b_{irs})\hat{\Phi}^{\gamma}_{m,i}\hat{\Phi}^{\delta}_{n}+s_3c_{ijrs}\hat{\Phi}^{\gamma}_{m,i}\hat{\Phi}^{\delta}_{n,j}]+\frac{\Delta t^2}{2}(s_2d_{ijrs}+s_4e_{ijrs})\hat{\Phi}^{\gamma}_{m,i}\hat{\Phi}^{\delta}_{n,j}\right\}d\Omega$$

$$C^{\gamma\eta}_{mnprs}=\int_{\Omega}\left\{-\Delta t[(s_1a_{irs}+s_3b_{irs})\hat{\Phi}^{\gamma}_{m,i}\hat{\Phi}^{\eta}_{np}+s_3c_{ijrs}\hat{\Phi}^{\gamma}_{m,i}\hat{\Phi}^{\eta}_{np,j}]+\frac{\Delta t^2}{2}(s_2d_{ijrs}+s_4e_{ijrs})\hat{\Phi}^{\gamma}_{m,i}\hat{\Phi}^{\eta}_{np,j}\right\}d\Omega$$

$$C^{\gamma}_{mnpqrs}=\int_{\Omega}\left\{-\Delta t[(s_1a_{irs}+s_3b_{irs})\hat{\Phi}^{\gamma}_{m,i}\hat{\Phi}_{npq}+s_3c_{ijrs}\hat{\Phi}^{\gamma}_{m,i}\hat{\Phi}_{npq,j}]+\frac{\Delta t^2}{2}(s_2d_{ijrs}+s_4e_{ijrs})\hat{\Phi}^{\gamma}_{m,i}\hat{\Phi}_{npq,j}\right\}d\Omega$$

$$B^{\xi}_{mk\beta rs}=\int_{\Omega}\left\{-\Delta t[(s_1a_{irs}+s_3b_{irs})\hat{\Phi}^{\xi}_{mk,i}\Phi_{\beta}+s_3c_{ijrs}\hat{\Phi}^{\xi}_{mk,i}\Phi_{\beta,j}]+\frac{\Delta t^2}{2}(s_2d_{ijrs}+s_4e_{ijrs})\hat{\Phi}^{\xi}_{mk,i}\Phi_{\beta,j}\right\}d\Omega$$

$$C^{\xi\delta}_{mknrs}=\int_{\Omega}\left\{-\Delta t[(s_1a_{irs}+s_3b_{irs})\hat{\Phi}^{\xi}_{mk,i}\hat{\Phi}^{\delta}_{n}+s_3c_{ijrs}\hat{\Phi}^{\xi}_{mk,i}\hat{\Phi}^{\delta}_{n,j}]+\frac{\Delta t^2}{2}(s_2d_{ijrs}+s_4e_{ijrs})\hat{\Phi}^{\xi}_{mk,i}\hat{\Phi}^{\delta}_{n,j}\right\}d\Omega$$

$$D^{\xi\eta}_{mknprs}=\int_{\Omega}\left\{-\Delta t[(s_1a_{irs}+s_3b_{irs})\hat{\Phi}^{\xi}_{mk,i}\hat{\Phi}^{\eta}_{np}+s_3c_{ijrs}\hat{\Phi}^{\xi}_{mk,i}\hat{\Phi}^{\eta}_{np,j}]+\frac{\Delta t^2}{2}(s_2d_{ijrs}+s_4e_{ijrs})\hat{\Phi}^{\xi}_{mk,i}\hat{\Phi}^{\eta}_{np,j}\right\}d\Omega$$

$$D^{\xi}_{mknpqrs}=\int_{\Omega}\left\{-\Delta t[(s_1a_{irs}+s_3b_{irs})\hat{\Phi}^{\xi}_{mk,i}\hat{\Phi}_{npq}+s_3c_{ijrs}\hat{\Phi}^{\xi}_{mk,i}\hat{\Phi}_{npq,j}]+\frac{\Delta t^2}{2}(s_2d_{ijrs}+s_4e_{ijrs})\hat{\Phi}^{\xi}_{mk,i}\hat{\Phi}_{npq,j}\right\}d\Omega$$

$$B_{mku\beta rs}=\int_{\Omega}\left\{-\Delta t[(s_1a_{irs}+s_3b_{irs})\hat{\Phi}_{mku,i}\Phi_{\beta}+s_3c_{ijrs}\hat{\Phi}_{mku,i}\Phi_{\beta,j}]+\frac{\Delta t^2}{2}(s_2d_{ijrs}+s_4e_{ijrs})\hat{\Phi}_{mku,i}\Phi_{\beta,j}\right\}d\Omega$$

$$C^{\delta}_{mkunrs}=\int_{\Omega}\left\{-\Delta t[(s_1a_{irs}+s_3b_{irs})\hat{\Phi}_{mku,i}\hat{\Phi}^{\delta}_{n}+s_3c_{ijrs}\hat{\Phi}_{mku,i}\hat{\Phi}^{\delta}_{n,j}]+\frac{\Delta t^2}{2}(s_2d_{ijrs}+s_4e_{ijrs})\hat{\Phi}_{mku,i}\hat{\Phi}^{\delta}_{n,j}\right\}d\Omega$$

$$D^{\eta}_{mkunprs}=\int_{\Omega}\left\{-\Delta t[(s_1a_{irs}+s_3b_{irs})\hat{\Phi}_{mku,i}\hat{\Phi}^{\eta}_{np}+s_3c_{ijrs}\hat{\Phi}_{mku,i}\hat{\Phi}^{\eta}_{np,j}]+\frac{\Delta t^2}{2}(s_2d_{ijrs}+s_4e_{ijrs})\hat{\Phi}_{mku,i}\hat{\Phi}^{\eta}_{np,j}\right\}d\Omega$$

$$E_{mkunpqrs}=\int_{\Omega}\left\{-\Delta t[(s_1a_{irs}+s_3b_{irs})\hat{\Phi}_{mku,i}\hat{\Phi}_{npq}+s_3c_{ijrs}\hat{\Phi}_{mku,i}\hat{\Phi}_{npq,j}]+\frac{\Delta t^2}{2}(s_2d_{ijrs}+s_4e_{ijrs})\hat{\Phi}_{mku,i}\hat{\Phi}_{npq,j}\right\}d\Omega$$

$$\hat{W}^{\gamma}_{mr}=\int_{\Omega}\left\{\Delta t\,\hat{\Phi}^{\gamma}_{m,i}\Phi_{\beta}(F^{n}_{\beta ir}+G^{n}_{\beta ir})-\frac{\Delta t^2}{2}(a_{irs}+b_{irs})\hat{\Phi}^{\gamma}_{m,i}\Phi_{\beta,j}(F^{n}_{\beta js}+G^{n}_{\beta js})\right\}d\Omega$$

$$+\int_\Gamma \left\{ \Delta t\, \overset{*}{\hat{\Phi}}{}^{\gamma}_{m}[-s_1 a_{irs}\,\Delta U^{n+1}_{s} - s_3(b_{irs}\,\Delta U^{n+1}_{s} - c_{ijrs}\,\Delta U^{n+1}_{s,j})] + \frac{\Delta t^2}{2}\,\overset{*}{\hat{\Phi}}{}^{\gamma}_{m}[s_2(a_{irq}a_{jqs} + b_{irq}a_{jqs}) \right.$$

$$\left. + s_4(a_{irq}b_{jqs} + b_{irq}b_{jqs})]\,\Delta U^{n+1}_{s,j} \right\} n_i\,\mathrm{d}\Gamma - \int_\Gamma \overset{*}{\hat{\Phi}}{}^{\gamma}_{m}\left[\Delta t(F^n_{ir} + G^n_{ir}) - \frac{\Delta t^2}{2}(a_{irs} + b_{irs})(F^n_{js,j} - G^n_{js,j})\right] n_i\,\mathrm{d}\Gamma$$

$$\hat{W}^{\epsilon}_{mkr} = \int_\Omega \left\{ \Delta t\,\hat{\Phi}^{\epsilon}_{mk,i}\Phi_\beta(F^n_{\beta ir} + G^n_{\beta ir}) - \frac{\Delta t^2}{2}(a_{irs} + b_{irs})\hat{\Phi}^{\epsilon}_{mk,i}\Phi_{\beta,j}(F^n_{\beta js} - G^n_{\beta js}) \right\} \mathrm{d}\Omega$$

$$+\int_\Gamma \left\{ \Delta t\, \overset{*}{\hat{\Phi}}{}^{\epsilon}_{mk}[-s_1 a_{irs}\,\Delta U^{n+1}_{s} - s_3(b_{irs}\,\Delta U^{n+1}_{s} + c_{ijrs}\,\Delta U^{n+1}_{s,j})] + \frac{\Delta t^2}{2}\,\overset{*}{\hat{\Phi}}{}^{\epsilon}_{mk}[s_2(a_{irq}a_{jqs} + b_{irq}a_{jqs}) \right.$$

$$\left. + s_4(a_{irq}b_{jqs} + b_{irq}b_{jqs})]\,\Delta U^{n+1}_{s,j} \right\} n_i\,\mathrm{d}\Gamma - \int_\Gamma \overset{*}{\hat{\Phi}}{}^{\epsilon}_{mk}\left[\Delta t(F^n_{ir} + G^n_{ir}) - \frac{\Delta t^2}{2}(a_{irs} + b_{irs})(F^n_{js,j} + G^n_{js,j})\right] n_i\,\mathrm{d}\Gamma$$

$$\hat{W}_{mkur} = \int_\Omega \left\{ \Delta t\,\hat{\Phi}_{mku,i}\Phi_\beta(F^n_{\beta ir} + G^n_{\beta ir}) - \frac{\Delta t^2}{2}(a_{irs} + b_{irs})\hat{\Phi}_{mku,i}\Phi_{\beta,j}(F^n_{\beta js} + G^n_{\beta js}) \right\} \mathrm{d}\Omega$$

References

[1] J.E. Green, Interaction between shock waves and boundary layers, Prog. Aerospace Sci. 11 (1970) 235–340.

[2] R.H. Korkegi, Survey of viscous interactions associated with high Mach number flight, AIAA J. 9 (1971) 771–784.

[3] D.J. Peake and M. Tobak, Three-dimensional interactions and vortical flows with emphasis on high speeds, NASA TM 81169, March, 1980.

[4] T.C. Adamson and A.F. Messiter, Analysis of two-dimensional interactions between shock waves and boundary layers, Annu. Rev. Fluid Mech. 12 (1980) 103–138.

[5] G.S. Settle and D.S. Dolling, Swept shock wave boundary layer interactions, tactical missile aerodynamics, in: M.J. Hemsch and J.N. Nielsen, eds., Progress in Astronautics and Aeronautics, Vol. 104 (AIAA, New York, 1986) 297–379.

[6] S. Lee, S.K. Lele and P. Moin, Direct numerical simulation and analysis of shock turbulence interaction, AIAA Paper 91-0523, 1991.

[7] D.D. Knight, T.J. Garrison, G.S. Settles, A.A. Sheltovodov, A.I. Maksimov, A.M. Shevchenko and S.S. Vorontsov, Asymmetric crossing-shock wave/turbulent boundary layer interaction, AIAA J. 33(12) (1995) 2241–2249.

[8] Y.M. Kim and T.J. Chung, Finite element analysis of turbulent diffusion flames, AIAA J. 27(3) (1989) 330–339.

[9] T.J. Chung and W.S. Yoon, Effects of reacting flows with turbulence and shock waves on efficiency of scramjet combustors, 28th JANNAF Combustion Meeting, Oct. 18–Nov. 1, 1991.

[10] B. Guo and I. Babuska, The *h-p* version of the finite element method, Parts 1 and 2, Comput. Mech. 1 (1986) 21–41 and 203–220.

[11] I. Babuska and M. Suri, The *h-p* version of the finite element method with quasi-uniform meshes, RAIRO Math Mod. Numer. Anal. 21(2) (1987) 199–238.

[12] W. Gui and I. Babuska, The *h*, *p*, and *h-p* versions of the finite element method in one dimension, Parts 1, 2, 3, Numer. Math. 49 (1986) 577–683.

[13] B. Szabó and I. Babuska, Finite Element Analysis (John Wiley & Sons, 1991) 96–99.

[14] L. Demkowicz, J.T. Oden, W. Rachowicz and O. Hardy, Toward a universal *h-p* adaptive finite element strategy, Part 1, Constrained approximation and data structure, Comput. Methods Appl. Mech. Engrg. 77 (1989) 79–112.

[15] J.T. Oden, L. Demkowicz, W. Rachowicz and T.A. Westermann, Toward a universal *h-p* adaptive finite element strategy, Part 2, A posteriori error estimation, Comput. Methods Appl. Mech. Engrg. 77 (1989) 113–180.

[16] W. Rachowicz, J.T. Oden and L. Demkowicz, Toward a universal *h-p* adaptive finite element strategy, Part 3, Design of *h-p* meshes, Comput. Methods Appl. Mech. Engrg. 77 (1989) 181–212.

[17] J.T. Oden, Theory and implementation of high-order adaptive *hp*-methods for the analysis of incompressible viscous flows, Comput. Nonlinear Mech. Aerospace Engrg., a volume in the AIAA Prog. in Aeronautics and Astronautics, Series, S.N. Atluri, ed. (1993).

[18] T.J. Chung and W.S. Yoon, Hypersonic combustion with shock waves in turbulent reacting flows, AIAA Paper 92-3426, 1992.

[19] T.J. Chung and W.S. Yoon, Numerical simulations of airbreathing combustion at all speed regimes, AIAA Paper 93-1972, 1993.

[20] T.J. Chung and W.S. Yoon, Finite rate chemical reactions in subsonic, supersonic, and hypersonic turbulent flows, AIAA Paper 93-2993, 1993.

[21] T.J. Chung, Finite Element Analysis in Fluid Dynamics (McGraw-Hill, 1978).

[22] T.J. Chung and W.S. Yoon, Wave instability in combustion, Comput. Methods Appl. Mech. Engrg. 90 (1991) 583–608.

[23] W.S. Yoon and T.J. Chung, Nonlinearly unstable waves dominated by entropy mode, J. Acoust. Soc. Am. 96(2) Pt. 1 (August 1994).
[24] K.T. Yoon and T.J. Chung, Unsteady turbulent boundary layer interactions in high speed flows, AIAA Paper 95-2223, 1995.
[25] A.T. Patera, A spectral element method for fluid dynamics: Laminar flow in a channel expansion, J. Comput. Phys. 54 (1984) 468–488.
[26] K.Z. Korczak and A.T. Petera, An isoparametric spectral element method for solution of the Navier–Stokes equations in complex geometry, J. Comput. Phys. 62 (1986) 361–382.
[27] T.A. Zang, M.Y. Hussaini and D.M. Bushnell, Numerical computations of turbulence amplification in shock wave interactions, AIAA J. 22(1) (1984) 13–21.
[28] N.N. Mansour, J. Kim and P. Moin, Reynolds-stress and dissipation-rate budgets in a turbulent channel flow, J. Fluid Mech. 194 (1988) 15–44.
[29] S.K. Lele, Direct numerical simulation of compressible free shear flows, AIAA Paper 89-0374, 1989.
[30] W.W. Tworzydlo, J.T. Oden and E.A. Thomton, Adaptive implicit/explicit finite element method for compressible viscous flows, Comput. Methods Appl. Mech. Engrg. 95 (1992) 397–440.
[31] T.J. Chung and K.T. Yoon, Direct numerical simulation of compressible turbulent flows using adaptive spectral elements, Final Report, AFOSR, F49620-93-1-0020, December, 1994.
[32] P. Ardonceua, D.H. Lee, T. Alziary de Roquefort and R. Goethals, Turbulence behavior in a shockwave boundary layer interactions, AGARD CP-271, Paper no. 8, 1980.
[33] J.E. Carter, Numerical solutions of the Navier–Stokes equations for the supersonic laminar flow over a two-dimensional compression corner, NASA TR R-385 (1972) 21–29.
[34] G.S. Settles and D.S. Dolling, Swept shock/boundary interactions—tutorial and update, AIAA Paper 90-0375, 1990.
[35] D. Knight, C. Horstman and B. Shapey, The flowfield structure of the 3-D shock wave-boundary layer interaction generated by a 20 degree sharp fin at Mach 3, AIAA Paper 86-0343, 1986.
[36] N. Narayanswami, C.C. Horstman and D.D. Knight, Computation of crossing shock/turbulence layer interaction at Mach 8.3, AIAA J. 31(8) (1993) 1369–1376.

ББК 24.54
Г 68
УДК 544

Advanced Computation and Analysis of Combustion / [Edited by G. D. Roy, S. M. Frolov, P. Givi]. — Moscow: ENAS Publishers, 1997. — 592 p. Tabl. 27, il. 273.

ISBN 5-89055-006-3

Selected papers presented at the International Colloquium on Advanced Computation and Analysis of Combustion held in Moscow. May 12–15, 1997, are assembled together in this volume. The papers present the strategies of systematic reduction of detailed reaction mechanisms, new numerical approaches for studies of multiphase reacting flows, advanced methods addressing mixing and combustion phenomena in high-speed flows, new modeling approaches to turbulent combustion, and a whole spectrum of advanced numerical methods relevant to turbulent combustion. The volume is intended to be a tool to explore the present state of the art, and an avenue for further follow-up for the researcher as well as practicing engineer.

В $\frac{03}{41C(03)-95}$ Без объявл.

ББК 24.54

ISBN 5-89055-006-3

Advanced Computation & Analysis of Combustion: 466–489

A NEW COMPUTATIONAL APPROACH WITH FLOWFIELD-DEPENDENT IMPLICITNESS ALGORITHM FOR APPLICATIONS TO SUPERSONIC COMBUSTION

T.J. Chung

Department of Mechanical and Aerospace Engineering, The University of Alabama in Huntsville, Huntsville, AL 35899, USA

Computations in reacting flows particularly for supersonic combustion are considerably more complicated than in nonreacting flows or low-speed combustion. This is due to widely disparate reaction rates for different species associated with finite rate chemistry and shock wave turbulent boundary layer interactions. Changes of nondimensional flow variables such as Mach, Reynolds, Peclet, and Damköhler numbers between adjacent nodal points and between time steps can be important factors in selecting suitable computational schemes as they are indicative of physics of the flow. It is toward this idea that the proposed approach called "Flowfield-Dependent Mixed Explicit–Implicit (FDMEI) Method" is developed in this paper. Here, every nodal point or element is provided with a unique numerical scheme according to their current flowfield situations, as characterized by a total of six implicitness parameters which are calculated from the changes of Mach, Reynolds, Peclet, and Damköhler numbers between adjacent nodal points and between time steps. These flowfield-dependent implicitness parameters represent whether or not the flowfield is compressible, incompressible, viscous, inviscid, laminar, turbulent, as well as the status of chemical reactions. In this procedure, discontinuities or fluctuations of all variables between adjacent nodal points and between time steps are reflected in the solution of the Navier–Stokes system of equations so that the fluctuation components can be obtained as the difference between the Navier–Stokes solutions and the mean flow components calculated from the standard time averages or the fast Fourier transform of the Navier–Stokes solutions. If all implicitness parameters are fixed to certain numbers instead of being calculated from the flowfield information, then practically all currently available numerical schemes arise as special cases. The proposed approach is believed to be most applicable to direct numerical simulation of the supersonic combustion where temperature gradients are extremely high and where shock wave turbulent boundary layer interactions are significant. Due to computer limitations, however, numerical examples in this paper are only for coarse mesh and simple cases without resolving turbulent microscales. Further studies on the proposed FDMEI method in applications to supersonic combustion are very much in need.

1 INTRODUCTION

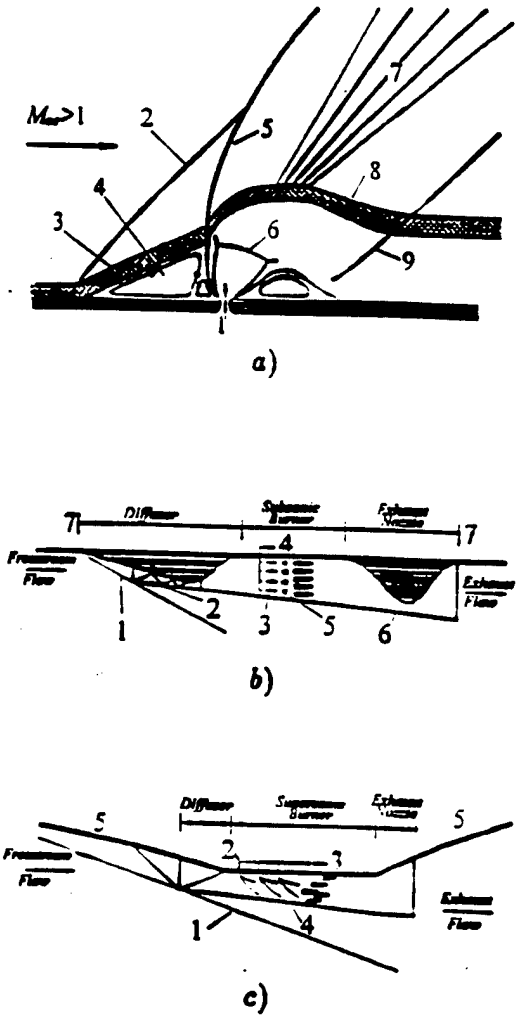

Figure 1. Supersonic combustion geometries. (*a*) Reacting flow (airbreathing combustion). *1* — injector; *2* — separation shock; *3* — boundary layer; *4* — upstream recirculation; *5* — bow shock; *6* — Mach disk; *7* — expansion waves; *8* — mixing layer; *9* — reattachment shock.) (*b*) Ramjet combustion. *1* — diffuser oblique shock wave; *2* — normal shock system; *3* — fuel injectors; *4* — fuel; *5* — flame holders; *6* — engine cowl; *7* — vehicle boundary. (*c*) Scramjet combustion. *1* — forebody oblique shock wave; *2* — fuel injectors; *3* — fuel; *4* — engine cowl; *5* — vehicle boundary

Nearly half a century has elapsed since the digital computer revolutionized computational techniques in engineering and mathematical physics. During this time finite difference methods (FDM) have dominated the field of computational fluid dynamics (CFD) [1–4], whereas the opposite is true for finite element methods (FEM) in solid mechanics. In recent years, however, the trend toward finite element methods in CFD appears to be increasingly favorable [5–9]. Numerical methods for supersonic combustion mainly with FDM have been actively pursued since the late 1980's [10–13].

One of the most important questions in CFD is how to deal with large gradients of the variable (density, velocity, pressure, temperature, and source terms). Rapid changes of Mach numbers, Reynolds numbers, Peclet numbers, and Damköhler numbers (if reacting) between adjacent nodal points or elements can be a crucial factor in determining whether the chosen computational scheme will succeed or fail. Furthermore, proper treatments for incompressibility and compressibility, viscous and inviscid flows, subsonic and supersonic flows, laminar and turbulent flows, nonreacting and reacting flows are extremely important. These various flow properties may be depicted in typical reacting flow problems for ramjet and scramjet combustion as shown in Figs. 1*a,b,c*.

Can there be a general approach to satisfy all the requirements mentioned above? Can a single mathematical for-

mulation lead to most of the currently available computational schemes both in FDM and FEM as special cases? Most importantly, will such an approach guarantee accuracy and efficiency? In this paper, our goal is to respond to these questions positively. To this end, our approach, known as the Flowfield-Dependent Mixed Explicit–Implicit (FDMEI) method, is based on the following procedure [7–9]:

(a) Write the Navier–Stokes system of equations in a conservation form.

(b) Expand the conservation variable U^{n+1} in Taylor series up to and including the second-order time derivatives of the conservation variables.

(c) Introduce in step (b) six different flowfield-dependent implicitness parameters which are calculated from the changes in Mach, Reynolds, Peclet, and Damköhler numbers (if reacting) between nodal points or local elements.

(d) Substitute step (a) and (c) into step (b) to obtain the increments of the conservation variables ΔU^{n+1}. As a result, the final form resembles the implicit factored scheme of Beam and Warming [1], but much more rigorous.

(e) Step (d) may be used either in FDM or FEM.

The computational procedure as described above is capable of resolving complex properties of fluid flows in general with shock waves, turbulence, and reacting flows in particular:

(1) **Shock waves in compressible flows** are dependent on changes in Mach number between nodal points in FDM and within local elements in FEM. Shock wave discontinuities are characterized by these changes in Mach number.

(2) **Incompressible turbulent flows** are dependent on changes in Reynolds number between nodal points in FDM and within local elements in FEM. Incompressibility conditions are characterized by these changes in Reynolds number.

(3) **Compressible turbulent flows** are dependent on changes in both Mach number and Reynolds number between nodal points in FDM and within local elements in FEM. Dilatational dissipation is characterized by these changes in Mach number and Reynolds number.

(4) **High temperature gradient flows** are dependent on changes in Peclet number between nodal points in FDM and within local elements in FEM. The convection vs diffusion in heat transfer is characterized by these changes in Peclet number.

(5) **Reacting flows** are dependent on changes in Damköhler number between nodal points in FDM and within local elements in FEM. The mass source vs convective transfer, mass source vs diffusive transfer, heat source vs convective

heat transfer, heat source vs conductive heat transfer, and heat source vs diffusive heat transfer are characterized by these changes in Damköhler number.

(6) Direct numerical simulation (DNS) in which mesh refinements are carried out until turbulence length microscales are resolved without turbulence models can not be reliable particularly for high speed compressible turbulent flows unless the computational scheme is capable of treating high gradients of variables as described in (3) above. To improve turbulence calculations, Legendre polynomial spectral modes may be added as shown in [7]. Whether or not the spectral mode approach is advantageous for an overall computational efficiency remains to be seen. Due to the limitation of computer time, the example problems in this paper are not intended for DNS microscale resolutions.

Details of the mathematical formulations are presented in Section 2, followed by implementation and computational procedures in Section 3, some example problems in Section 4, and concluding remarks in Section 5.

2 MATHEMATICAL FORMULATIONS

For the general purpose program considering the compressible viscous reacting flows, we write the conservation form of the Navier–Stokes system of equations as

$$\frac{\partial \mathbf{U}}{\partial t} + \frac{\partial \mathbf{F}_i}{\partial x_i} + \frac{\partial \mathbf{G}_i}{\partial x_i} = \mathbf{B}\,, \tag{1}$$

where U, $\mathbf{F}_i$, $\mathbf{G}_i$, and B denote the conservation flow variables, convection flux variables, diffusion flux variables, and source terms, respectively,

$$\mathbf{U} = \begin{bmatrix} \rho \\ \rho v_j \\ \rho E \\ \rho Y_k \end{bmatrix}, \quad \mathbf{F}_i = \begin{bmatrix} \rho v_i \\ \rho v_i v_j + p\delta_{ij} \\ \rho E v_i + p v_i \\ \rho Y_k v_i \end{bmatrix},$$

$$\mathbf{G}_i = \begin{bmatrix} 0 \\ -\tau_{ij} \\ -\tau_{ij} v_j - kT_{,i} - \sum \rho c_{pk} T D_{km} Y_{k,i} \\ -\rho D_{km} Y_{k,i} \end{bmatrix}, \quad \mathbf{B} = \begin{bmatrix} 0 \\ \rho f_i \\ -H_k^o w_k + \rho f_j v_j \\ w_k \end{bmatrix} \tag{2}$$

where $f_j = \sum_{k=1}^{N} Y_k f_{kj}$ is the body force, Y_k is the chemical species, H_k^o is the zero-point enthalpy, w_k is the reaction rate, and D_{km} is the binary diffusivity. Additional equations for vibrational and electronic energies may be included in Eq. (1) for hypersonics.

Expanding the conservation variables U in Taylor series including the first and second derivatives, we have

$$\mathbf{U}^{n+1} = \mathbf{U}^n + \Delta t \frac{\partial \mathbf{U}^{n+s_1}}{\partial t} + \frac{\Delta t^2}{2} \frac{\partial^2 \mathbf{U}^{n+s_2}}{\partial t^2} + O(\Delta t^3), \tag{3}$$

where s_1 and s_2 are the implicitness parameters defined such that

$$\frac{\partial \mathbf{U}^{n+s_1}}{\partial t} = \frac{\partial \mathbf{U}^n}{\partial t} + s_1 \frac{\partial \Delta \mathbf{U}^{n+1}}{\partial t}, \qquad 0 \le s_1 \le 1, \tag{4}$$

$$\frac{\partial^2 \mathbf{U}^{n+s_2}}{\partial t^2} = \frac{\partial^2 \mathbf{U}^n}{\partial t^2} + s_2 \frac{\partial^2 \Delta \mathbf{U}^{n+1}}{\partial t^2}, \qquad 0 \le s_2 \le 1, \tag{5}$$

with $\Delta \mathbf{U}^{n+1} = \mathbf{U}^{n+1} - \mathbf{U}^n$. It is assumed that the convection flux $\mathbf{F}_i$ is a function of U and the diffusion flux $\mathbf{G}_i$ is a function of both U and its gradient $\mathbf{U}_{,i}$. Thus, we have:

$$\frac{\partial \mathbf{U}}{\partial t} = -\frac{\partial \mathbf{F}_i}{\partial x_i} - \frac{\partial \mathbf{G}_i}{\partial x_i} + \mathbf{B}, \tag{6}$$

$$\frac{\partial^2 \mathbf{U}}{\partial t^2} = -\frac{\partial}{\partial x_i}\left(\mathbf{a}_i \frac{\partial \mathbf{U}}{\partial t}\right) - \frac{\partial}{\partial x_i}\left(\mathbf{b}_i \frac{\partial \mathbf{U}}{\partial t}\right) - \frac{\partial^2}{\partial x_i \partial x_j}\left(\mathbf{c}_{ij} \frac{\partial \mathbf{U}}{\partial t}\right) + \mathbf{d}\left(\frac{\partial \mathbf{U}}{\partial t}\right), \tag{7}$$

where the convection Jacobian $\mathbf{a}_i$, the diffusion Jacobian $\mathbf{b}_i$, the diffusion gradient Jacobian $\mathbf{c}_{ij}$, and the source Jacobian d are defined as

$$\mathbf{a}_i = \frac{\partial \mathbf{F}_i}{\partial \mathbf{U}}, \quad \mathbf{b}_i = \frac{\partial \mathbf{G}_i}{\partial \mathbf{U}}, \quad \mathbf{c}_{ij} = \frac{\partial \mathbf{G}_i}{\partial \mathbf{U}_j}, \quad \mathbf{d} = \frac{\partial \mathbf{B}}{\partial \mathbf{U}} \tag{8}$$

Assuming the product of the diffusion gradient Jacobian with third order spatial derivatives to be negligible, it follows from Eqs. (1) through (7) that

$$\begin{aligned}
\Delta \mathbf{U}^{n+1} = \Delta t \Bigg[& -\frac{\partial \mathbf{F}_i^n}{\partial x_i} - \frac{\partial \mathbf{G}_i^n}{\partial x_i} + \mathbf{B}^n + s_1 \left(-\frac{\partial \Delta \mathbf{F}_i^{n+1}}{\partial x_i} - \frac{\partial \Delta \mathbf{G}_i^{n+1}}{\partial x_i} + \Delta \mathbf{B}^{n+1} \right) \Bigg] \\
& + \frac{\Delta t^2}{2} \Bigg\{ \Bigg[\frac{\partial}{\partial x_i}(\mathbf{a}_i + \mathbf{b}_i) \left(\frac{\partial \mathbf{F}_j^n}{\partial x_j} + \frac{\partial \mathbf{G}_j^n}{\partial x_j} - \mathbf{B}^n \right) - \mathbf{d} \left(\frac{\partial \mathbf{F}_i^n}{\partial x_i} + \frac{\partial \mathbf{G}_i^n}{\partial x_i} - \mathbf{B}^n \right) \Bigg] \\
& + s_2 \Bigg[\frac{\partial}{\partial x_i}(\mathbf{a}_i + \mathbf{b}_i) \left(\frac{\partial \Delta \mathbf{F}_j^{n+1}}{\partial x_j} + \frac{\partial \Delta \mathbf{G}_j^{n+1}}{\partial x_j} - \Delta \mathbf{B}^{n+1} \right) \\
& - \mathbf{d} \left(\frac{\partial \Delta \mathbf{F}_i^{n+1}}{\partial x_i} + \frac{\partial \Delta \mathbf{G}_i^{n+1}}{\partial x_i} - \mathbf{B}^{n+1} \right) \Bigg] \Bigg\} + O(\Delta t^3).
\end{aligned} \tag{9}$$

In order to provide different implicitness (different numerical treatments or schemes) to different physical quantities, we reassign s_1 and s_2 associated with the diffusion and source terms, respectively,

$$\begin{aligned}
s_1 \Delta \mathbf{G}_i &\Rightarrow s_3 \Delta \mathbf{G}_i, \qquad s_1 \Delta \mathbf{B} \Rightarrow s_5 \Delta \mathbf{B}, \\
s_2 \Delta \mathbf{G}_i &\Rightarrow s_4 \Delta \mathbf{G}_i, \qquad s_2 \Delta \mathbf{B} \Rightarrow s_6 \Delta \mathbf{B},
\end{aligned} \tag{10}$$

with the various implicitness parameters defined as

s_1 = first order convection implicitness parameter,
s_2 = second order convection implicitness parameter,
s_3 = first order diffusion implicitness parameter,
s_4 = second order diffusion implicitness parameter,
s_5 = first order source term implicitness parameter,
s_6 = second order source term implicitness parameter.

The first order implicitness parameters s_1, s_3, and s_5 will be shown to be flowfield dependent with the solution accuracy assured by taking into account the flowfield gradients, whereas the second order implicitness parameters s_2, s_4, and s_6, which are also flowfield dependent, mainly act as artificial viscosity, contributing to the solution stability. Substituting these implicitness parameters as defined in Eq. (9) into Eq. (8), we obtain

$$\begin{aligned}
&\Delta \mathbf{U}^{n+1} + \Delta t \left[s_1 \left(\frac{\partial \mathbf{a}_i \Delta \mathbf{U}^{n+1}}{x_i} \right) + s_3 \left(\frac{\partial \mathbf{b}_i \Delta \mathbf{U}^{n+1}}{\partial x_i} + \frac{\partial^2 \mathbf{c}_{ij} \Delta \mathbf{U}^{n+1}}{\partial x_i \partial x_j} \right) - s_5 \mathbf{d} \Delta \mathbf{U}^{n+1} \right] \\
&\qquad - \frac{\Delta t^2}{2} \left\{ s_2 \left[\frac{\partial^2 (\mathbf{a}_i \mathbf{a}_j + \mathbf{b}_i \mathbf{a}_j \Delta \mathbf{U}^{n+1}}{\partial x_i \partial x_j} - \mathbf{d} \frac{\partial \mathbf{a}_i \Delta \mathbf{U}^{n+1}}{\partial x_i} \right] \right. \\
&\qquad + s_4 \left[\left(\frac{\partial^2 (\mathbf{a}_i \mathbf{b}_j + \mathbf{b}_i \mathbf{b}_j) \Delta \mathbf{U}^{n+1}}{\partial x_i \partial x_j} \right) - \mathbf{d} \left(\frac{\partial \mathbf{b}_i \Delta \mathbf{U}^{n+1}}{\partial x_i} + \frac{\partial^2 \mathbf{c}_{ij} \Delta \mathbf{U}^{n+1}}{\partial x_i \partial x_j} \right) \right] \\
&\qquad \left. - s_6 \left[\mathbf{d} \frac{\partial (\mathbf{a}_i + \mathbf{b}_i) \mathbf{U}^{n+1}}{\partial x_i} - \mathbf{d} \Delta \mathbf{U}^{n+1} \right] \right\} \\
&\quad + \Delta t \left(\frac{\partial \mathbf{F}_i^n}{\partial x_i} + \frac{\partial \mathbf{G}_i^n}{\partial x_i} - \mathbf{B}^n \right) - \frac{\Delta t^2}{2} \left[\frac{\partial}{\partial x_i} (\mathbf{a}_i + \mathbf{b}_i) \left(\frac{\partial \mathbf{F}_j^n}{\partial x_j} + \frac{\partial \mathbf{G}_j^n}{\partial x_j} - \mathbf{B}^n \right) \right. \\
&\qquad \left. - \mathbf{d} \left(\frac{\partial \mathbf{F}_i^n}{\partial x_i} + \frac{\partial \mathbf{G}_i^n}{\partial x_i} - \mathbf{B}^n \right) \right] + O(\Delta t^3) = 0 , \qquad (11)
\end{aligned}$$

with

$$\Delta \mathbf{B}^{n+1} = \frac{\partial \mathbf{B}}{\partial \mathbf{U}} \Delta \mathbf{U}^{n+1} = \mathbf{d} \Delta \mathbf{U}^{n+1} .$$

Rearranging Eq. (11), we obtain

$$\mathbf{R} = \mathbf{A} \Delta \mathbf{U}^{n+1} + \frac{\partial}{\partial x_i} \left(\mathbf{E}_i \Delta \mathbf{U}^{n+1} \right) + \frac{\partial^2}{\partial x_i \partial x_j} \left(\mathbf{E}_{ij} \Delta \mathbf{U}^{n+1} \right) + \mathbf{Q}^n + O(\Delta^3) , \qquad (12)$$

or

$$\left(\mathbf{A} + \frac{\partial}{\partial x_i} \mathbf{E}_i + \frac{\partial^2}{\partial x_i \partial x_j} \mathbf{E}_{ij} \right) \Delta \mathbf{U}^{n+1} = -\mathbf{Q}^n , \qquad (13)$$

with

$$\mathbf{A} = \mathbf{I} + \Delta t s_5 \mathbf{d} + \frac{\Delta t^2}{2} s_6 \mathbf{d}, \tag{14}$$

$$\mathbf{E}_i = \Delta t(s_1 \mathbf{a}_i + s_3 \mathbf{b}_i) + \frac{\Delta t^2}{2}[s_6 \mathbf{d}(\mathbf{a}_i + \mathbf{b}_i) + s_2 \mathbf{d}\mathbf{a}_i + s_4 \mathbf{d}\mathbf{b}_i], \tag{15}$$

$$\mathbf{E}_{ij} = \Delta t s_3 \mathbf{c}_{ij} - \frac{\Delta t^2}{2}[s_2(\mathbf{a}_i\mathbf{a}_j + \mathbf{b}_i\mathbf{a}_j) + s_4(\mathbf{a}_i\mathbf{b}_j + \mathbf{b}_i\mathbf{b}_j - \mathbf{d}\mathbf{c}_{ij})], \tag{16}$$

$$\mathbf{Q}^n = \frac{\partial}{\partial x_i}\left[\left(\Delta t + \frac{\Delta t^2}{2}\mathbf{d}\right)(\mathbf{F}_i^n + \mathbf{G}_i^n) + \frac{\Delta t^2}{2}(\mathbf{a}_i + \mathbf{b}_i)\mathbf{B}^n\right] - \frac{\partial^2}{\partial x_i \partial x_j}\left[\frac{\partial t^2}{2}(\mathbf{a}_i + \mathbf{b}_i)(\mathbf{F}_j^n + \mathbf{G}_j^n)\right] - \left(\Delta t + \frac{\Delta t^2}{2}\mathbf{d}\right)\mathbf{B}^n. \tag{17}$$

An alternative scheme is to allow the source term in the left hand side (LHS) of Eq. (13) to lag from $n+1$ to n so that Eq. (13) may be written as

$$\left(\mathbf{I} + \frac{\partial}{\partial x_i}\mathbf{E}_i + \frac{\partial^2}{\partial x_i \partial x_j}\mathbf{E}_{ij}\right)\Delta \mathbf{U}^{n+1} = \mathbf{Q}^n, \tag{18}$$

with

$$\mathbf{Q}^n = \frac{\partial}{\partial x_i}\left[\left(\Delta t + \frac{\Delta t^2}{2}\mathbf{d}\right)(\mathbf{F}_i^n + \mathbf{G}_i^n) + \frac{\Delta t^2}{2}(\mathbf{a}_i + \mathbf{b}_i)\mathbf{B}^n\right] - \frac{\partial^2}{\partial x_i \partial x_j}\left[\frac{\Delta t^2}{2}(\mathbf{a}_i + \mathbf{b}_i)(\mathbf{F}_j^n + \mathbf{G}_j^n)\right] - \left(\Delta t s_5 + \frac{\Delta t^2}{2}s_6\right)\mathbf{d}\Delta \mathbf{U}^n - \left(\Delta t + \frac{\Delta t^2}{2}\mathbf{d}\right)\mathbf{B}^n. \tag{19}$$

Note that the Beam-Warming scheme [1] can be written in the form identical to Eq. (18) with the following definitions of $\mathbf{E}_i$, $\mathbf{E}_{ij}$ and $\mathbf{Q}^n$:

$$\mathbf{E}_i = m\Delta t(\mathbf{a}_i + \mathbf{b}_i), \quad \text{with } m = \frac{\theta}{1+\xi}, \tag{20}$$

$$\mathbf{E}_{ij} = m\Delta t \mathbf{c}_{ij}, \tag{21}$$

$$\mathbf{Q}^n = \frac{\Delta t}{1+\xi}\left(\frac{\partial \mathbf{F}_i^n}{\partial x_i} + \frac{\partial \mathbf{G}_i^n}{\partial x_i}\right) + \frac{\xi}{1+\xi}\Delta \mathbf{U}^n, \tag{22}$$

where the cross derivative terms appearing in $\mathbf{Q}^n$ for the Beam-Warming scheme are included in the second derivative terms on the LHS. The Beam-Warming scheme is seen to be a special case of the FDMEI equations if we set $s_1 = s_3 = m$, $s_2 = s_4 = s_5 = s_6 = 0$, in Eq. (18), with adjustments of $\mathbf{Q}^n$ on the right hand side (RHS) as

in Eq. (22). The stability analysis of the Beam-Warming scheme requires $\xi \geq 0.385$ and $\theta = 1/2 + \xi$. This will fix the implicitness parameter m to be $0.639 \leq m \leq 0.75$. It can be shown that the FDMEI equations as derived in Eq. (13) or Eq. (18) are capable of producing practically all existing FDM and FEM schemes. Some examples are shown in [9].

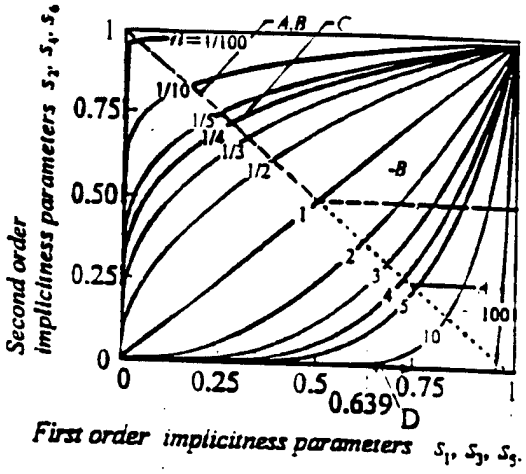

Figure 2. Relationships between the first and second order implicitness parameters. *A* — $s_2 = 1 - s_1$, $s_4 = 1 - s_3$, $s_6 = 1 - s_5$; *B* — $s_2 = \max(1 - s_1, 0.5)$, $s_4 = \max(1 - s_3, 0.5)$, $s_6 = \max(1 - s_5, 0.5)$; *C* — $s_2 = s_1^n$, $s_4 = s_3^n$, $s_6 = s_5^n$, $0 < n < 1$; *D* — Beam-Warming Criterion

Contrary to the Beam-Warming scheme, the FDMEI approach is to obtain the implicitness parameters from the current flowfield variables at each and every nodal point rather than fixing the implicitness parameters to certain predetermined numbers and using them for the entire flow domain irrespective of the local flowfield variation from one point to another. In FDMEI scheme, these implicitness parameters may be determined for spatial and temporal bases as depicted in Fig. 2. The final values of implicitness parameters at any point and at any time can be obtained as the average of both spatial and temporal contributions:

Convection Implicitness Parameters:

$$s_1 = \begin{cases} \min(r, 1) & r > \alpha \\ 0 & r < \alpha, M_{min} \neq 0 \\ 1 & M_{min} = 0 \end{cases} \qquad s_2 = s_1^n, 0 < n < 1 \tag{23}$$

with

$$r = \frac{\sqrt{M_{max}^2 - M_{min}^2}}{M_{min}}, \tag{24}$$

where the maximum and minimum Mach numbers are calculated between adjacent nodal points in FDM or within a local finite element in FEM for spatial implicitness parameters and between the time step at n and $n-1$ for temporal implicitness parameters, and α is a user-specified small number ($\alpha \cong 0.01$). Here it is seen that s_1 is directly related to the flowfield, whereas s_2 depends on s_1 such that $s_2 = s_1^n$. The primary role of s_1 is to ensure the solution accuracy by properly accommodating the convection gradients, whereas that of s_2 is to act as artificial viscosity, for solution stability.

Diffusion Implicitness Parameters:

$$s_3 = \begin{cases} \min(s,1) & s > \beta \\ 0 & s < \beta\,, Re_{min} \neq 0\,, \text{ or } Pe_{min} \neq 0 \\ 1 & Re_{min} = 0\,, \text{ or } Pe_{min} = 0 \end{cases} \qquad s_4 = s_3^n\,, 0 < n < 1 \tag{25}$$

with

$$s = \frac{\sqrt{Re_{max}^2 - Re_{min}^2}}{Re_{min}}\,, \tag{26a}$$

or

$$s = \frac{\sqrt{Pe_{max}^2 - Pe_{min}^2}}{Pe_{min}}\,, \tag{26b}$$

where the maximum and minimum Reynolds numbers or maximum and minimum Peclet numbers are calculated similarily as in s_1 for spatial and temporal implicitness parameters, and β is a user-specified small number ($\beta \cong 0.01$). If temperature gradients are large, it is possible that Peclet numbers instead of Reynolds numbers will dictate the diffusion implicitness parameters. The larger value of s_3 is to be chosen, as obtained either from Eq. (26*a*) or (26*b*). Note also that $s_4 = s_3^n$ with s_3 ensuring the solution accuracy by taking into account the diffusion gradients, and here again, s_4 plays the role of artificial viscosity, for solution stability.

Source Term Implicitness Parameters:

For the case of chemically reacting flows the Da (Damköhler number) must be used

$$s_5 = \begin{cases} \min(t,1) & t \geq \gamma \\ 0 & t < \gamma\,, Da_{min} \neq 0 \\ 1 & Da_{min} = 0 \end{cases} \qquad s_6 = s_5^n\,, 0 < n < 1 \tag{27}$$

with

$$t = \frac{\sqrt{Da_{max}^2 - Da_{min}^2}}{Da_{min}}\,, \tag{28}$$

where the maximum and minimum Damköhler numbers are calculated similarily as in s_1 and s_3 for spatial and temporal implicitness parameters, and γ is a user-specified small number ($\gamma \cong 0.01$). The relationship between s_5 and s_6 is similar to those for convection and diffusion implicitness parameters such that $s_6 = s_5^n$ with s_5 and s_6 controlling the solution accuracy and solution stability, respectively. The average of both spatial and temporal implicitness parameters will be adopted for use in computations at any point (element) and time.

Relationships between all physical phenomena and the corresponding numerical treatments are characterized by the balance between the first order implicitness parameters (s_1, s_3, s_5) and the second order implicitness parameters (s_2, s_4, s_6),

ensuring the computational accuracy and computational stability, respectively. The idea is to provide adequate (no more and no less than required) amount of numerical viscosity in order to preserve the computational accuracy. Note that the definitions for the second order implicitness parameters have been modified from those reported in [7, 8] in order to meet the above requirements. Initially, it was thought that the second order implicitness parameters should be the direct opposite compliances of the first order implicitness parameters ($s_2 = 1 - s_1$, $s_4 = 1 - s_3$, $s_6 = 1 - s_5$) [8] such that the second order implicitness parameters are the maximum and minimum, respectively, for the minimum and maximum values of the first order implicitness parameters. Unfortunately, such definition resulted in too little numerical viscosities for the high values of the first order implicitness parameters. Subsequently, the limiting values (0.5) of the second order implicitness parameters were provided such that $s_2 = \max(1 - s_1, 0.5)$, *etc.* as experimented in [7]. However, it was noted that both first and second order parameters should assume the same values at the both extremes at zero and unity with the second order implicitness parameters being reasonably large for all values of the first order implicitness parameters. Thus, the second order implicitness parameters given above are the nonlinear continuous functions of the first order implicitness parameters satisfying these requirements. The range of the constant n is $0 < n < 1$, although $n \cong 1/4$ has been found to be the optimum, exhibiting the best convergence rate for reasonably high CFL numbers in the example problems presented in Section 4.

The flowfield dependent implicitness parameters as defined above are capable of allowing various numerical schemes to be automatically generated, as summarized as follows:

(1) The first order implicitness parameters s_1 and s_3 control all high gradient phenomena such as shock waves and turbulence. These parameters as calculated from the changes of local Mach numbers and Reynolds (or Peclet) numbers within each element and are indicative of the actual local element flowfields. The contours of these parameters closely resemble the flowfields themselves, with both s_1 and s_3 being large (close to unity) in regions of high gradients, but small (close to zero) in regions where the gradients are small. The basic role of s_1 and s_3 is to provide computational accuracy.

(2) The second order implicitness parameters s_2 and s_4 are also flowfield dependent. However, their primary role is to provide adequate computational stability (artificial viscosity) as they were originally introduced into the second order time derivative term of the Taylor series expansion of the conservation flow variables U^{n+1}. The primary role of s_2 and s_4 is to provide computational stability.

(3) The s_1 terms represent convection. This implies that if $s_1 \cong 0$ then the effect of convection is small. The computational scheme is automatically altered to

take this effect into account, with the governing equations being predominantly parabolic–elliptic. Note that these effects are confined at U^{n+1}, not at U^n.

(4) The s_3 terms are associated with diffusion. Thus, with $s_3 \cong 0$, the effect of viscosity or diffusion is small and the computational scheme is automatically switched to that of Euler equations where the governing equations are predominantly hyperbolic.

(5) If the first order implicitness parameters s_1 and s_3 are nonzero, this indicates a typical situation for the mixed hyperbolic, parabolic and elliptic nature of the Navier–Stokes system of equations, with convection and diffusion being equally important. This is the case for incompressible flows at low speeds. The unique property of the FDMEI scheme is its capability to control pressure oscillations adequately without resorting to the separate hyperbolic elliptic pressure equation for pressure corrections. The capability of FDMEI scheme to handle incompressible flows is achieved by a delicate balance between s_1 and s_3 as determined by the local Mach numbers and Reynolds (or Peclet) numbers. If the flow is completely incompressible ($M = 0$), the criteria given by Eq. (19) leads to $s_1 = 1$, whereas the implicitness parameter s_3 is to be determined according to the criteria given in Eq. (21). Make a note of the presence of the convection–diffusion interaction terms given by the product of $\mathbf{b}_i\mathbf{a}_j$ in the s_2 terms and $\mathbf{a}_i\mathbf{b}_j$ in the s_4 terms. These terms allow interactions between convection and diffusion in the viscous incompressible and/or viscous compressible flows.

(6) If temperature gradients rather than velocity gradients dominate the flowfield, then s_3 is governed by the Peclet number rather than by the Reynolds number. Such cases arise in high speed, high temperature compressible flows close to the wall.

(7) In the case of reacting flows the source terms B contains the reaction rates which are functions of the flowfield variables. With widely disparate time and length scales involved in the fast and slow chemical reaction rates of various chemical species as characterized by Damköhler numbers, the first order source term implicitness parameter s_5 is instrumental in dealing with the stiffness of the resulting equations to obtain convergence to accurate solutions. On the other hand, the second order source term implicitness parameter s_6 contribute to the stability of solutions. It is seen that the criteria given by Eq. (23), (24) will adjust the reaction rate terms in accordance with the ratio of the diffusion time to the reaction time in finite rate chemistry so as to assure the accurate solutions with computational stability.

(8) Various definitions of Peclet number and Damköhler numbers (Table 1) between the energy and species equations should be checked. Whichever definition provides larger values of s_3 and s_5 must be used.

(9) The transition to turbulence is a natural flow process as the Reynolds number increases, causing the gradients of any or all flow variables to increase. This phenomenon is the physical instability and is detected by the increase of s_3 if the flow is incompressible, but by both s_3 and s_1 if the flow is compressible. Such physical instability is likely to trigger the numerical instability, but will be countered by the second order implicitness parameters s_2 and/or s_4 to ensure numerical stability automatically. In this process, these flowfield dependent implicitness parameters are capable of capturing relaminarization, compressibility effect or dilatational turbulent energy dissipation, and turbulent unsteady fluctuations.

(10) An important contribution of the first order implicitness parameters is the fact that they can be used as error indicators for adaptive mesh generations. That is, the larger the implicitness parameters the higher the gradients of any flow variables. Whichever governs (largest first order implicitness parameters) will indicate the need for mesh refinements. In this case, all variables (density, velocity, pressure, temperature, species mass fraction) participate in resolving the adaptive mesh, contrary to the conventional definitions of the error indicators.

(11) Physically, the implicitness parameters will influence the magnitudes of Jacobians. Thus, Item 8 above may be modified so that the diffusion implicitness parameters s_3 and s_4 as calculated from Reynolds number and Peclet number can be applied to the Jacobians (a_i, b_i, c_{ij}), corresponding to the momentum equations and energy equation, respectively. Furthermore, two different definitions of Peclet number (Pe_I, Pe_{II}) would require the s_3 and s_4 as calculated from the energy and species equations to be applied to the corresponding terms of the Jacobians. Similar applications for the source term implicitness parameters s_5 and s_6 should be followed for the source term Jacobian d. In this way, high temperature gradients arising from the momentum and energy equations and the finite rate chemistry governed by the energy and species equations can be resolved accordingly.

The FDMEI equations as given in Eq. (12) may be solved by either FDM or FEM. The standard linear Galerkin approximations of FEM lead to the results of central differences of FDM. However, the main difference between FDM and FEM arises when integration by parts is performed in FEM and the explicit terms of Neumann boundary conditions "naturally" appear as boundary integral forms. Thus, all Neumann boundary conditions can be directly specified at boundaries in FEM.

Table 1. Definitions of nondimentional flow variables

$$\underbrace{\rho(v\cdot\nabla)v}_{A} = \underbrace{-\nabla p}_{B} + \underbrace{\mu[\nabla^2 v + \frac{1}{3}\nabla(\nabla\cdot v)]}_{C}$$

$$\underbrace{\nabla\cdot\rho v\int_{T_0}^{T} c_{pk}\,dT}_{E} - \underbrace{\nabla\cdot k\nabla T}_{F} - \underbrace{\nabla\cdot\left(\rho D\nabla Y_k\int_{T_0}^{T} c_{pk}\,dT\right)}_{G} = \underbrace{-\sum_{k=1}^{N} H_k^{\circ} w_k}_{N}$$

$$\underbrace{\nabla\cdot(\rho Y_k v)}_{I} - \underbrace{\nabla\cdot(\rho D\nabla Y_k)}_{J} = \underbrace{w_k}_{K}$$

Mach number	M	$\frac{u}{a}$	$\frac{A}{B} = \frac{\text{inertial force}}{\text{pressure force}}$
Reynolds number	Re	$\frac{\rho u L}{\mu}$	$\frac{A}{C} = \frac{\text{inertial force}}{\text{viscous force}}$
Peclet number, I	Pe_I	$\frac{\rho u L c_{pk}}{k}$	$\frac{E}{F} = \frac{\text{convective heat transfer}}{\text{conductive heat transfer}}$
Peclet number, II	Pe_{II}	$\frac{uL}{D}$	$\frac{I}{J} = \frac{\text{convective mass transfer}}{\text{diffusive mass transfer}}$
Damköhler number, I	Da_I	$\frac{L w_k}{\rho u Y_k}$	$\frac{K}{I} = \frac{\text{mass source}}{\text{convective transfer}}$
Damköhler number, II	Da_{II}	$\frac{L^2 w_k}{\rho D Y_k}$	$\frac{K}{J} = \frac{\text{mass source}}{\text{diffusive transfer}}$
Damköhler number, III	Da_{III}	$\frac{qL}{Hu}$	$\frac{N}{E} = \frac{\text{heat source}}{\text{convective heat transfer}}$
Damköhler number, IV	Da_{IV}	$\frac{qL^2}{kT}$	$\frac{N}{F} = \frac{\text{heat source}}{\text{conductive heat transfer}}$
Damköhler number, V	Da_V	$\frac{qL^2}{HD}$	$\frac{N}{G} = \frac{\text{heat source}}{\text{diffusive heat transfer}}$

This is not the case for FDM. Often, a rather cumbersome process must be taken for Neumann boundary conditions in FDM.

When dealing with all speed flow regimes such as in shock wave turbulent boundary layer interactions where compressible and incompressible flows, viscous and inviscid flows, and laminar and turbulent flows are intermingled throughout the flowfield domain, a computational scheme intended for only one type of flow physics and that does not account for other types of flow phenomena will fail. For example, the flow close to the wall in shock wave turbulent boundary layer interactions is incompressible ($M \leq 0.1$), whereas away from the wall the flow is compressible (supersonic or hypersonic). In this case, viscous flows change to inviscid flows. In between these two extremes the flowfield changes continuously, oscillating back and forth across the boundary layers of velocity and entropy, and leading edge and bow shocks. At any given computational nodal point or element, gradients of each variable (density, pressure, velocity, and temperature) may be very small or very large, so large that practically all currently available computational methods may fail. In order to succeed, it is necessary that the current flow physics everywhere be identified and so recognized, with specific computational schemes accorded to each and every computational nodal point and element. It is clear that such accommodations are available in FDMEI scheme.

3 IMPLEMENTATION AND COMPUTATIONAL PROCESS

As stated earlier, the governing equations for the Taylor series-modified Navier–Stokes system of equations, (12) may be applied to either FDM or FEM, or to the finite volume method (FVM). For FDM applications the first order and second order spatial derivatives may be written in central difference schemes. For example, we may write for any variable u as

$$\frac{\partial u}{\partial x}\Big|_{i,j} = \frac{u_{i+1,j} - u_{i-1,j}}{2\Delta x} \tag{29}$$

$$\frac{\partial^2 u}{\partial x^2}\Big|_{i,j} = \frac{u_{i+1,j} - 2u_{i,j} + u_{i-1,j}}{\Delta x^2} \tag{30}$$

with analogous formulas for the y derivatives in two-dimensions or corresponding extensions to three-dimensional problems.

For applications to FEM we begin by expressing the conservation and flux variables and source terms as a linear combination of trial functions Φ_α with the nodal values of these variables.

$$\begin{aligned} \mathbf{U}(\mathbf{x},t) &= \Phi_\alpha(\mathbf{x})\mathbf{U}_\alpha(t) \quad , & \mathbf{F}_i(\mathbf{x},t) &= \Phi_\alpha(\mathbf{x})\mathbf{F}_{\alpha i}(t) \\ \mathbf{G}_i(\mathbf{x},t) &= \Phi_\alpha(\mathbf{x})\mathbf{G}_{\alpha i}(t) \quad , & \mathbf{B}_i(\mathbf{x},t) &= \Phi_\alpha(\mathbf{x})\mathbf{B}_\alpha(t) \end{aligned} \tag{31}$$

Applying the generalized Galerkin approximations to Eq. (13) we obtain:

$$\int_\Omega \Phi_\alpha \mathbf{R}(\mathbf{U}, \mathbf{F}_i, \mathbf{G}_i, \mathbf{B})\, d\Omega = 0 \tag{32}$$

or

$$(A_{\alpha\beta}\eta_{rs} + B_{\alpha\beta rs})\Delta U_{\beta s}^{n+1} = H_{\alpha r}^{n} + N_{\alpha r}^{n}, \tag{33}$$

where

$$A_{\alpha\beta} = \int_{\Omega} \Phi_\alpha \Phi_\beta \, d\Omega, \quad \eta_{rs} = (1 + \Delta t s_5 + \frac{\Delta t^2}{2} s_6)\delta_{rs}, \tag{34}$$

$$\begin{aligned} B_{\alpha\beta rs} = \int_{\Omega} \Bigg[& -\Bigg\{ \Delta t(s_1 a_{irs} + s_3 b_{irs}) + \frac{\Delta t^2}{2}[s_2 d_{rt} a_{its} + s_6 d_{rt}(a_{its} + b_{its}) \\ & + s_4 d_{rt} b_{its}] \Bigg\} \Phi_{\alpha,i} \Phi_\beta - \Bigg\{ \Delta t s_3 c_{ijrs} - \frac{\Delta t^2}{2}[s_2(a_{irt} a_{jts} + b_{irt} a_{jts}) \\ & + s_4(a_{irt} b_{jts} + b_{irt} b_{jts} - d_{rt} c_{ijts})] \Bigg\} \Phi_{\alpha,i} \Phi_{\beta,j} \Bigg] \, d\Omega \\ & + \int_{\Gamma} \Bigg[\Bigg\{ \Delta t(s_1 a_{irs} + s_3 b_{irs}) + \frac{\Delta t^2}{2}[s_2 d_{rt} a_{its} + s_6 d_{rt}(a_{its} + b_{its}) \\ & + s_4 d_{rt} b_{its}] \Bigg\} \bar{\Phi}_\alpha \bar{\Phi}_\beta + \Bigg\{ \Delta t s_3 c_{ijrs} - \frac{\Delta t^2}{2}[s_2(a_{irt} a_{jts} + b_{irt} a_{jts}) \\ & + s_4(a_{irt} b_{jts} + b_{irt} b_{jts} - d_{rt} c_{ijts})] \Bigg\} \bar{\Phi}_\alpha \bar{\Phi}_{\beta,j} \Bigg] n_i \, d\Gamma, \end{aligned} \tag{35}$$

$$\begin{aligned} H_{\alpha r}^{n} = \int_{\Omega} \Bigg\{ & \Bigg[\Delta t \left(F_{\beta ir}^{n} + G_{\beta ir}^{n} \right) + \frac{\Delta t^2}{2} d_{rs} \left(F_{\beta is}^{n} + G_{\beta is}^{n} \right) \\ & + \frac{\Delta t^2}{2}(a_{irs} + b_{irs}) B_{\beta s}^{n} \Bigg] \Phi_{\alpha,i} \Phi_\beta \\ & - \frac{\Delta t^2}{2}(a_{irs} + b_{irs}) \left(F_{\beta js}^{n} + G_{\beta js}^{n} \right) \Phi_{\alpha,i} \Phi_{\beta,j} + \Bigg[\Delta t B_{\beta,r}^{n} \\ & + \frac{\Delta t^2}{2} d_{rs} B_{\beta s}^{n} \Bigg] \Phi_\alpha \Phi_\beta \Bigg\} \, d\Omega, \end{aligned} \tag{36}$$

$$\begin{aligned} N_{\alpha r}^{n} = \int_{\Gamma} \Bigg\{ & \Bigg[-\Delta t \left(F_{\beta ir}^{n} + G_{\beta ir}^{n} \right) - \frac{\Delta t^2}{2} d_{rs} \left(F_{\beta is}^{n} + G_{\beta is}^{n} \right) \\ & - \frac{\Delta t^2}{2}(a_{irs} + b_{irs}) B_{\beta s}^{n} \Bigg] \bar{\Phi}_\alpha \bar{\Phi}_\beta \\ & + \frac{\Delta t^2}{2}(a_{irs} + b_{irs}) \left(F_{\beta js}^{n} + G_{\beta js}^{n} \right) \bar{\Phi}_\alpha \bar{\Phi}_{\beta,j} \Bigg\} n_i \, d\Gamma, \end{aligned} \tag{37}$$

where all Jacobians must be updated at each iteration step, $\dot{\Phi}_\alpha$ represents the Neumann boundary trial and test functions, with α, β denoting the global node number and r, s providing the number of conservation variables at each node. For three dimensions, $i, j = 1,2,3$ associated with the Jacobians imply directional identification of each Jacobian matrix (a_1, a_2, a_3, b_1, b_2, b_3, c_{11}, c_{12}, c_{13}, c_{21}, c_{22}, c_{23}, c_{31}, c_{32}, c_{33}) with r, $s = 1,2,3,4,5$ denoting entries of each of the 5×5 Jacobian matrices. Note also that the relation (18) may be used to move the delta source terms to the RHS of Eq. (33) instead of lagging the source terms one time step behind. These indices can be reduced similarly for 2-D. The FEM equations given by Eq. (33) are referred to as FDMEI-FEM. The counterpart of Eq. (33) based on FDM schemes of Eqs. (29) and (30) is to be called FDMEI-FDM.

It is important to realize that the integration by parts as applied to the generalized Galerkin approximations in FEM produces all Neumann boundary integrals. It is particularly advantageous that Neumann boundary conditions through re-evaluation of Jacobians normal to the boundary surfaces can simply be added to the boundary nodes for the stiffness matrix $B_{\alpha\beta rs}$ in Eq. (35). On the other hand, all Neumann boundary conditions which appear in Eq. (37) act as source terms. These features are absent in FDM, but implementations of Neumann boundary conditions can be handled by devising special forms of finite differences at boundary nodes.

Similar results are obtained either by FDM or FEM with accuracy of computations derived primarily from the FDMEI Eqs. (12). However, with the increase of Reynolds number (say around $Re \gg 10^6$), it is possible that accuracy may increase with applications of special functions such as Legendre polynomials of high degree modes characterizing extremely small turbulent microscales. Implementation of such high frequency modes can be achieved by placing these modes between the corner nodes of isoparametric finite elements. Adaptively, such high modes can be chosen as needed for the resolution of turbulent microscales. Once again the diffusion implicitness parameter s_3 will play a crucial factor in determining the required degrees of Legendre polynomial. The use of Legendre polynomial spectral modes superimposed onto isoparametric elements has been discussed in [7]. Its merit, however, has not yet been fully established for general applications.

One of the most significant aspects of the FDMEI scheme is that for low Mach numbers (incompressible flow) the scheme will automatically adjust itself to prevent pressure oscillations. This adjustment is analogous to the pressure correction scheme employed for incompressible flows. Otherwise, the FDMEI scheme is capable of shock wave resolutions at high Mach numbers, and particularly well suited for dealing with interactions between shock waves and turbulent boundary layers where regions of high and low Mach numbers and Reynolds numbers coexist. In this case, the inviscid and viscous interactions are allowed to take place. To this end the second order implicitness parameters play the role of artificial viscosity

needed for shock wave resolutions in the presence of flow diffusion due to physical viscosity.

In order to understand how the FDMEI scheme handles computations involving both compressible and incompressible flows fundamental definitions of pressure must be recognized. Consider in the following that the fluid is a perfect gas and that the total energy is given by

$$E = c_p T - \frac{p}{\rho} + \frac{1}{2} v_i v_i . \tag{38}$$

The momentum equation for steady state incompressible rotational flow may be integrated to give

$$\int (p + \frac{1}{2}\rho v_j v_j)_{,i}\, dx_i = \int \left[\mu \left(v_{i,jj} + \frac{1}{3} v_{j,ji} \right) + \rho \varepsilon_{ijk} v_j \omega_k \right] dx_i ,$$

$$p + \frac{1}{2}\rho v_j v_j = p_o + W , \tag{39}$$

with

$$W = \frac{1}{m} \int [\mu (v_{i,jj} + \frac{1}{3} v_{j,ji}) + \rho \varepsilon_{ijk} v_j \omega_k]\, dx_i ,$$

where ω_k is the component of a vorticity vector, p_o is the constant of integration, and m denotes the spatial dimension. Combining Eqs. (40) and (41) leads to the following relationship:

$$p_o = \rho (c_p T + v_i v_i - E) - W . \tag{40}$$

If p_o as given by Eq. (40) remains a constant, equivalent to a stagnation pressure, then the compressible flow as assumed in the conservation form of the Navier–Stokes system of equations has now been turned into an incompressible flow, which is expected to occur when the flow velocity is sufficiently reduced (approximately $0.1 \leq M < 0.3$ for air). Thus, Eq. (40) may serve as an equivalent equation of state for an incompressible flow. This can be identified element by element for the entire domain. Note that conservation of mass is achieved for incompressible flows with p_o in Eq. (40) being constant, thus keeping the pressure from oscillating.

Once the Navier–Stokes solution via FDMEI is carried out and all flow variables determined, then we compute fluctuations f' of any variable f,

$$f' = f - \overline{f} , \tag{41}$$

where f and $\overline{f}$ denote the Navier–Stokes solution and its time average, respectively. This process may be replaced by the fast Fourier transform of the Navier–Stokes solution. Unsteady turbulence statistics (turbulent kinetic energy, Reynolds stresses, and various energy spectra) can be calculated once the fluctuation quantities of all variables are determined.

Before we demonstrate numerical examples, let us summarize why the FDMEI scheme is capable of handling low speed and high speed and compressible and incompressible flows, including shock waves and turbulent flows:

(1) How is the transition from incompressible flow to compressible flow naturally and automatically accommodated without using two separate equations or two separate codes? This process is dictated by the first order convection implicitness parameter s_1 as reflected by the Mach number changes and the expression of the stagnation pressure.

(2) How is the shock wave captured? As the Mach number increases and its discontinuity is abrupt, the s_2 terms associated with second order derivatives together with squares of the convection Jacobian provide adequate numerical viscosities through second order derivatives, similarly as the Lax–Wendroff scheme.

(3) How is the transition from laminar to turbulent flows naturally and automatically accommodated? This process is governed by the first and second order diffusion implicitness parameters (s_3 and s_4) as calculated from the changes of the Reynolds number. The terms associated with s_3 and s_4 are responsible for fluctuations of velocities, with the values of these implicitness parameters increasing with intensities of turbulence in conjuction with the diffusion gradient Jacobian and the squares of the diffusion Jacobian. This process allows the Navier–Stokes solutions to contain fluctuations which can be extracted by subtracting the time averages of the Navier–Stokes solutions.

(4) How do the interactions between convection and diffusion take place? Changes of Mach numbers and Reynolds numbers as reflected by both convection and diffusion implicitness parameters close to the wall contribute to the unsteadiness. Away from the wall, they contribute to the transition between incompressible to compressible flows.

4 APPLICATIONS

We examine first a nonreacting flow problem with shock wave turbulent boundary layer interactions on a compression corner, followed by the reacting flow with a flat plate transverse fuel injection combustor. In these examples, 2-D isoparametric finite elements are used [8].

4.1 Supersonic Nonreacting Flow on a Compression Corner

In this example we demonstrate calculations of supersonic flow on a compression corner. The inlet boundary conditions (nondimensionalized) are $\rho = 1$, $M = 2.25$, $p = 0.14$, $Re = 105$, $Pr = 0.72$, and $v = 0$, with adiabatic wall condition. The steady state background mean flowfields for the comopression corner are shown in Fig. 3*a*. In these calculations, all perturbation(fluctuation) variables are determined from time averages of the Navier–Stokes solutions according to Eq. (41).

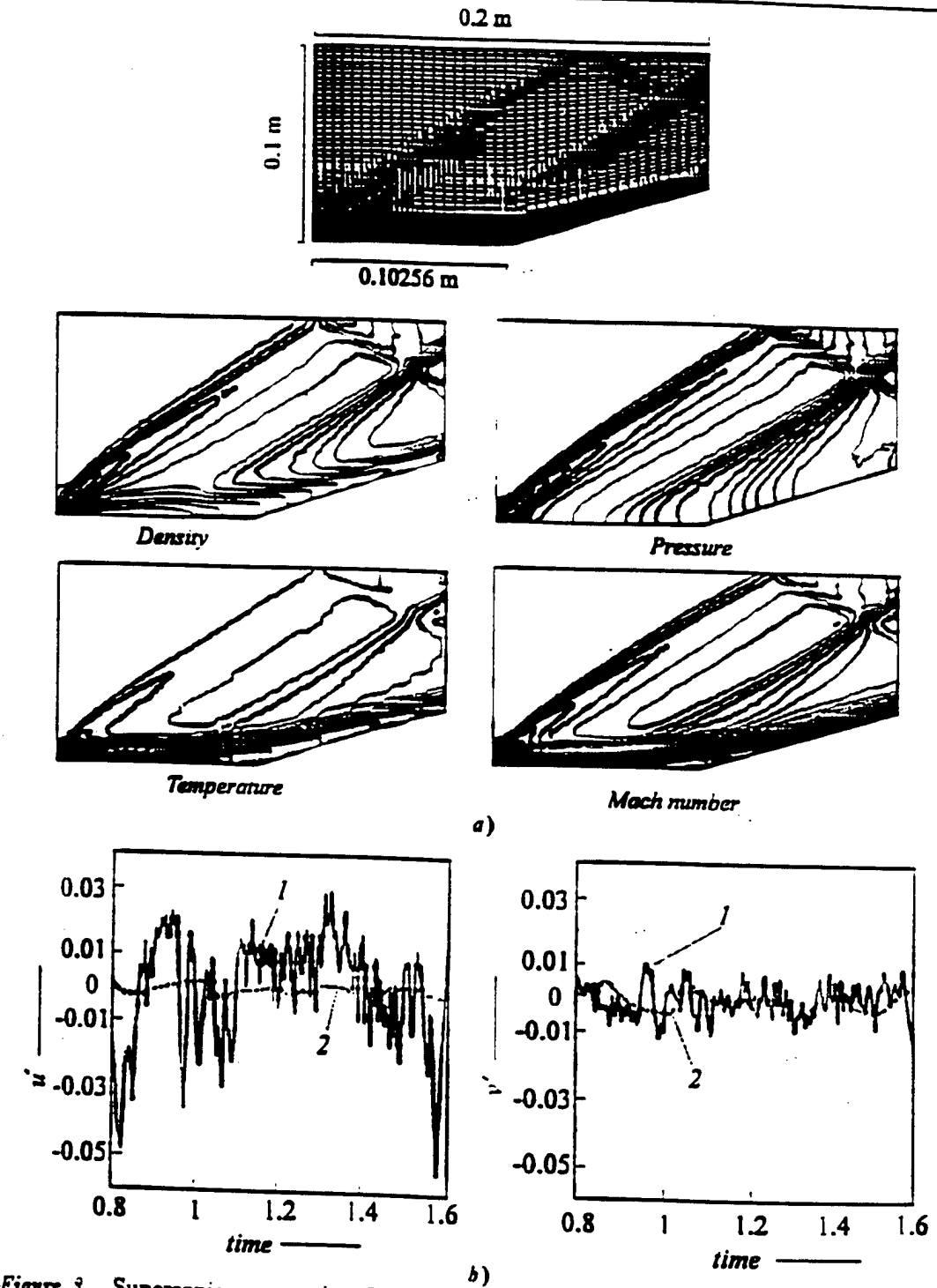

Figure 3. Supersonic nonreacting flow on a compression corner. (*a*) Compression corner geometry and flowfields. (*b*) fluctuation velocities, *1* — $x = 0.102$ m, $y = 0.001$ m; *2* — $x = 0.102$ m, $y = 0.004$ m

The horizontal and vertical perturbation velocities (u', and v') at locations close to the wall ($x = 0.10256$ m, $y = 0.001$ m) and away from the wall ($x = 0.10256$ m, $y = 0.04$ m) are shown in Fig. 3*b*. Note that u' is extremely unsteady whereas v' is significantly less unsteady close to the wall. Away from the wall, both u' and v' are almost steady. These trends are reflected in the turbulence (Reynolds) stresses as shown in Fig. 4.

Turbulent kinetic energy distributions at the locations upstream of the corner ($x = 0.0513$ m) and downstream of the corner ($x = 0.1333$ m) are shown in Fig. 5. We observe that the turbulent kinetic energy downstream of the corner is considerably larger than the upstream. No turbulent statistics calculations (wave numbers or frequencies *vs.* power spectral density) are attempted at this time as turbulence microscales are not resolved in this example.

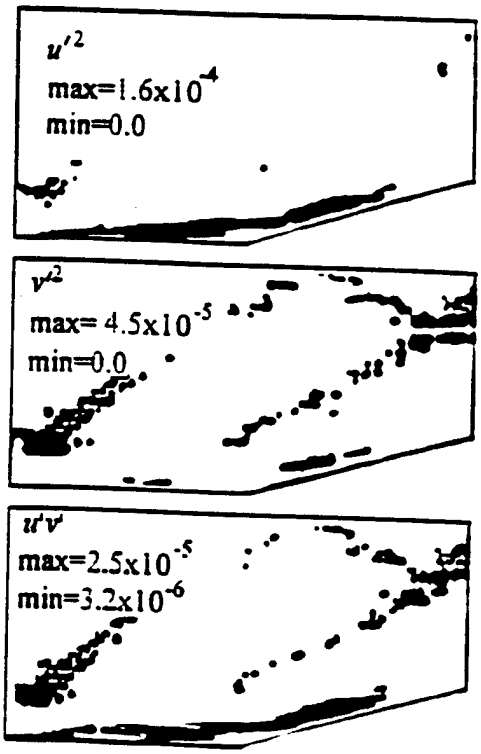

Figure 4. Supersonic nonreacting flow on a compression corner. Reynolds stresses

It should be noted that the above results obtained without turbulence models or without the standard DNS solutions (neither spectral nor DNS mesh refinements) are regarded as the consequence of the time-averaging of the FDMEI Navier–Stokes solutions. This implies that the fluctuation of variables between nodal points and between time steps as reflected in terms of the implicitness parameters (s_i) have contributed to these physical phenomena, with compressibility and shock waves dictated by the Mach number-dependent s_1, and with incompressibility and turbulent fluctuations dictated by the Reynolds number or Peclet number-dependent s_3. The simultaneous participation of s_1 and s_3 are also responsible for shock wave turbulent boundary layer interactions.

A comparison of the results of the FDMEI scheme with the k–ε turbulent model and experimantal data is shown in Fig. 6. It is seen that the FDMEI results compare more favorably with those of measurements [14].

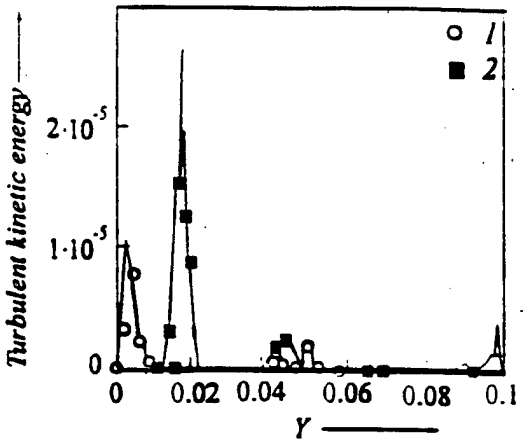

Figure 5. Supersonic nonreacting flow on a compression corner. Turbulent kinetic energy. 1 — $x = 0.051$ m, 2 — $x = 0.1333$ m

4.2 Supersonic Reacting Flow with Transverse Fuel Injector

We consider an example of transverse hydrogen fuel injector with 9 species and 18 reaction equations and a rectanglar geometry of 3615 isoparametric finite elements studied in [8]. The primary air flow is set at $M_\infty = 1$, $P_\infty = 0.1$ MPa, and $T_\infty = 1000$ K. The secondary hydrogen jet transversely injected through a slot of 2 mm is provided at $M = 1$. $P = 0.2$ MPa, and $T = 300$ K. Initially, the frozen flow with the mass fractions of 0.095 O_2 and 0.905 N_2 is analyzed, which is then used for reacting flows.

Figures 7*a,b* show density contours for the frozen and reacting cases. Notice that the density changes steadily toward vertical directions downstream of the slot for the case of frozen flow. However, for the reacting flow. there is a considerable undulation due to the formation of production species and the effect of dilation and dissipation.

In Figs. 7*c,d*, the pressure and temperature variations for the reacting flow with an isothermal wall (300 K) are shown. It is evident that the upstream boundary layer, separation and bow shocks, Mach disk and barrel shock, downstream boundary layer, and reattachment shocks appear to be smeared due to chemical reactions. Expansion waves appear downstream of the injection slot as the boundary layer is reattached (Fig. 7*c*). The static temperature increases to the maximum below the upstream boundary layer slightly toward upstream of the injection slot as a result of of the exothermic reactions (Fig. 7*d*). Downstream of the injector, cold unburned gases flowing out of the injector reduce the static temperature drastically. There is an evidence of sudden increase of temperature downstream of the reattachment shock wave due to the reignition of fuel together with an increased oxygen concentration from the main flow.

Contours of mass fractions for the reactions H_2 and O_2 and the main products OH and H_2O are shown in Figs. 7*e–h*. The large scale recirculation upstream of the injection transports the injected hydrogen within the upstream boundary layer stagnation region, resulting in a significant amount of OH and H_2O species therein. These main species together with intermediate species are carried downstream of the recirculation region. The exothermic energy thus created within the mixing layer contributes to the thrust force.

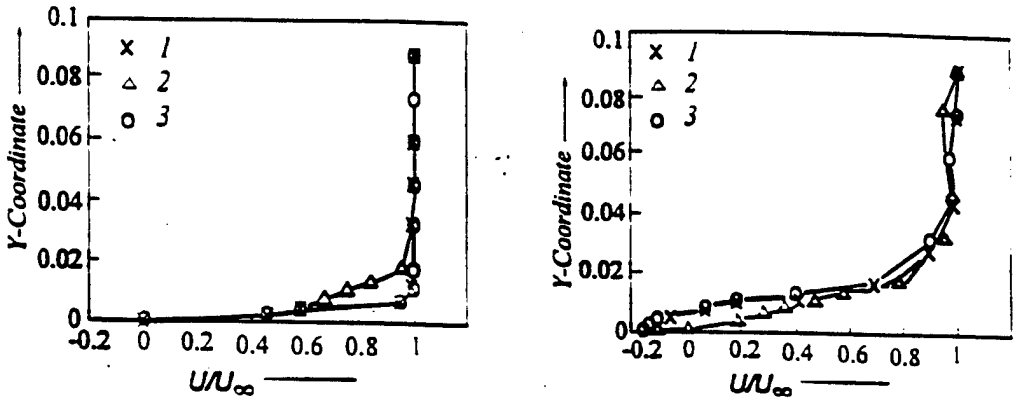

Figure 6. Supersonic nonreacting flow on a compression corner. Comparison of velocity distribution of FDMEI (*1*) scheme with k–ε (*2*) model and experimental data [14] (*3*). *a*) $x = 0.064$m, *b*) 0.1 m

5 CONCLUDING REMARKS

A new computational strategy, called the Flowfield-Dependent Mixed Explicit–Implicit(FDMEI) method has been introduced for both nonreacting and reacting flows. This method is believed to be particularly useful for supersonic combustion. The reason for this is that the source term implicitness parameters and various definitions of Damköhler number as related to the source term Jacobians play a significant role in the finite rate chemistry, especially with shock wave turbulent boundary layer interactions. Chemical reactions are either enhanced or dimisnished in the presence of complex flow physics including transition from laminar to turbulence, from incompressible to compressible, and from inviscid to viscous flows, and resulting in the various degree of efficiency in combustion.

Clearly, more extensive research will be required before the full assessment of the proposed FDMEI scheme for applications to supersonic combustion can be made. This paper, nevertheless, represents some of the preliminary results, expected certaily to be refined and reenforced in the future research.

Acknowledgement

This research was partially supported by AFOSR with Len Sakell as technical monitor and assisted by numerous former and present graduate students. Among them are K.T. Yoon, S.Y. Moon, S.A. Garcia, and G.W. Heard.

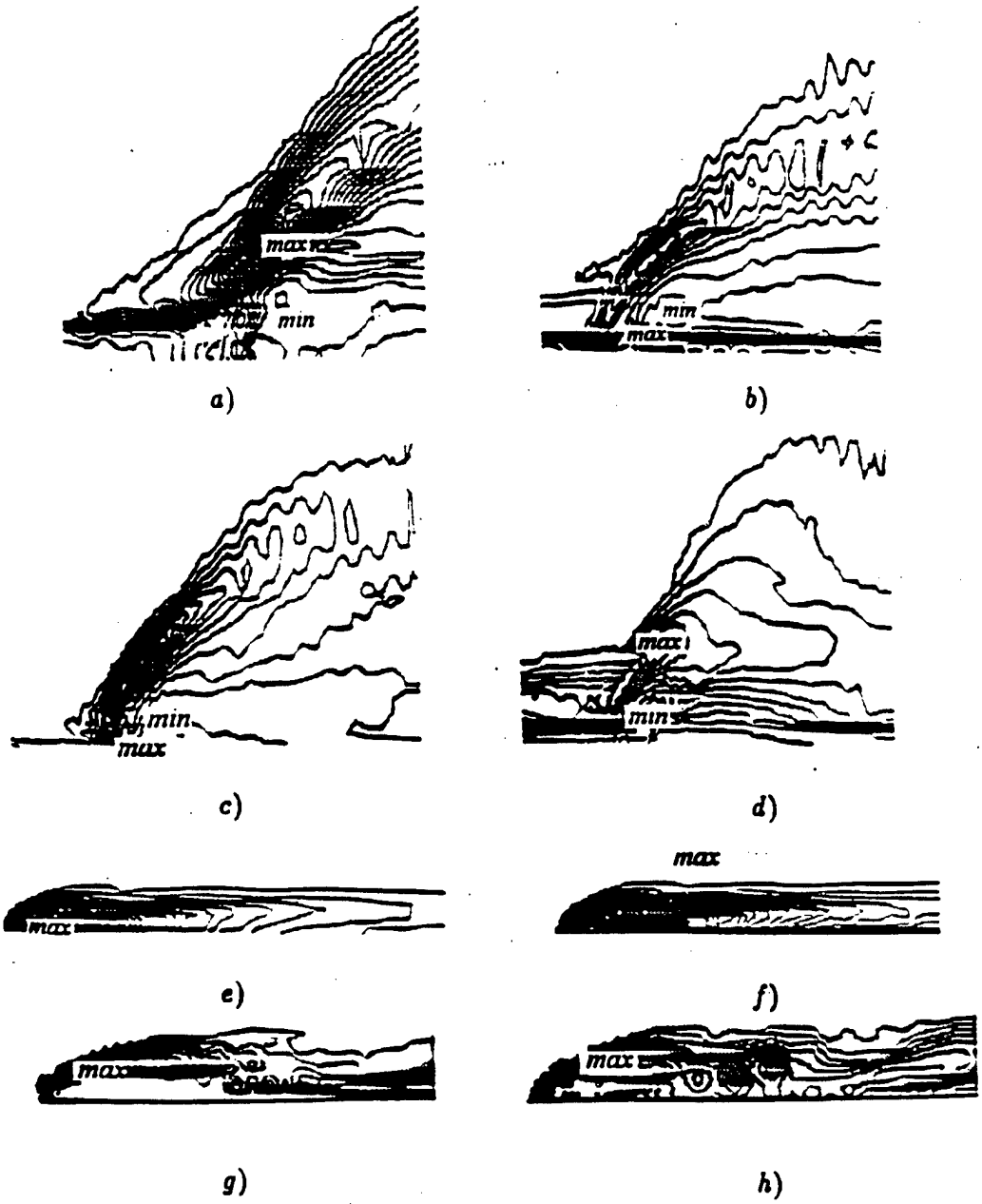

Figure 7. Various flowfield contours for transverse hydrogen fuel injection. (*a*) Density contours (frozen): max = 0.6, min = 0.058, Δ = 0.021 kg/m^3. (*b*) Density contours (reacting): max = 1.813, min = 0.0842, Δ = 0.049 kg/m^3. (*c*) Pressure contours (reacting): max = 0.4053, min = 0.0017, Δ = 0.025 MPa. (*d*) Temperature contours (reacting): max = 2982, min = 545, Δ = 195 K. (*e*) H_2 mass fraction: max = 1.0, min = 0.0, Δ = 0.024. (*f*) O_2 mass fraction: max = 0.095, min = 0.0, Δ = 0.002. (*g*) OH mass fraction: max = 0.0602, min = 0.0, Δ = 0.0024. (*h*) H_2O mass fraction: max = 0.0081, min = 0.0, Δ = 0.0003

References

[1] Beam. R.M. and Warming, R.F., "An Implicit Finite-Difference Algorithm for Hyperbolic Systems in Conservation Law Form", *J. of Computational Physics*,, **22**, 87–110, 1978.

[2] MacCormack, R.W., Current Status of Numerical Solutions of the Navier–Stokes Equations, AIAA Paper No.88–0513, 1988.

[3] Jameson, A., Schmidt, W. and Turkel, E., Numerical simulation of the Euler equations by finite volume methods using Runge-Kutta time stepping schemes. AIAA Paper No.81–1259, AIAA 5th Computational Fluid Dynamics Conference, 1981.

[4] Hirsch. C., *Numerical Computation of Internal and External Flows*. Vol. II, *Computational Methods for Inviscid and Viscous Flows*, Wiley, New York, 1990.

[5] Chung, T.J., *Finite Element Analysis in Fluid Dynamics*. McGraw-Hill, New York, 1778.

[6] Zienkiewicz, O., Codina, R., "A General Algorithm for Compressible and Incompressible Flow — Part I. The Split, Characteristic-Based Scheme", *Int. J. Numer. Meth. in Fluids*, **20**, 869–885, 1995.

[7] Yoon. K.T. and Chung, T.J., "Three-Dimensional Mixed Explicit–Implicit Galerkin Spectral Element Methods for high Speed Turbulent Compressible Flows", *Computer Methods in Applied Mechanics and Engineering*, **135**, 343–367, 1996.

[8] Moon. S.Y, Yoon, K.T., and Chung, T.J., "Numerical Simulation of Heat Transfer in Chemically Reacting Shock Wave Turbulent Boundary Layer Interactions", *Numerical Heat Transfer*, **30**, 1, Part A, 55–721996.

[9] Chung, T.J., Flowfield-Dependent Mixed Explicit–Implicit (FDMEI) Method for Compressible and Incompressible Flows, Proc. Symposium on Advances in Computational Mechanics, University of Texas, January 12–15, 1997.

[10] Drummond, J.P., Rogers, R.C., and Hussaini, M.Y., A Detailed Model of a Supersonic Reacting Mixing Layer, AIAA Paper No.86–1427, 1986.

[11] Carpenter, M.H., Thress-Dimentional Comutations of Cross-Flow Injection and Combustion in a Supersonioc Flow, AIAA Paper No.89–1870, 1989.

[12] Drummond, J.P., Carpenter, M.H., Riggins, D.W., Adams, M.S., Mixing Enhancement in a Supersonic Combustion, AIAA Paper No.89–2794, 1889.

[13] Bobskill, G., Bittner, R. Riggins, D., McClinton, C., CFD Evaluation of Mach 17 HYPULSE Scramjet Combustion Data, AIAA Paper No.91–5093, 1991.

[14] Ardonceau, P., Lee, D.H., Alziary de Roguefort, T., and Goethals, R., Turbulence Behavior in a Shock Wave/Boundary Layer Interactions, AGARD CP–271, Paper No. 8, 1980.

ELSEVIER

XP3

(Comput. Methods Appl. Mech. Engrg. [Vol.] (1997) 000–000)

Computer methods in applied mechanics and engineering

Flowfield-dependent mixed explicit–implicit (FDMEI) methods for high and low speed and compressible and incompressible flows

K.T. Yoon[*,1], S.Y. Moon[2], S.A. Garcia[2], G.W. Heard[2], T.J. Chung[3]

Department of Mechanical and Aerospace Engineering, The University of Alabama in Huntsville, Huntsville, AL 35899, USA

Received 19 February 1997

Abstract

Despite significant achievements in computational fluid dynamics, there still remain many fluid flow phenomena not well understood. For example, the prediction of temperature distributions is inaccurate when temperature gradients are high, particularly in shock wave turbulent boundary layer interactions close to the wall. Complexities of fluid flow phenomena include transition to turbulence, relaminarization, separated flows, transition between viscous and inviscid, incompressible and compressible flows, among others, in all speed regimes. The purpose of this paper is to introduce a new approach, called the *Flowfield-Dependent Mixed Explicit–Implicit* (FDMEI) method, in an attempt to resolve these difficult issues in CFD. In this process, a total of six implicitness parameters characteristic of the current flowfield are introduced. They are calculated from the current flowfield or changes of Mach numbers, Reynolds numbers, Peclet numbers, and Damköhler numbers (if reacting) at each nodal point and time step. This implies that every nodal point or element is provided with different or unique numerical scheme according to their current flowfield situations, whether compressible, incompressible, viscous, inviscid, laminar, turbulent, reacting, or nonreacting. In this procedure, discontinuities or fluctuations of all variables between adjacent nodal points are determined accurately. If these implicitness parameters are fixed to certain numbers instead of being calculated from the flowfield information, then practically all currently available schemes of finite differences or finite elements arise as special cases. Some benchmark problems to be presented in this paper will show the validity, accuracy, and efficiency of the proposed methodology.

1. Introduction

Nearly half a century has elapsed since the digital computer revolutionized computational technologies in engineering and mathematical physics. During this time finite difference methods (FDM) have dominated the field of computational fluid dynamics (CFD) [1–7], whereas the opposite is true for finite element methods (FEM) in solid mechanics. In recent years, however, the trend toward finite element methods in CFD appears to be increasingly favorable [8–14].

In general, the analyst preoccupied with the methods of his choice based on his educational background or research experience is seldom motivated to investigate other options. Thus, today the gap between these two disciplines is widely apart, despite the fact that the thorough understanding of the relations between FDM and FEM is beneficial. The purpose of this paper is an attempt to call for a new approach in which both FEM and FDM can be united toward the common goal of achieving the highest level of accuracy and efficiency in CFD. Similarities and dissimilarities must be identified in order to recognize merits and demerits of each method and to enable the analysts to choose the most desirable approach suitable for the particular task at hand.

* Corresponding author.

[1] Postdoctoral Research Associate, currently with Hyundai Aerospace Research Laboratory, Korea.

[2] Graduate Research Assistant.

[3] Distinguished Professor.

PII S0045-7825(97)00114-X

One of the most important questions in CFD is how to deal with large gradients of the variable (density, velocity, pressure, temperature, and source terms). Rapid changes of Mach numbers, Reynolds numbers, Peclet numbers, and Damköhler numbers (if reacting) between adjacent nodal points or elements can be a crucial factor in determining whether the chosen computational scheme will succeed or fail. Furthermore, proper treatments for incompressibility and compressibility, viscous and inviscid flows, subsonic and supersonic flows, laminar and turbulent flows, nonreacting and reacting flows are extremely important. The most general case of fluid dynamics where these various flow properties may be depicted in external and internal hypersonic flows is shown in Fig. 1(a,b). A typical reacting flow (hydrogen-air reaction) can also be seen in Fig. 1(c).

Can a single formulation and computer code be made available to satisfy all the requirements mentioned above? Can a single mathematical formulation lead to most of the currently available computational schemes both in FDM and FEM as special cases? Most importantly, will such an approach guarantee accuracy and efficiency? In this paper, we respond to these questions positively, based on the results obtained through example problems.

Toward this goal, our approach is based on the following procedure [15,16], known as the Flowfield-Dependent Mixed Explicit–Implicit (FDMEI) scheme:

(a) Write the Navier–Stokes system of equations in a conservation form.

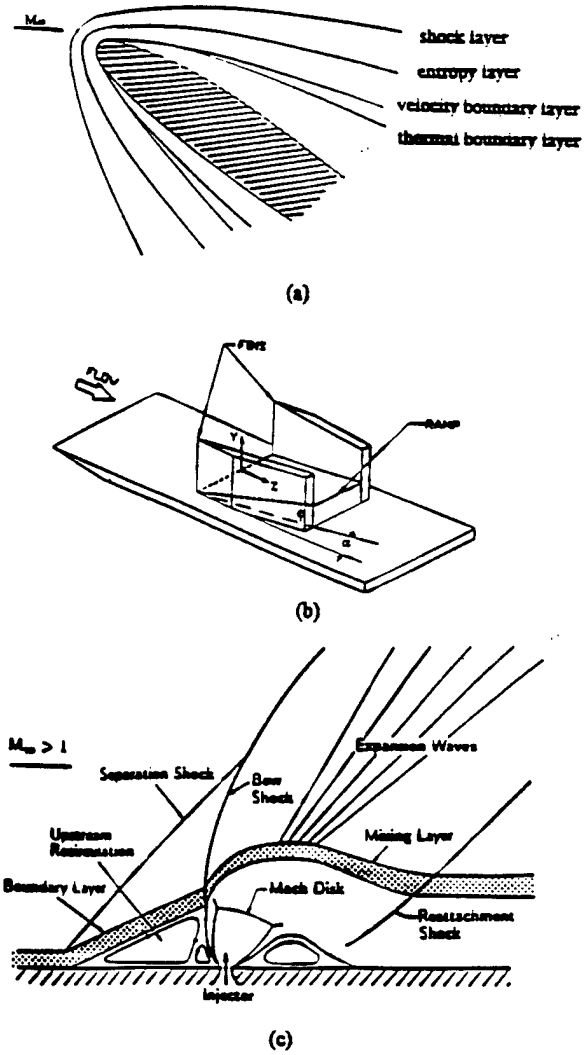

Fig. 1. Supersonic and hypersonic flows: (a) External flow over a blunt body; (b) internal flow through fins; (c) reacting flow (air-breathing combustion).

(b) Expand the conservation variable U^{n+1} in Taylor series up to and including the second-order time derivatives of the conservation variables.

(c) Introduce in step (b) six different flowfield-dependent implicitness parameters which are calculated from the changes in Mach numbers, Reynolds numbers, Peclet numbers, and Damköhler numbers (if reacting) between nodal points or local elements.

(d) Substitute step (a) and (c) into step (b) to obtain the increments of the conservation variables ΔU^{n+1}. As a result, the final form resembles the implicit factored scheme of Beam and Warming [1], but much more rigorous.

(e) Step (d) may be used either in FDM or FEM.

The computational procedure as described above is capable of resolving complex properties of fluid flows in general with shock waves, turbulence, and recting flows in particular.

(1) *Shock waves in compressible flows* are dependent on changes in Mach number between nodal points in FDM and within local elements in FEM. Shock wave discontinuities are characterized by these changes in Mach number.

(2) *Incompressible turbulent flows* are dependent on changes in Reynolds number between nodal points in FDM and within local elements in FEM. Incompressibility conditions are characterized by these changes in Reynolds number.

(3) *Compressible turbulent flows* are dependent on changes in both Mach number and Reynolds number between nodal points in FDM and within local elements in FEM. Dilatational dissipation is characterized by these changes in Mach number and Reynolds number.

(4) *High temperature gradient flows* are dependent on changes in Peclet number between nodal points in FDM and within local elements in FEM. The convection vs. diffusion in heat transfer is characterized by these changes in Peclet number.

(5) *Reaction flows* are dependent on changes in Damköhler number between nodal points in FDM and within local elements in FEM. The mass source vs. convective transfer, mass source vs. diffusive transfer, heat source vs. convective heat transfer, heat source vs. conductive heat transfer, and heat source vs. diffusive heat transfer are characterized by these changes in Damköhler number.

(6) *Direct numerical simulation* (*DNS*) in which mesh refinements are carried out until turbulence length microscales are resolved without turbulence models can not be reliable particularly for high speed compressible turbulent flows unless the computational scheme is capable of treating high gradients of variables as described in (3) above. To improve turbulence calculations, Legendre polynomial spectral modes may be added as shown in [15]. Whether or not the spectral mode approach is advantageous for an overall computational efficiency remains to be seen. Due to the limitation of computer time, the example problems in this paper are not intended for DNS microscale resolutions.

Details of the mathematical formulations as described above are presented in Section 2, implementation and computational process in Section 3, some example problems in Section 4, and concluding remarks in Section 5.

2. Mathematical formulations

For the general purpose program considering the compressible viscous reacting flows, we write the conservation form of the Navier–Stokes system of equations as

$$\frac{\partial \boldsymbol{U}}{\partial t}+\frac{\partial \boldsymbol{F}_i}{\partial x_i}+\frac{\partial \boldsymbol{G}_i}{\partial x_i}=\boldsymbol{B} \tag{1}$$

where $\boldsymbol{U}$, $\boldsymbol{F}_i$, $\boldsymbol{G}_i$ and $\boldsymbol{B}$ denote the conservation flow variables, convection flux variables, diffusion flux variables, and source terms, respectively,

$$\boldsymbol{U}=\begin{bmatrix}\rho\\ \rho v_i\\ \rho E\\ \rho Y_k\end{bmatrix},\quad \boldsymbol{F}_i=\begin{bmatrix}\rho v_i\\ \rho v_i v_j+p\delta_{ij}\\ \rho E v_i+p v_i\\ \rho Y_k v_i\end{bmatrix},\quad \boldsymbol{G}_i=\begin{bmatrix}0\\ -\tau_{ij}\\ -\tau_{ij}v_j-kT_{,i}-\sum \rho c_{pk}TD_{km}Y_{k,i}\\ -\rho D_{km}Y_{k,i}\end{bmatrix},\quad \boldsymbol{B}=\begin{bmatrix}0\\ 0\\ -H_k^0 w_k\\ w_k\end{bmatrix}$$

where $f_i = \sum_{i=1}^{N} Y_i f_{i_i}$ is the chemical species, H_i^0 is the zero-point enthalpy, w_i is the reaction rate, and D_{i_j} is the binary diffusivity. Additional equations for vibrational and electronic energies may be included in (1) for hypersonics.

Expanding the conservation variables U in Taylor series including the first and second derivatives, we have

$$U^{n+1} = U^n + \Delta t \frac{\partial U^{n+s_1}}{\partial t} + \frac{\Delta t^2}{2} \frac{\partial^2 U^{n+s_2}}{\partial t^2} - O(\Delta t^3) \tag{2}$$

where s_1 and s_2 are the implicitness parameters defined such that

$$\frac{\partial U^{n+s_1}}{\partial t} = \frac{\partial U^n}{\partial t} + s_1 \frac{\partial \Delta U^{n+1}}{\partial t} \quad 0 \leq s_1 \leq 1 \tag{3}$$

$$\frac{\partial^2 U^{n+s_2}}{\partial t^2} = \frac{\partial^2 U^n}{\partial t^2} + s_2 \frac{\partial^2 \Delta U^{n+1}}{\partial t} \quad 0 \leq s_2 \leq 1 \tag{4}$$

with $\Delta U^{n+1} = U^{n+1} - U^n$. It is assumed that the convection flux F_i is a function of U and the diffusion flux G_i is a function of both U and its gradient $U_{,i}$. Thus, we have

$$\frac{\partial U}{\partial t} = -\frac{\partial F_i}{\partial x_i} - \frac{\partial G_i}{\partial x_i} + B \tag{5}$$

$$\frac{\partial^2 U}{\partial t^2} = -\frac{\partial}{\partial x_i}\left(a_i \frac{\partial U}{\partial t}\right) - \frac{\partial}{\partial x_i}\left(b_i \frac{\partial U}{\partial t}\right) - \frac{\partial^2}{\partial x_i \partial x_j}\left(c_{ij} \frac{\partial U}{\partial t}\right) + d\left(\frac{\partial U}{\partial t}\right) \tag{6}$$

where the convection Jacobian a_i, the diffusion Jacobian b_i, the diffusion gradient Jacobian c_{ij}, and the source Jacobian d are defined as

$$a_i + \frac{\partial F_i}{\partial U}, \qquad b_i = \frac{\partial G_i}{\partial U}, \qquad c_{ij} = \frac{\partial G_i}{\partial U_{,j}}, \qquad d = \frac{\partial B}{\partial U} \tag{7}$$

Substituting (3)–(6) into (2) and assuming the product of the diffusion gradient Jacobian with third-order spatial derivatives to be negligible, we obtain

$$\begin{aligned}
\Delta U^{n+1} = {} & \Delta t\left[-\frac{\partial F_i^n}{\partial x_i} - \frac{\partial G_i^n}{\partial x_i} + B^n + s_1\left(-\frac{\partial \Delta F_i^{n+1}}{\partial x_i} - \frac{\partial \Delta G_i^{n+1}}{\partial x_i} + \Delta B^{n+1}\right)\right] \\
& + \frac{\Delta t^2}{2}\left\{\left[\frac{\partial}{\partial x_i}(a_i + b_i)\left(\frac{\partial F_j^n}{\partial x_j} - \frac{\partial G_j^n}{\partial x_j} - B^n\right) - d\left(\frac{\partial F^n}{\partial x_i} - \frac{\partial G_i^n}{\partial x_i} - B^n\right)\right]\right. \\
& + s_2\left[\frac{\partial}{\partial x_i}(a_i + b_i)\left(\frac{\partial \Delta F_j^{n+1}}{\partial x_j} + \frac{\partial \Delta G_j^{n+1}}{\partial x_j} - \Delta B^{n+1}\right)\right. \\
& \left.\left. - d\left(\frac{\partial \Delta F_i^{n+1}}{\partial x_i} + \frac{\partial \Delta G_i^{n+1}}{\partial x_i} - \Delta B^{n+1}\right)\right]\right\} + O(\Delta t^3)
\end{aligned} \tag{8}$$

where all Jacobians are considered to be constant within an incremental numerical time step, but allowed to be updated at consecutive time steps.

In order to provide different implicitness (different numerical treatments or schemes) to different physical quantities, we reassign s_1 and s_2 associated with the diffusion and source term, respectively,

$$s_1 \Delta G_i \Rightarrow s_3 \Delta G_i, \qquad s_1 \Delta B \Rightarrow s_5 \Delta B \tag{9a}$$

$$s_2 \Delta G_i \Rightarrow s_4 \Delta G_i, \qquad s_2 \Delta B \Rightarrow s_6 \Delta B \tag{9b}$$

with the various implicitness parameters defined as

s_1 = first-order convection implicitness parameter
s_2 = second-order convection implicitness parameter
s_3 = first-order diffusion implicitness parameter
s_4 = second-order diffusion implicitness parameter
s_5 = first-order source term implicitness parameter
s_6 = second-order source term implicitness parameter

The first order implicitness parameters s_1, s_3 and s_5 will be shown to be flowfield dependent with the solution accuracy assured by taking into account the flowfield gradients, whereas the second order implicitness parameters s_2, s_4 and s_6, which are also flowfield dependent, mainly act as artificial viscosity, contributing to the solution stability.

Substituting these implicitness parameters as defined in (9) into (8), we obtain

$$\Delta U^{n+1} + \Delta t\left[s_1\left(\frac{\partial a_i\,\Delta U^{n+1}}{\partial x_i}\right) + s_3\left(\frac{\partial b_i\,\Delta U^{n+1}}{\partial x_i} + \frac{\partial^2 c_{ij}\,\Delta U^{n+1}}{\partial x_i\,\partial x_j}\right) - s_5 d\,\Delta U^{n+1}\right]$$
$$- \frac{\Delta t^2}{2}\left\{ s_2\left[\frac{\partial^2 (a_i a_j + b_i a_j)\,\Delta U^{n+1}}{\partial x_i\,\partial x_j} - d\,\frac{\partial a_i\,\Delta U^{n+1}}{\partial x_i}\right] + s_4\left[\left(\frac{\partial^2 (a_i b_j + b_i b_j)\,\Delta U^{n+1}}{\partial x_i\,\partial x_j}\right)\right.\right.$$
$$\left.\left. - d\left(\frac{\partial b_i\,\Delta U^{n+1}}{\partial x_i} + \frac{\partial^2 c_{ij}\,\Delta U^{n+1}}{\partial x_i\,\partial x_j}\right)\right] - s_6\left[d\,\frac{\partial (a_i + b_i)\,\Delta U^{n+1}}{\partial x_i} - d\,\Delta U^{n+1}\right]\right\} + \Delta t\left(\frac{\partial F_i^n}{\partial x_i} - \frac{\partial G_i^n}{\partial x_i} - B^n\right)$$
$$- \frac{\Delta t^2}{2}\left[\frac{\partial}{\partial x_i}(a_i + b_i)\left(\frac{\partial F_j^n}{\partial x_j} - \frac{\partial G_j^n}{\partial x_j} - B^n\right) - d\left(\frac{\partial F_i^n}{\partial x_i} - \frac{\partial G_i^n}{\partial x_i} - B^n\right)\right] - \mathrm{O}(\Delta t^3) = 0 \tag{10}$$

with

$$\Delta B^{n+1} = \frac{\partial B}{\partial U}\,\Delta U^{n+1} \quad = d\,\Delta U^{n+1} \tag{11}$$

Rearranging (10), we obtain

$$R = A\,\Delta U^{n+1} + \frac{\partial}{\partial x_i}(E_i\,\Delta U^{n+1}) + \frac{\partial^2}{\partial x_i\,\partial x_j}(E_{ij}\,\Delta U^{n+1}) + Q^n + \mathrm{O}(\Delta t^3), \tag{12}$$

or

$$\left(A - \frac{\partial}{\partial x_i}E_i - \frac{\partial^2}{\partial x_i\,\partial x_j}E_{ij}\right)\Delta U^{n+1} = -Q^n, \tag{13}$$

with

$$A = I + \Delta t\, s_5 d + \frac{\Delta t^2}{2} s_6 d \tag{14}$$

$$E_i = \Delta t(s_1 a_i + s_3 b_i) + \frac{\Delta t^2}{2}\left[s_6 d(a_i + b_i) + s_2\, d a_i + s_4 d b_i\right] \tag{15}$$

$$E_{ij} = \Delta t\, s_3 c_{ij} - \frac{\Delta t^2}{2}\left[s_2(a_i a_j + b_i a_j) + s_4(a_i b_j + b_i b_j - d c_{ij})\right] \tag{16}$$

$$Q^n = \frac{\partial}{\partial x_i}\left[\left(\Delta t + \frac{\Delta t^2}{2} d\right)(F_i^n + G_i^n) + \frac{\Delta t^2}{2}(a_i + b_i)B^n\right]$$
$$- \frac{\partial^2}{\partial x_i\,\partial x_j}\left[\frac{\Delta t^2}{2}(a_i + b_i)(F_j^n + G_j^n)\right] - \left(\Delta t + \frac{\Delta t^2}{2} d\right)B^n. \tag{17}$$

An alternative scheme is to allow the source term in the LHS of (13) to lag from $n+1$ to n so that (13) may be written as

$$\left(I + \frac{\partial}{\partial x} E_i - \frac{\partial^2}{\partial x\, \partial x} E_{ij}\right) \Delta U^{n+1} = -Q^n \tag{18}$$

with

$$Q^n = \frac{\partial}{\partial x_i}\left[\left(\Delta t + \frac{\Delta t^2}{2} d\right)(F_i^n - G_i^n) + \frac{\Delta t^2}{2}(a_i + b_i)B^n\right] - \frac{\partial^2}{\partial x_i\, \partial x_j}\left[\frac{\Delta t^2}{2}(a_i + b_i)(F_j^n - G_j^n)\right] - \left(\Delta t\, s_5 + \frac{\Delta t^2}{2} s_6\right) d\, \Delta U^n - \left(\Delta t + \frac{\Delta t^2}{2} d\right) B^n \tag{19}$$

Note that the Beam–Warming scheme [1] can be written in the form identical to (18) with the following definitions of E_i, E_{ij} and Q^n

$$E_i = m\, \Delta t (a_i + b_i), \quad \text{with } m = \theta/(1+\xi) \tag{20}$$

$$E_{ij} = m\, \Delta t\, c_{ij} \tag{21}$$

$$Q^n = \frac{\Delta t}{1+\xi}\left(\frac{\partial F_i^n}{\partial x_i} + \frac{\partial G_i^n}{\partial x_i}\right) + \frac{\xi}{1+\xi}\Delta U^n \tag{22}$$

where the cross derivative terms appearing in Q^n for the Beam–Warming scheme are included in the second derivative terms on the LHS. The Beam–Warming scheme is seen to be a special case of the FDMEI equations if we set $s_1 = s_3 = m$, $s_2 = s_4 = s_5 = s_6 = 0$, in (18), with adjustments of Q^n on the RHS as in (22). The stability analysis of the Beam–Warming scheme requires $\xi \geq 0.385$ and $\theta = \frac{1}{2} + \xi$. This will fix the implicitness parameter m to be $0.639 \leq m \leq 0.75$. It can be shown that the FDMEI equations as derived in (13) or (18) are capable of producing practically all existing FDM and FEM schemes. Some examples are shown in Appendix A.

Contrary to the Beam–Warming scheme, the FDMEI approach is to obtain the implicitness parameters from the current flowfield variables at each and every nodal point rather than by fixing the implicitness parameters to certain predetermined numbers and using them for the entire flow domain irrespective of the local flowfield variation from one point to another. These implicitness parameters may be determined for spatial and temporal bases as depicted in Fig. 2. The final values of implicitness parameters at any point and at any time can be obtained as the average of both spatial and temporal contributions:

Convection implicitness parameters

$$s_1 = \begin{cases} \min(r, 1) & r > \alpha \\ 0 & r < \alpha,\ \mathrm{M}_{\min} \neq 0 \\ 1 & \mathrm{M}_{\min} = 0 \end{cases} \qquad s_2 = s_1^n, \quad 0 < n < 1 \tag{23}$$

with

$$r = \sqrt{\mathrm{M}_{\max}^2 - \mathrm{M}_{\min}^2}/\mathrm{M}_{\min} \tag{24}$$

where the maximum and minimum Mach numbers are calculated between adjacent nodal points in FDM or within a local finite element in FEM for spatial implicitness parameters (Fig. 2(a)) and between the time step at n and $n-1$ for temporal implicitness parameters (Fig. 2(b)), and α is a user-specified small number $\alpha \cong 0.01$). Here, it is seen that s_1 is directly related to the flowfield, whereas s_2 depends on s_1 such that $s_2 = s_1^n$. The primary role of s_1 is to ensure the solution accuracy by properly accommodating the convection gradients, whereas that of s_2 is to act as artificial viscosity, for solution stability.

Diffusion implicitness parameters

$$s_3 = \begin{cases} \min(s, 1) & s > \beta \\ 0 & s < \beta,\ \mathrm{Re}_{\min} \neq 0, \text{ or } \mathrm{Pe}_{\min} \neq 0 \\ 1 & \mathrm{Re}_{\min} = 0, \text{ or } \mathrm{Pe}_{\min} = 0 \end{cases} \qquad s_4 = s_3^n, \quad 0 < n < 1 \tag{25}$$

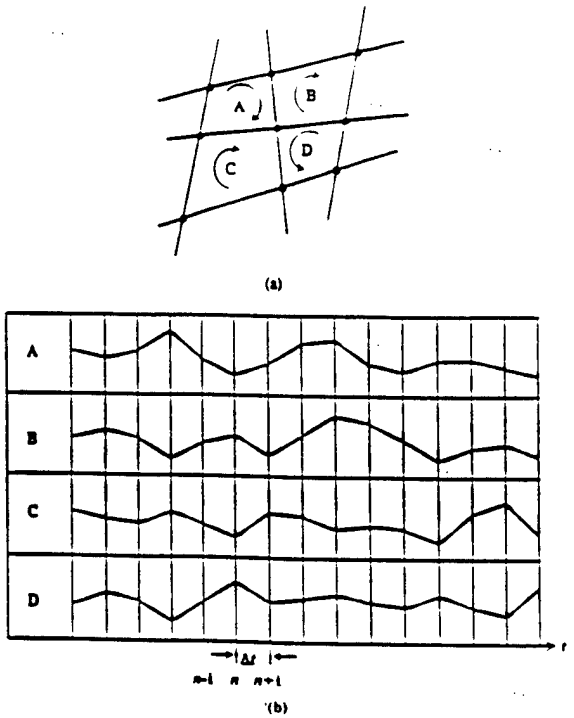

Fig. 2. Spatial and temporal flowfield dependent implicitness parameters: (a) idealized turbulence length scales assumed to be within each element-spatially evolving turbulence. The maximum and minimum value of M, Re, Pe and Da are those among the corner nodes within an element; (b) idealized turbulence time scales assumed to be within each time step-temporally evolving turbulence. The maximum and minimum value of M, Re, Pe and Da are identified at time steps n and $n-1$.

with

$$s = \sqrt{\mathrm{Re}_{\max}^2 - \mathrm{Re}_{\min}^2}/\mathrm{Re}_{\min} \quad \text{or} \quad s = \sqrt{\mathrm{Pe}_{\max}^2 - \mathrm{Pe}_{\min}^2}/\mathrm{Pe}_{\min} \tag{26a,b}$$

where the maximum and minimum Reynolds numbers or maximum and minimum Peclet numbers are calculated similarily as in s_1 for spatial and temporal implicitness parameters, and β is a user-specified small number ($\beta \cong 0.01$). If temperature gradients are large, it is possible that Peclet numbers instead of Reynolds numbers will dictate the diffusion implicitness parameters. The larger value of s_1 is to be chosen, as obtained either from (26a) or (26b). Note also that $s_4 = s_3''$ with s_3 ensuring the solution accuracy by taking into account the diffusion gradients, and here again, s_4 plays the role of artificial viscosity, for solution stability.

Source term implicitness parameters

For the case of chemically reacting flows the Da (Damköhler number) must be used

$$s_5 = \begin{cases} \min(t, 1) & t \geq \gamma \\ 0 & t < \gamma,\ \mathrm{Da}_{\min} \neq 0 \\ 1 & \mathrm{Da}_{\min} = 0 \end{cases} \qquad s_6 = s_5'', \quad 0 < n < 1 \tag{27}$$

with

$$t = \sqrt{\mathrm{Da}_{\max}^2 - \mathrm{Da}_{\min}^2}/\mathrm{Da}_{\min} \tag{28}$$

where the maximum and minimum Damköhler numbers are calculated similarly as in s_1 and s_3 for spatial and temporal implicitness parameters, and γ is a user-specified small number ($\gamma \cong 0.01$). The relationship between s_5 and s_6 is similar to those for convection and diffusion implicitness parameters such that $s_6 = s_5''$ with s_5 and s_6 controlling the solution accuracy and solution stability, respectively. The average of both spatial and temporal implicitness parameters will be adopted for use in computations at any point (element) and time.

Relationships between all physical phenomena and the corresponding numerical treatments are characterized by the balance between the first-order implicitness parameters (s_1, s_3, s_5) and the second-order implicitness parameters (s_2, s_4, s_6), ensuring the computational accuracy and computational stability, respectively. The idea is to provide adequate (no more and no less than required) amount of numerical viscosity in order to preserve the computational accuracy. Note that the definitions for the second-order implicitness parameters have been modified from those reported in [15,16] in order to meet the above requirements (Fig. 3). Initially, it was thought that the second-order implicitness parameters should be the direct opposite compliances of the first-order implicitness parameters $(s_2 = 1 - s_1, s_4 = 1 - s_3, s_6 = 1 - s_5)$ [16] such that the second-order implicitness parameters are the maximum and minimum, respectively, for the minimum and maximum values of the first-order implicitness parameters. Unfortunately, such definition resulted in too little numerical viscosities for the high values of the first-order implicitness parameters. Subsequently, the limiting values (0.5) of the second-order implicitness parameters were provided such that $s_2 = \max(1 - s_1, 0.5)$, etc. as experimented in [15]. However, it was noted that both first- and second-order parameters should assume the same values at the both extremes at zero and unity with the second-order implicitness parameters being reasonably large for all values of the first-order implicitness parameters. Thus, the second-order implicitness parameters given above are the nonlinear continuous functions of the first-order implicitness parameters satisfying these requirements. The range of the constant n is $0 < n < 1$, although $n \cong \frac{1}{4}$ has been found to be the optimum, exhibiting the best convergence rate for reasonably high CFL numbers in the example problems presented in Section 4.

The flowfield dependent implicitness parameters as defined above are capable of allowing various numerical schemes to be automatically generated, as summarized below:

(1) The first-order implicitness parameters s_1 and s_3 control all high gradient phenomena such as shock waves and turbulence. These parameters as calculated from the changes of local Mach numbers and Reynolds (or Peclet) numbers within each element and are indicative of the actual local element flowfields. The contours of these parameters closely resemble the flowfields themselves, with both s_1 and s_3 being large (close to unity) in regions of high gradients, but small (close to zero) in regions where the gradients are small. The basic role of s_1 and s_3 is to provide computational accuracy.

(2) The second-order implicitness parameters s_2 and s_4 are also flowfield dependent. However, their primary role is to provide adequate computational stability (artificial viscosity) as they were originally introduced

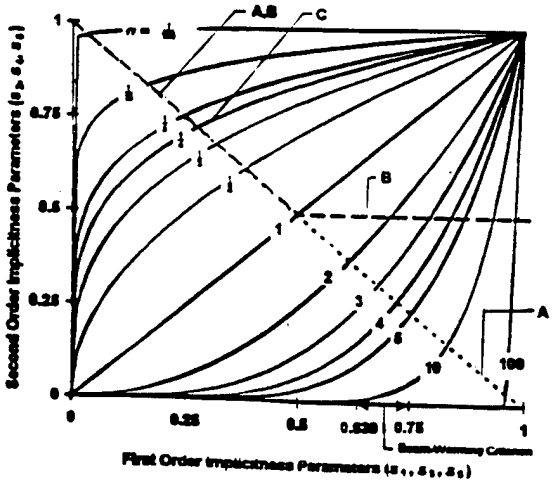

A. $s_2 = 1 - s_1, s_4 = 1 - s_3, s_6 = 1 - s_5$

B. $s_2 = \max(1 - s_1, 0.5), s_4 = \max(1 - s_3, 0.5), s_6 = \max(1 - s_5, 0.5)$

C. $s_2 = s_1^n, s_4 = s_3^n, s_6 = s_5^n, 0 < n < 1$

Fig. 3. Relationships between the first- and second-order implicitness parameters. Stable solutions occur in the range, $0 < n < 1$, with an optimum at $n \approx \frac{1}{4}$ for the second-order implicitness parameters to preserve the solution accuracy as dictated by the first-order implicitness parameters.

into the second-order time derivative term of the Taylor series expansion of the conservation flow variables U^{n+1}. The primary role of s_2 and s_4 is to provide computational stability.

(3) The s_3 terms represent convection. This implies that if $s_3 \cong 0$ then the effect of convection is small. The computational scheme is automatically altered to take this effect into account, with the governing equations being predominantly parabolic-elliptic. Note that these effects are confined at U^{n+1}, not at U^n.

(4) The s_4 terms are associated with diffusion. Thus, with $s_4 \cong 0$, the effect of viscosity or diffusion is small and the computational scheme is automatically switched to that of Euler equations where the governing equations are predominantly hyperbolic.

(5) If the first-order implicitness parameters s_1 and s_2 are nonzero, this indicates a typical situation for the mixed hyperbolic, parabolic and elliptic nature of the Navier–Stokes system of equations, with convection and diffusion being equally important. This is the case for incompressible flows at low speeds. The unique property of the FDMEI scheme is its capability to control pressure oscillations adequately without resorting to the separate hyperbolic elliptic pressure equation for pressure corrections. The capability of FDMEI scheme to handle incompressible flows is achieved by a delicate balance between s_1 and s_3 as determined by the local Mach numbers and Reynolds (or Peclet) numbers. If the flow is completely incompressible (M = 0), the criteria given by (23) leads to $s_1 = 1$, whereas the implicitness parameter s_3 is to be determined according to the criteria given in (25). Make a note of the presence of the convection–diffusion interaction terms given by the product of $\boldsymbol{b}_i \boldsymbol{a}_j$ in the s_2 terms and $\boldsymbol{a}_i \boldsymbol{b}_j$ in the s_4 terms. These terms allow interactions between convection and diffusion in the viscous incompressible and/or viscous compressible flows.

(6) If temperature gradients rather than velocity gradients dominate the flowfield, then s_3 is governed by the Peclet number rather than by the Reynolds number. Such cases arise in high speed, high temperature compressible flows close to the wall.

(7) In the case of reacting flows the source terms $\boldsymbol{B}$ contain the reaction rates which are functions of the flowfield variables. With widely disparate time and length scales involved in the fast and slow chemical reaction rates of various chemical species as characterized by Damköhler numbers, the first-order source term implicitness parameter s_5 is instrumental in dealing with the stiffness of the resulting equations to obtain convergence to accurate solutions. On the other hand, the second-order source term implicitness parameter s_6 contribute to the stability of solutions. It is seen that the criteria given by (27) will adjust the reaction rate terms in accordance with the ratio of the diffusion time to the reaction time in finite rate chemistry so as to assure the accurate solutions with computational stability.

(8) Various definitions of Peclet number and Damköhler numbers (Table 1) between the energy and species equations should be checked. Whichever definition provides larger values of s_3 and s_6 must be used. The summary of the above definitions for implicitness parameters is shown in Table 2.

(9) The transition to turbulence is a natural flow process as the Reynolds number increases, causing the gradients of any or all flow variables to increase. This phenomenon is the physical instability and is detected by the increase of s_3 if the flow is incompressible, but by both s_3 and s_1 if the flow is compressible. Such physical instability is likely to trigger the numerical instability, but will be countered by the second-order implicitness parameters s_2 and/or s_4 to ensure numerical stability automatically. In this process, these flowfield dependent implicitness parameters are capable of capturing relaminarization, compressibility effect or dilatational turbulent energy dissipation, and turbulent unsteady fluctuations.

(10) An important contribution of the first-order implicitness parameters is the fact that they can be used as error indicators for adaptive mesh generations. That is, the larger the implicitness parameters the higher the gradients of any flow variables. Whichever governs (largest first-order implicitness parameters) will indicate the need for mesh refinements. In this case, all variables (density, velocity, pressure, temperature, species mass fraction) participate in resolving the adaptive mesh, contrary to the conventional definitions of the error indicators.

(11) Physically, the implicitness parameters will influence the magnitudes of Jacobians. Thus, Item 8 above may be modified so that the diffusion implicitness parameters s_3 and s_4 as calculated from Reynolds number and Peclet number can be applied to the Jacobians $(\boldsymbol{a}_i, \boldsymbol{b}_i, c_{ij})$, corresponding to the momentum equations and energy equation, respectively. Furthermore, two different definitions of Peclet number (Pe_I, Pe_{II}) would require the s_3 and s_4 as calculated from the energy and species equations to be applied to the corresponding terms of the Jacobians. Similar applications for the source term implicitness

Table 1
Definitions of nondimensional flowfield quantities

$$\underbrace{\rho(\boldsymbol{v}\cdot\nabla)\boldsymbol{v}}_{\mathrm{A}} = \underbrace{-\nabla p}_{\mathrm{B}} - \underbrace{\mu\left[\nabla^2\boldsymbol{v} + \frac{1}{3}\nabla(\nabla\cdot\boldsymbol{v})\right]}_{\mathrm{C}}$$

$$\underbrace{\nabla\cdot\rho\boldsymbol{v}\int_{T_{\mathrm{ref}}}^{T} c_{v_i}\,\mathrm{d}T}_{\mathrm{E}} - \underbrace{\nabla\cdot\rho D\,\nabla Y_i\int_{T_{\mathrm{ref}}}^{T} c_{p_i}\,\mathrm{d}T}_{\mathrm{F}} - \underbrace{\nabla\cdot k\,\nabla T}_{\mathrm{G}} = \underbrace{-\sum_{i=1}^{N} H_i w_i}_{\mathrm{N}}$$

$$\underbrace{\nabla\cdot(\rho Y_i\boldsymbol{v})}_{\mathrm{I}} - \underbrace{\nabla\cdot(\rho D\,\nabla Y_i)}_{\mathrm{J}} = \underbrace{w_i}_{\mathrm{K}}$$

Mach number	M	$\frac{u}{a}$	$\frac{\mathrm{A}}{\mathrm{B}} = \frac{\text{inertial force}}{\text{pressure force}}$
Reynolds number	Re	$\frac{\rho u L}{\mu}$	$\frac{\mathrm{A}}{\mathrm{C}} = \frac{\text{initial force}}{\text{viscous force}}$
Peclet number, I	Pe_{I}	$\frac{\rho u L c_{v_i}}{k}$	$\frac{\mathrm{E}}{\mathrm{G}} = \frac{\text{convective heat transfer}}{\text{conductive heat transfer}}$
Peclet number, II	$\mathrm{Pe}_{\mathrm{II}}$	$\frac{uL}{D}$	$\frac{\mathrm{I}}{\mathrm{J}} = \frac{\text{convective mass transfer}}{\text{diffusive mass transfer}}$
Damkohler number, I	Da_{I}	$\frac{Lw_i}{\rho u Y_i}$	$\frac{\mathrm{K}}{\mathrm{I}} = \frac{\text{mass source}}{\text{convective transfer}}$
Damkohler number, II	$\mathrm{Da}_{\mathrm{II}}$	$\frac{L^2 w_i}{\rho D Y_i}$	$\frac{\mathrm{K}}{\mathrm{J}} = \frac{\text{mass source}}{\text{diffusive transfer}}$
Damkohler number, III	$\mathrm{Da}_{\mathrm{III}}$	$\frac{qL}{Hu}$	$\frac{\mathrm{N}}{\mathrm{E}} = \frac{\text{heat source}}{\text{convective heat transfer}}$
Damkohler number, IV	$\mathrm{Da}_{\mathrm{IV}}$	$\frac{qL^2}{kT}$	$\frac{\mathrm{N}}{\mathrm{G}} = \frac{\text{heat source}}{\text{conductive heat transfer}}$
Damkohler number, V	Da_{V}	$\frac{qL^2}{HD}$	$\frac{\mathrm{N}}{\mathrm{F}} = \frac{\text{heat source}}{\text{diffusive heat transfer}}$

parameters s_5 and s_6 should be followed for the source term Jacobian d. In this way, high temperature gradients arising from the momentum and energy equations and the finite rate chemistry governed by the energy and species equations can be resolved accordingly.

The FDMEI equations as given in (13) or (18) may be solved by either FDM or FEM. The standard linear Galerkin approximations of FEM lead to the results of central differences of FDM. However, the main difference between FDM and FEM arises when integration by parts is performed in FEM and the explicit terms of Neumann boundary conditions 'naturally' appear as boundary integral forms. Thus, all Neumann boundary conditions can be directly specified at boundaries in FEM. This is not the case for FDM. Often, a rather cumbersome process must be taken for Neumann boundary conditions in FDM.

When dealing with all speed flow regimes such as in shock wave turbulent boundary layer interactions where compressible and incompressible flows, viscous and inviscid flows, and laminar and turbulent flows are intermingled throughout the flowfield domain, a computational scheme intended for only one type of flow physics and that does not account for other types of flow phenomena will fail. For example, the flow close to the wall in shock wave turbulent boundary layer interactions is incompressible ($\mathrm{M} \leq 0.1$), whereas away from the wall the flow is compressible (supersonic or hypersonic). In this case, viscous flows change to inviscid flows. In between these two extremes the flowfield changes continuously, oscillating back and forth across the boundary layers of velocity and entropy, and leading edge and bow shocks. At any given computational nodal point or element, gradients of each variable (density, pressure, velocity and temperature) may be very small or very large, so large that practically all currently available computational methods may fail. In order to succeed, it is necessary that the current flow physics everywhere be identified and so recognized, with specific computational schemes accorded to each and every computational nodal point and element. It is clear that such accommodations are available in (13) or (18).

Table 2
Flowfield dependent implicitness parameters

Convection gradient behavior	
s_1—*First-order convection implicitness parameter*	
$s_1 = \begin{cases} \min(r, 1) & r > \alpha \\ 0 & r < \alpha, M_{min} \neq 0 \\ 1 & M_{min} = 0 \end{cases}$ $r = \sqrt{M_{max}^2 - M_{min}^2}/M_{min}$	*Ensures solution accuracy* Strongly flowfield dependent, with high gradients characterized by large Mach number changes between nodal points or within element and between time steps
s_2—*Second-order convection implicitness parameter*	
$s_2 = s_1^n, \quad 0 < n < 1$	*Ensures solution stability* Flowfield dependent artificial viscosity for convection process
Diffusion gradient behavior.	
s_3—*First-order diffusion implicitness parameter*	
$s_3 = \begin{cases} \min(s, 1) & s > \beta \\ 0 & s < \beta, Re_{min} \neq 0, \text{ or } Pe_{min} \neq 0 \\ 1 & Re_{min} = 0 \text{ or } Pe_{min} = 0 \end{cases}$ $s = \sqrt{Re_{max}^2 - Re_{min}^2}/Re_{min}$ or $s = \sqrt{Pe_{max}^2 - Pe_{min}^2}/Pe_{min}$	*Ensures solution accuracy* Strongly flowfield dependent, with high gradients characterized by large changes in Reynolds number or Peclet number between nodal points or within element and between time steps. Diffusion gradient behavior may be dictated by Peclet number when temperature gradients are high. Choose whichever (Reynolds or Peclet number) provides the larger value for s_3
s_4—*Second-order diffusion implicitness parameter*	
$s_4 = s_3^n, \quad 0 < n < 1$	*Ensures solution stability* Flowfield dependent artificial viscosity for diffusion process
Source term gradient behavior	
s_5—*First-order source term implicitness parameter*	
$s_5 = \begin{cases} \min(r, 1) & r \geq \alpha \\ 0 & r < \alpha, Da_{min} \neq 0 \\ 1 & Da_{min} = 0 \end{cases}$ $r = \sqrt{Da_{max}^2 - Da_{min}^2}/Da_{min}$	*Ensures solution accuracy* Strongly flowfield dependent, with high reaction rate gradients characterized by large Damköhler number changes between nodal points or within element and between time steps
s_6—*Second-order source term implicitness parameter*	
$s_6 = s_5^n, \quad 0 < n < 1$	*Ensures solution stability* Flowfield dependent artificial viscosity for reaction process

3. Implementation and computational process

As stated earlier, the governing equations for the Taylor series-modified Navier–Stokes system of equations, (13), may be applied to either FDM or FEM, or to the finite volume method (FVM). For FDM applications the first-order and second-order spatial derivatives may be written in central difference schemes. For example, we

may write for any variable u as

$$\left.\frac{\partial u}{\partial x}\right|_{i,j} = \frac{u_{i+1,j} - u_{i-1,j}}{2\Delta x} \tag{29}$$

$$\left.\frac{\partial^2 u}{\partial x^2}\right|_{i,j} = \frac{u_{i+1,j} - 2u_{i,j} + u_{i-1,j}}{\Delta x^2} \tag{30}$$

with analogous formulas for the y derivatives in two dimensions or corresponding extensions to three-dimensional problems. Any other difference schemes of higher-order accuracy may also be chosen as deemed necessary.

For applications to FEM we begin by expressing the conservation and flux variables and source terms as a linear combination of trial functions Φ_α with the nodal values of these variables.

$$\begin{aligned} \boldsymbol{U}(\boldsymbol{x}, t) &= \Phi_\alpha(\boldsymbol{x}) U_\alpha(t), \qquad \boldsymbol{F}_i(\boldsymbol{x}, t) = \Phi_\alpha(\boldsymbol{x}) F_{\alpha i}(t) \\ \boldsymbol{G}_i(\boldsymbol{x}, t) &= \Phi_\alpha(\boldsymbol{x}) G_{\alpha i}(t), \qquad \boldsymbol{B}(\boldsymbol{x}, t) = \Phi_\alpha(\boldsymbol{x}) B_\alpha(t) \end{aligned} \tag{31}$$

Applying the generalized Galerkin approximations to (12) we obtain

$$\int_\Omega \Phi_\alpha \boldsymbol{R}(\boldsymbol{U}, \boldsymbol{F}_i, \boldsymbol{G}_i, \boldsymbol{B})\, \mathrm{d}\Omega = 0 \tag{32}$$

or

$$(A_{\alpha\beta}\eta_{rs} + B_{\alpha\beta rs})\, \Delta U^{n+1}_{\beta s} = H^n_{\alpha r} + N^n_{\alpha r} \tag{33}$$

where

$$A_{\alpha\beta} = \int_\Omega \Phi_\alpha \Phi_\beta \, \mathrm{d}\Omega, \qquad \eta_{rs} = \delta_{rs} - \left(\Delta t\, s_5 + \frac{\Delta t^2}{2} s_6\right) d_{rs} \tag{34}$$

$$\begin{aligned} B_{\alpha\beta rs} = \int_\Omega \Bigg[& -\left\{\Delta t(s_1 a_{irs} + s_3 b_{irs}) + \frac{\Delta t^2}{2}[s_2 d_{rl} a_{its} + s_6 d_{rl}(a_{its} + b_{its}) + s_4 d_{rl} b_{its}]\right\}\Phi_{\alpha,i}\Phi_\beta \\ & -\left\{\Delta t\, s_3 c_{ijrs} - \frac{\Delta t^2}{2}[s_2(a_{irl}a_{jts} + b_{irl}a_{jts}) + s_4(a_{irl}b_{jts} + b_{irl}b_{jts} - d_{rl}c_{ijts})]\right\}\Phi_{\alpha,i}\Phi_{\beta,j}\Bigg]\mathrm{d}\Omega \\ & + \int_\Gamma \Bigg[\left\{\Delta t(s_1 a_{irs} + s_3 b_{irs}) + \frac{\Delta t^2}{2}[s_2 d_{rl} a_{its} + s_6 d_{rl}(a_{its} + b_{its}) + s_4 d_{rl} b_{its}]\right\}\overset{*}{\Phi}_\alpha \overset{*}{\Phi}_\beta \\ & + \left\{\Delta t\, s_3 c_{ijrs} - \frac{\Delta t^2}{2}[s_2(a_{irl}a_{jts} + b_{irl}a_{jts}) + s_4(a_{irl}b_{jts} + b_{irl}b_{jts} - d_{rl}c_{ijts})]\right\}\overset{*}{\Phi}_\alpha \overset{*}{\Phi}_{\beta,j}\Bigg] n_i \, \mathrm{d}\Gamma \end{aligned} \tag{35}$$

$$\begin{aligned} H^n_{\alpha r} = \int_\Omega \Bigg\{ & \left[\Delta t(F^n_{\beta ir} + G^n_{\beta ir}) + \frac{\Delta t^2}{2} d_{rs}(F^n_{\beta is} + G^n_{\beta is}) + \frac{\Delta t}{2}(a_{irs} + b_{irs}) B^n_{\beta s}\right]\Phi_{\alpha,i}\Phi_\beta \\ & - \frac{\Delta t^2}{2}(a_{irs} + b_{irs})(F^n_{\beta js} + G^n_{\beta js})\Phi_{\alpha,i}\Phi_{\beta,j} + \left[\Delta t\, B^n_{\beta r} + \frac{\Delta t^2}{2} d_{rs} B^n_{\beta s}\right]\Phi_\alpha \Phi_\beta\Bigg\}\mathrm{d}\Omega \end{aligned} \tag{36}$$

$$\begin{aligned} N^n_{\alpha r} = \int_\Gamma \Bigg\{ & \left[-\Delta t(F^n_{\beta ir} + G^n_{\beta ir}) - \frac{\Delta t^2}{2} d_{rs}(F^n_{\beta is} + G^n_{\beta is}) - \frac{\Delta t^2}{2}(a_{irs} + b_{irs}) B^n_{\beta s}\right]\overset{*}{\Phi}_\alpha \overset{*}{\Phi}_\beta \\ & + \frac{\Delta t^2}{2}(a_{irs} + b_{irs})(F^n_{\beta js} + G^n_{\beta js})\overset{*}{\Phi}_\alpha \overset{*}{\Phi}_{\beta,j}\Bigg\} n_i \, \mathrm{d}\Gamma \end{aligned} \tag{37}$$

where $\overset{*}{\Phi}_\alpha$ represents the Neumann boundary trial and test functions, with α, β denoting the global node number and r, s providing the number of conservation variables at each node. For three dimensions, $i, j = 1, 2, 3$ associated with the Jacobians imply directional identification of each Jacobian matrix ($\boldsymbol{a}_1, \boldsymbol{a}_2, \boldsymbol{a}_3, \boldsymbol{b}_1, \boldsymbol{b}_2, \boldsymbol{b}_3, \boldsymbol{c}_{11},$

c_{12}, c_{13}, c_{21}, c_{22}, c_{23}, c_{31}, c_{32}, c_{33}) with $r, s = 1, 2, 3, 4, 5$ denoting entries of each of the 5×5 Jacobian matrices. These indices can be reduced similarly for 2-D. Note also that the relation (18) may be used to move the delta source terms to the RHS of (33) by lagging the source terms one time step behind. The FEM equations given by (33) are referred to as FDMEI-FEM. The counterpart of (33) based on FDM schemes of (29) and (30) is to be called FDMEI-FDM.

It is important to realize that the integration by parts as applied to the generalized Galerkin approximations in FEM produces all Neumann boundary integrals. It is particularly advantageous that Neumann boundary conditions through re-evaluation of Jacobians normal to the boundary surfaces can simply be added to the boundary nodes for the stiffness matrix $B_{\alpha\beta rs}$ in (35). On the other hand, all Neumann boundary conditions which appear in (37) act as source terms. These features are absent in FDM, but implementations of Neumann boundary conditions can be handled by devising special forms of finite differences at boundary nodes.

Similar results are obtained either by FDM or FEM with accuracy of computations derived primarily from the FDMEI equations of (12). However, with the increase of Reynolds number (say around $\mathrm{Re} \gg 10^8$), it is possible that accuracy may increase with applications of special functions such as Legendre polynomials of high degree modes characterizing extremely small turbulent microscales. Implementation of such high frequency modes can be achieved by placing these modes between the corner nodes of isoparametric finite elements. Adaptively, such high modes can be chosen as needed for the resolution of turbulent microscales. Once again, the diffusion implicitness parameter s_1 will play a crucial factor in determining the required degrees of Legendre polynomial. The use of Legendre polynomial spectral modes superimposed onto isoparametric elements has been discussed in [15]. Its merit, however, has not yet been fully established for general applications.

For turbulent flows with an extremely high Reynolds number, the phase error of the short wavelengths can be very large. In this case, it is necessary to add numerical dissipation terms to damp out the short wavelengths. Such numerical viscosities are conceptually different from the second-order implicitness parameters whose role is to ensure stable solutions while preserving the solution accuracy dictated by the first-order implicitness parameters. Toward this end, it is desirable to revise (18) in the form

$$\left(\boldsymbol{I} + \boldsymbol{E}_i \frac{\partial}{\partial x_i} + \boldsymbol{E}_{ij} \frac{\partial^2}{\partial x_i \, \partial x_j}\right) \Delta \boldsymbol{U}''^{\tau+1} = -\boldsymbol{Q}'' - \overline{\boldsymbol{Q}}'' \tag{38}$$

where $\overline{\boldsymbol{Q}}''$ is the numerical dissipation vector in terms of the second-order tensor of numerical dissipation, S_{ij}, associated with the second-order derivatives of $\boldsymbol{U}''$,

$$\overline{\boldsymbol{Q}}'' = S_{ij} \frac{\partial^2 \boldsymbol{U}''}{\partial x_i \, \partial x_j} = \overline{\mu} \, \Delta x_i \, \Delta x_j \frac{\partial^2 \boldsymbol{U}''}{\partial x_i \, \partial x_j} \tag{39}$$

with $\overline{\mu}$ being the numerical dissipation constant chosen as $0 \leq \overline{\mu} \leq \overline{\mu}_0$, where $\overline{\mu}_0$ is set approximately equal to 2, but adjusted from numerical experiments. Note that the Galerkin integral of (39) (integration by parts once) leads to the first derivative of the trial and test functions combined with the nodal values of $\boldsymbol{U}''_\beta$. In addition, note that the damping provided by the second-order derivatives with not disrupt the formal accuracy of the FDMEI scheme. This process may be applied to (13) as well.

One of the most significant aspects of the FDMEI scheme is that for low Mach numbers (incompressible flow) the scheme will automatically adjust itself to prevent pressure oscillations. This adjustment is analogous to the pressure correction scheme employed for incompressible flows. Otherwise, the FDMEI scheme is capable of shock wave resolutions at high Mach numbers, and particularly well suited for dealing with interactions between shock waves and turbulent boundary layers where regions of high and low Mach numbers and Reynolds numbers coexist. In this case, the inviscid and viscous interactions are allowed to take place. To this end the second-order implicitness parameters play the role of artificial viscosity needed for shock wave resolutions in the presence of flow diffusion due to physical viscosity.

In order to understand how the FDMEI scheme handles computations involving both compressible and incompressible flows, fundamental definitions of pressure must be recognized. Consider in the following that the fluid is a perfect gas and that the total energy is given by

$$E = c_v T - \frac{p}{\rho} + \frac{1}{2} v_i v_i \tag{40}$$

The momentum equation for steady state incompressible rotational flow may be integrated to give

$$\int \left(p + \frac{1}{2} \rho v_j v_j \right)_{,i} \mathrm{d}x = \int \left[\mu \left(v_{i,jj} + \frac{1}{3} v_{j,ji} \right) + \rho \varepsilon_{ijk} v_j \omega_k \right] \mathrm{d}x$$

$$p + \frac{1}{2} \rho v_j v_j = p_0 + W \tag{41}$$

with

$$W = \frac{1}{m} \int \left[\mu \left(v_{i,jj} + \frac{1}{3} v_{j,ji} \right) + \rho \varepsilon_{ijk} v_j \omega_k \right] \mathrm{d}x_i$$

where ω_k is the component of a vorticity vector, p_0 is the constant of integration, and m denotes the spatial dimension.

Combining (40) and (41) leads to the following relationship:

$$p_0 = \rho (c_p T + v_i v_i - E) - W \tag{42}$$

If p_0 as given by (42) remains a constant, equivalent to a stagnation pressure, then the compressible flow as assumed in the conservation form of the Navier–Stokes system of equations has now been turned into an incompressible flow, which is expected to occur when the flow velocity is sufficiently reduced (approximately $0.1 \leq M < 0.3$ for air). Thus, (42) may serve as an equivalent equation of state for an incompressible flow. This can be identified element by element for the entire domain. Note that conservation of mass is achieved for incompressible flows with p_0 in (42) being constant, thus keeping the pressure from oscillating.

Once the Navier–Stokes solution via FDMEI is carried out and all flow variables determined, then we compute fluctuations f' of any variable f,

$$f' = f - \bar{f} \tag{43}$$

where f and $\bar{f}$ denote the Navier–Stokes solution and its time average, respectively. This process may be replaced by the fast fourier transform of the Navier–Stokes solution. Unsteady turbulence statistics (turbulent kinetic energy, Reynolds stresses, and various energy spectra) can be calculated once the fluctuation quantities of all variables are determined.

Let us summarize why the FDMEI scheme is capable of handling low speed and high speed and nonreacting and reacting compressible and incompressible flows, including shock waves and turbulent flows: (1) How is the transition from incompressible flow to compressible flow naturally and automatically accommodated without using two separate equations or two separate codes? This process is dictated by the first-order convection implicitness parameter $s1$ as reflected by the Mach number changes and the expression of the stagnation pressure. (2) How is the shock wave captured? As the Mach number increases and its discontinuity is abrupt, the $s2$ terms associated with second order derivatives together with squares of the convection Jacobian provide adequate numerical viscosities through second order derivatives, similarly as the Lax–Wendroff scheme. (3) How is the transition from laminar to turbulent flows naturally and automatically accommodated? This process is governed by the first- and second-order diffusion implicitness parameters ($s3$ and $s4$) as calculated from the changes of the Reynolds number. The terms associated with $s3$ and $s4$ are responsible for fluctuations of velocities, with the values of these implicitness parameters increasing with intensities of turbulence in conjuction with the diffusion gradient Jacobian and the squares of the diffusion Jacobian. This process allows the Navier–Stokes solutions to contain fluctuations which can be extracted by subtracting the time averages of the Navier–Stakes solutions. (4) How do the interactions between convection and diffusion take place? Changes of Mach numbers and Reynolds numbers as reflected by both convection and diffusion implicitness parameters close to the wall contribute to the unsteadiness. Away from the wall, they contribute to the transition between incompressible to compressible flows. (5) How are the stiff equations arising from widely disparate reaction rates of all chemical species treated? The most crucial aspect of the FDMEI scheme is its capability to identify

the ratio of the resident time to the reaction time as calculated from five different definitions of the Damkohler numbers between the adjacent nodal points and time steps as reflected in the calculated first-order implicitness parameter, s_1, and the second-order implicitness parameter, s_2. These parameters provide precise degree of computational implicitness at every nodal point and every time step, contributing to the determination of accurate chemical reactions.

4. Applications

We examine here various example problems: (a) flow over a flat plate, (b) shock wave turbulent boundary layer interactions on a compression corner, (c) 3D duct flows, and (d) lid-driven cavity flow. Linear isoparameteric finite elements are used for the example problems.

(a) *Behavior of flowfield dependent implicitness parameters on flat plate*

First of all, our concern is to test the behaviour of FDMEI and FDMEI-FEM. Toward this objective we examine the flow over a flat plate investigated earlier by Carter [17] as shown in Fig. 4(a). The initial setting for the implicitness parameters are determined from the initial conditions of the flowfield and subsequently updated after each time step until the steady state solution is reached.

Corresponding to the mesh refinements and the flowfields at steady state shown in Fig. 4(b–d), the contours of implicitness parameters s_1 and s_3 are given in Fig. 5. It is seen that the implicitness parameters themselves closely resemble the flowfield. There are little or no changes in Mach numbers and Reynolds numbers between adjacent nodes or elements far away from the surface of the plate as indicated by $s_1 = s_3 = 0$. Along the leading edge shock and boundary layers, both s_1 and s_3 move toward unity indicating that gradients of all variables increase. The final flowfields, as shown in Fig. 4(b–d), are the consequence of these implicitness parameters. The implicitness parameters s_2 and s_4 are the compliances of s_1 and s_3, respectively, with their primary roles being the artificial viscosity. Thus, the first-order implicitness parameters (s_1, s_3) help to resolve the high gradients ensuring the accuracy of the solution. While on the other hand, the second-order implicitness parameters (s_2, s_4) ensure computational stability.

Computations of wall pressure, wall skin friction, u-velocity, v-velocity, density and temperature distribution are shown in Fig. 6(a–f). The comparison with the Carter's data indicates reasonable agreements.

(b) *Supersonic flow on a compression corner*

In this example we demonstrate calculations of supersonic flow on a compression corner. The inlet boundary conditions (non-dimensionalized) are $\rho = 1$, $M = 2.25$, $p = 0.14$, $Re = 10^5$, $Pr = 0.72$, and $v = 0$, with adiabatic wall condition. The steady state background mean flowfields for the compression corner are shown in Fig. 7(a). In these calculations, all perturbation (fluctuation) variables are determined from time averages of the Navier–Stokes solutions according to (43). The horizontal and vertical perturbation velocities (u', v') at locations close to the wall ($x = 0.10256$ m, $y = 0.001$ m) and away from the wall ($x = 0.10256$ m, $y = 0.04$ m) are shown in Fig. 7(b). Note that u' is extremely unsteady whereas v' is significantly less unsteady close to the wall. Away from the wall, both u' and v' are almost steady. These trends are reflected in the turbulence (Reynolds) stresses as shown in Fig. 7(c). Turbulent kinetic energy distributions at the locations upstream of the corner ($x = 0.0513$ m) and downstream of the corner ($x = 0.1333$ m) are shown in Fig. 7(d). We observe that the turbulent kinetic energy downstream of the corner is significantly larger than the upstream. No turbulent statistics calculations (wave numbers or frequencies vs. power spectral density) are attempted at this time as turbulence microscales are not resolved in this example.

It should be noted that the above results obtained without turbulence models or without the standard DNS solutions (neither spectral nor DNS-mesh refinements) are regarded as the consequence of the time-averaging of the FDMEI Navier–Stokes solutions. This implies that the fluctuation of variables between nodal points (Fig. 2(a)) and between time steps (Fig. 2(b)) as reflected in terms of the implicitness parameters (s_i) have contributed to these physical phenomena, with compressibility and shock waves dictated by the Mach number-dependent s_1,

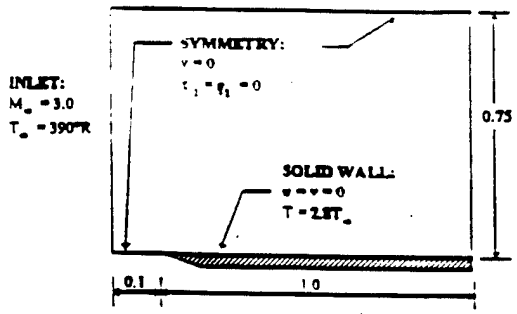

(a)

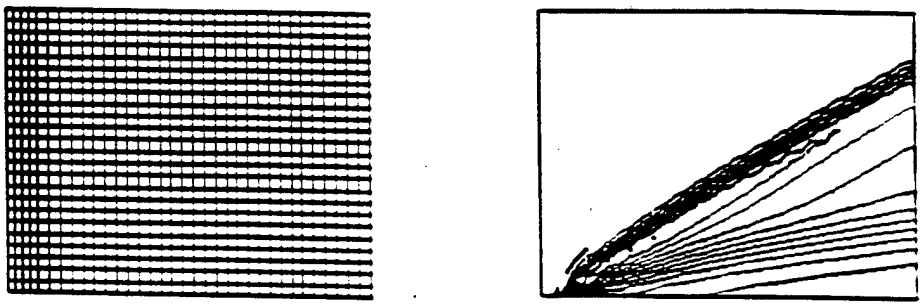

(b)

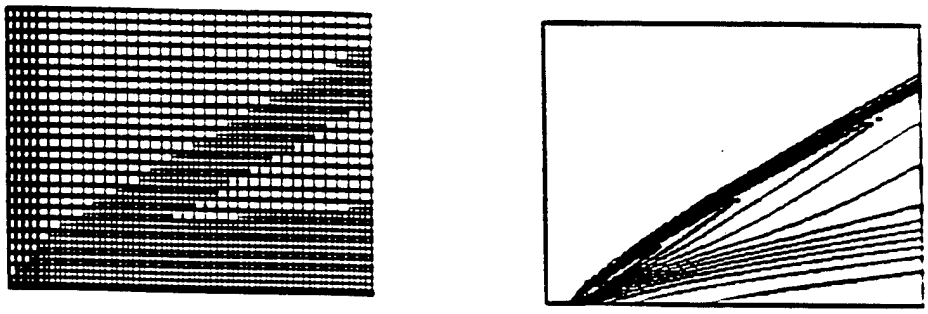

(c)

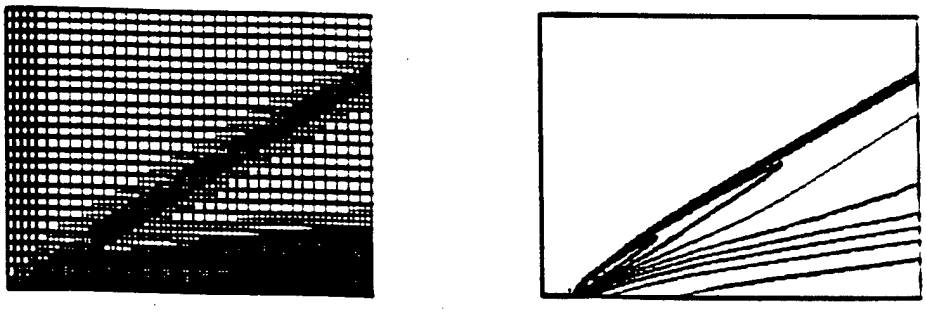

(d)

Fig. 4. Flat plate problem—initial and adaptive meshes and their corresponding density contours: (a) Geometry and boundary conditions of Carter's [17] flat plate problem. $M_\infty = 3$, $Re_L = 1000$, $T_\infty = 390°R$; (b) initial mesh (816 elements, 875 nodes) and the corresponding density contours, (max = 2.21 Kg/m^3, min = 0.5 Kg/m^3); (c) one-level adaptive mesh (1755 elements, 1889 nodes) and the corresponding density contours (max = 2.1 Kg/m^3, min = 0.5 Kg/m^3); (d) two-level adaptive mesh (4257 elements, 4547 nodes) and the corresponding density contours, (max = 2.0 Kg/m^3, min = 0.5 Kg/m^3).

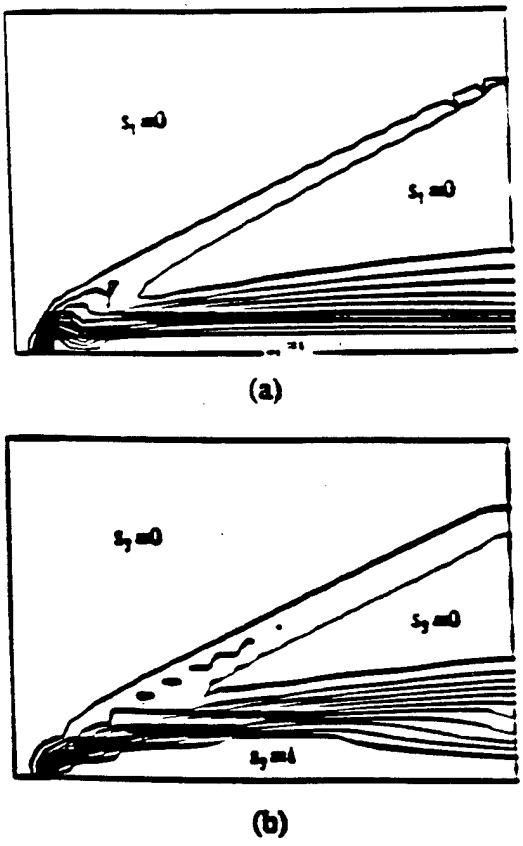

Fig. 5. Flowfield-dependent first-order convection and diffusion implicitness parameters: (a) s_1 contours; (b) s_3 contours.

and with incompressibility and turbulent fluctuation dictated by the Reynolds number or Peclet number-dependent (s_3). An equal participation of s_1 and s_3 will be responsible for shock wave turbulent boundary layer interactions. A comparison of the results of the FDMEI scheme with the κ-ε turbulent model and experimental data is shown in Fig. 7(e). It is seen that the FDMEI results compare more favorably with those of measurements [18].

(c) *FDMEI analysis of three-dimensional flows*

To demonstrate the effectiveness of the flowfield-dependent implicitness parameters in 3-D flows at the steady state, we examine the spatially evolving boundary layer (Fig. 8(a–e). Note that the contours of s_1 and s_3 (Fig. 8(c)) show the boundary layer effects in which both s_1 and s_3 are indicative of rapid changes of Mach numbers and Reynolds numbers, respectively, larger (close to unity) on the wall, but small (closer to zero) away from the wall. The velocity vectors and RMS error distributions versus interactions are shown in Fig. 8(d) and (e), respectively.

(d) *Demonstration of compressibility vs. incompressibility*

We ask the question: Can a single formulation or computer program originally designed for high speed compressible flows be applied to analyze the low speed incompressible flows? The advantage of FDMEI is to respond positively to this question. To prove the point, let us examine the lid-driven cavity flow at the steady state (Fig. 9(a–f)). Notice that, for $M = 0.1$, density changes occur closer to the lid, whereas, for $M = 0.01$, density is constant throughout the domain (Fig. 9(e)), corresponding to $P_{01}^{(r,s,q)}$ being variable and constant, respectively (see Eq. (42)). The equation of state for compressible flows is automatically switched over to accommodate the incompressible flows. This advantage is contrary to the previous practice such as the Table

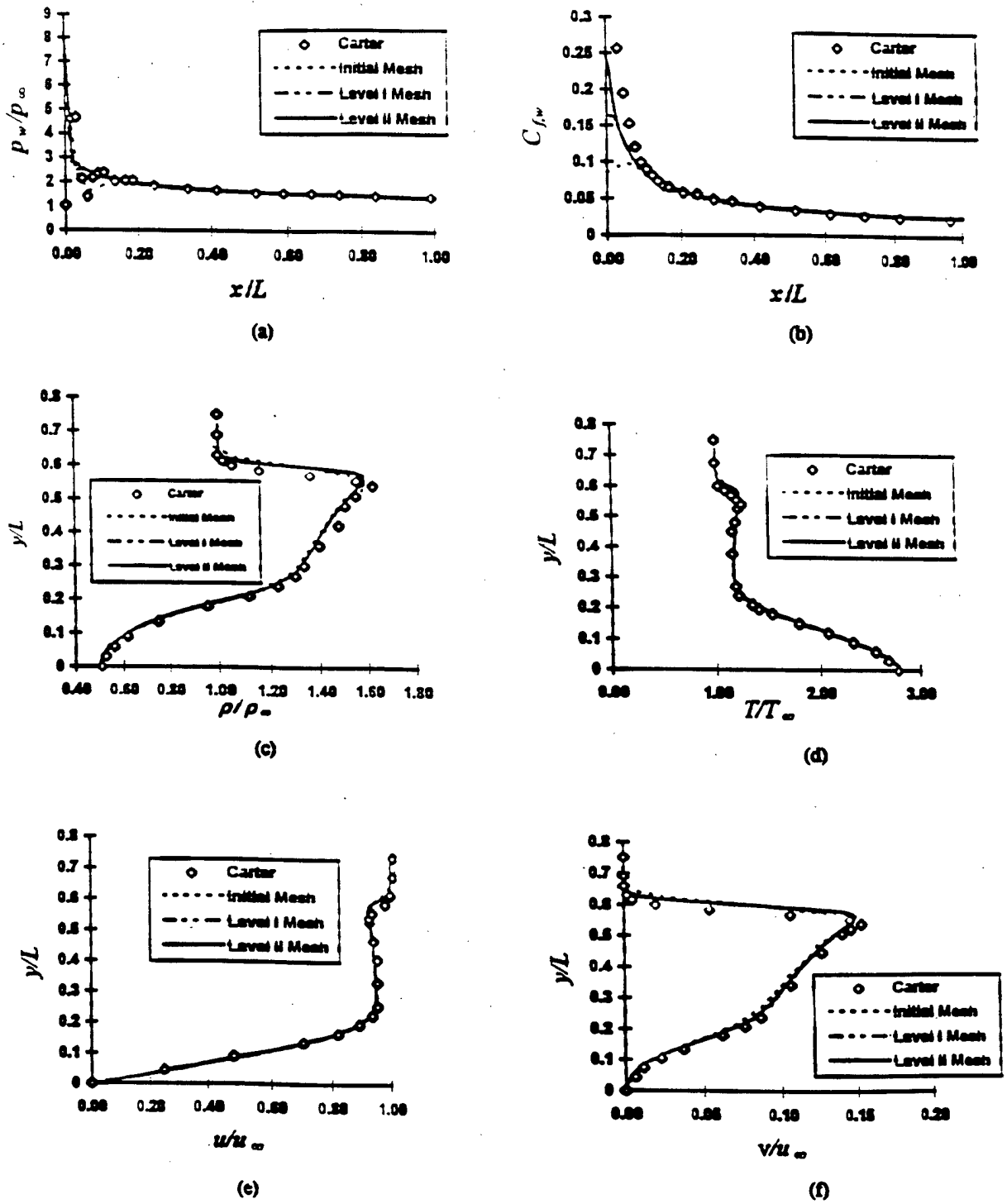

Fig. 6. Comparisons of various quantities with Carter [17]. (a) Wall pressure; (b) wall skin friction; (c) density distribution, $x/L = 1$; (d) temperature distribution, $x/L = 1$; (e) u-velocity, $x/L = 1$; (f) v-velocity, $x/L = 1$.

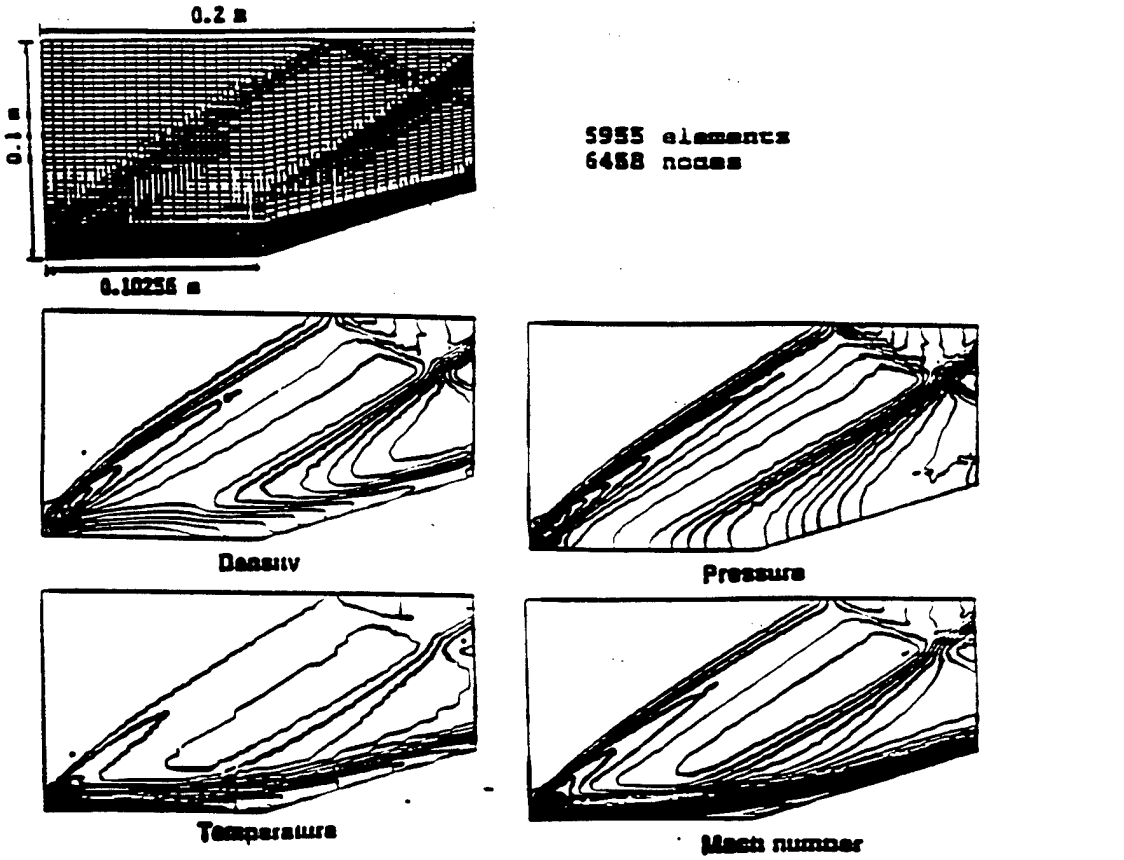

(a)

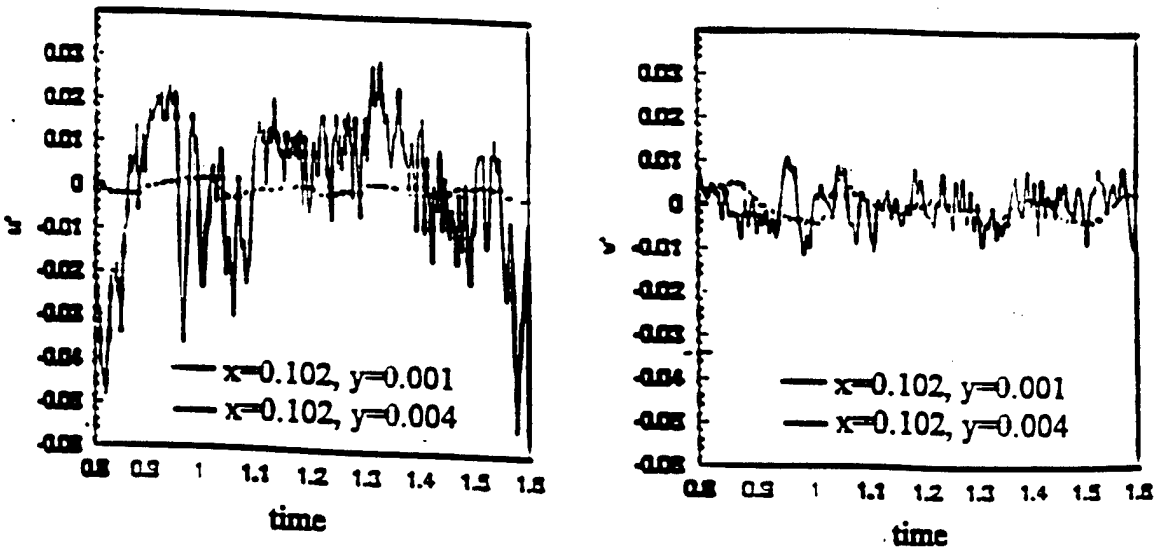

(b)

Fig. 7. Supersonic flow on a compression corner, $M_\infty = 2.25$: (a) Compression corner geometry and flowfields; (b) fluctuation velocities; (c) Reynolds stresses; (d) turbulent kinetic energy; (e) comparison velocity distribution of FDMEI with k-ε model and experimental data [18].

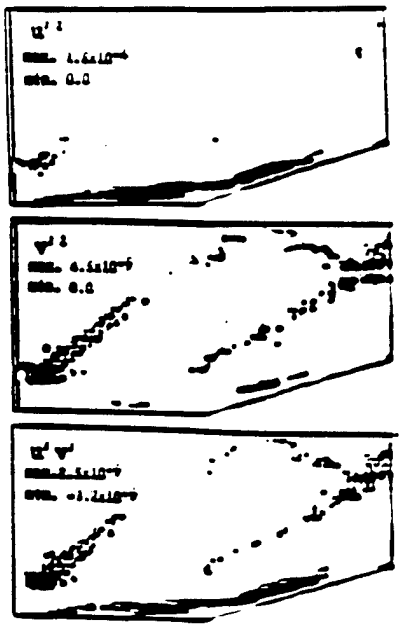

(c)

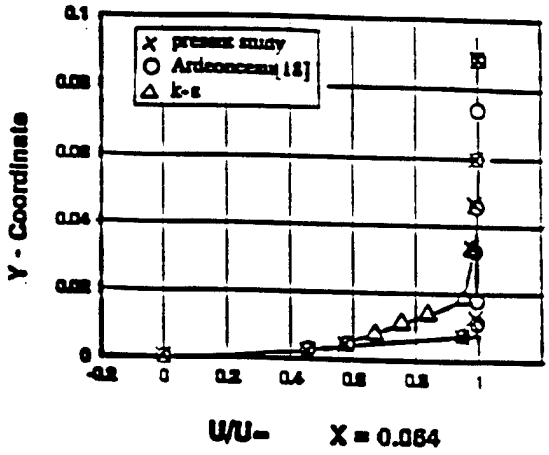

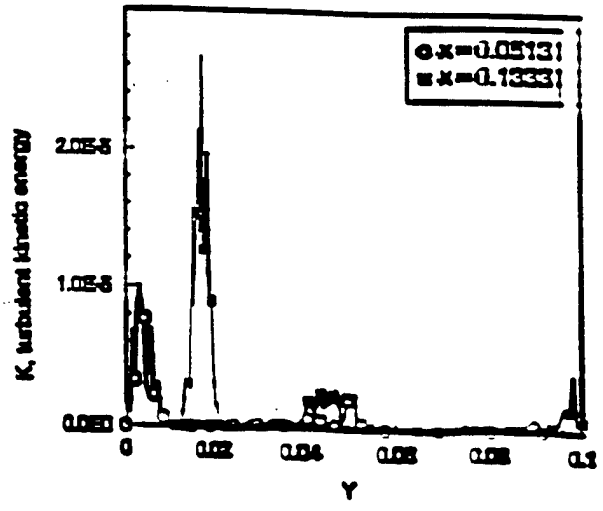

(d)

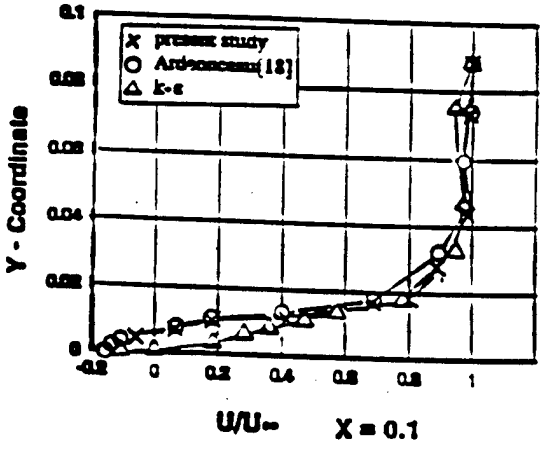

(e)

Fig. 7 (continued)

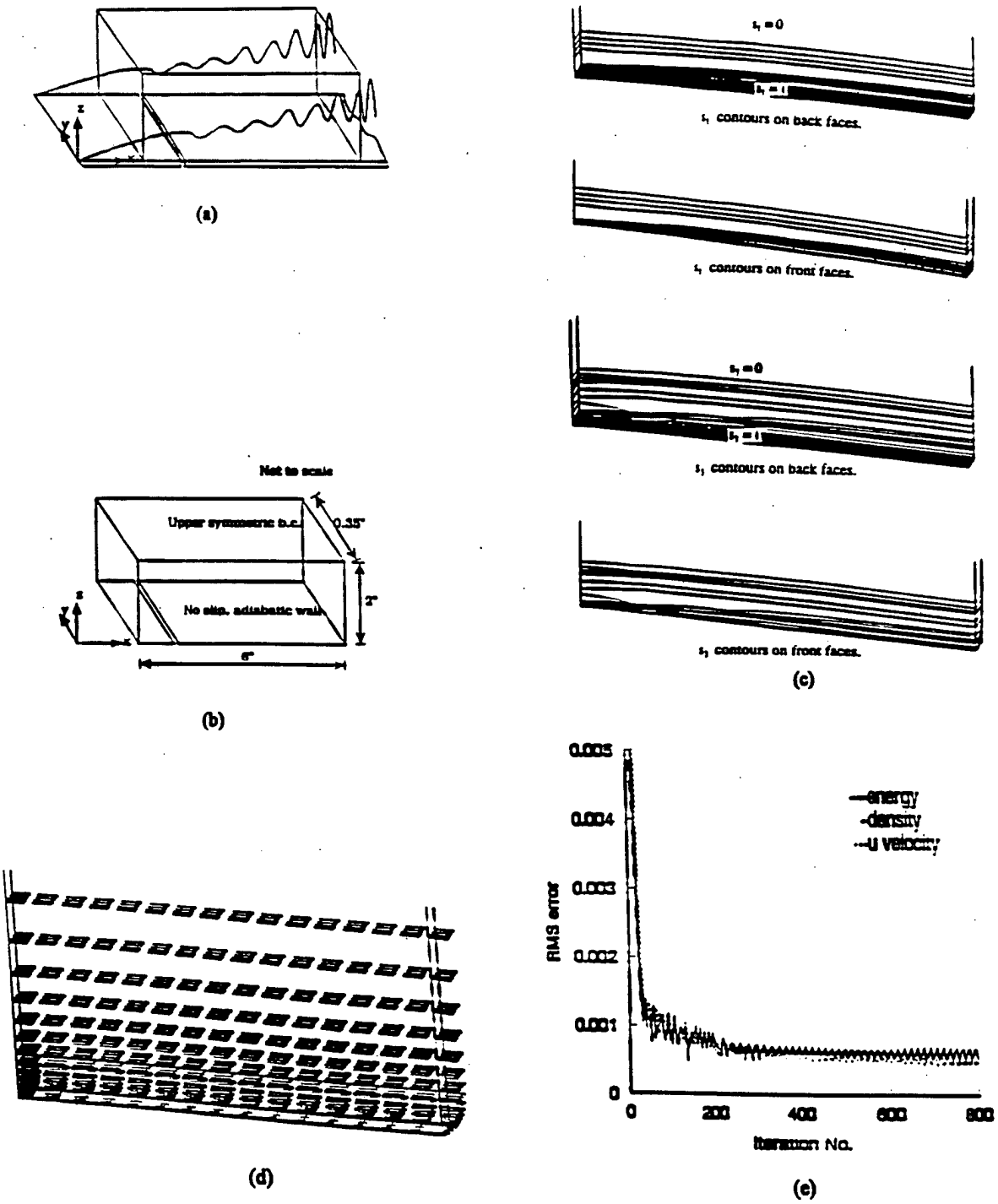

Fig. 8. Three-dimensional spatially evolving boundary layer flow: (a) Schematics of spatially evolving boundary layer flow; (b) computational geometry and boundary conditions; (c) flowfield-dependent first-order convection and diffusion implicitness parameter contours; (d) velocity vectors; (e) convergence history.

look-up for the equation of state for incompressible flow handled separately through hyperbolic elliptic equation as derived from the continuity equation combined with the momentum and energy equations. Comparison of the results of FDMEI with those of the independent incompressible flow code of Ghia et al. [19] are very favorable as shown in Fig. 9(f).

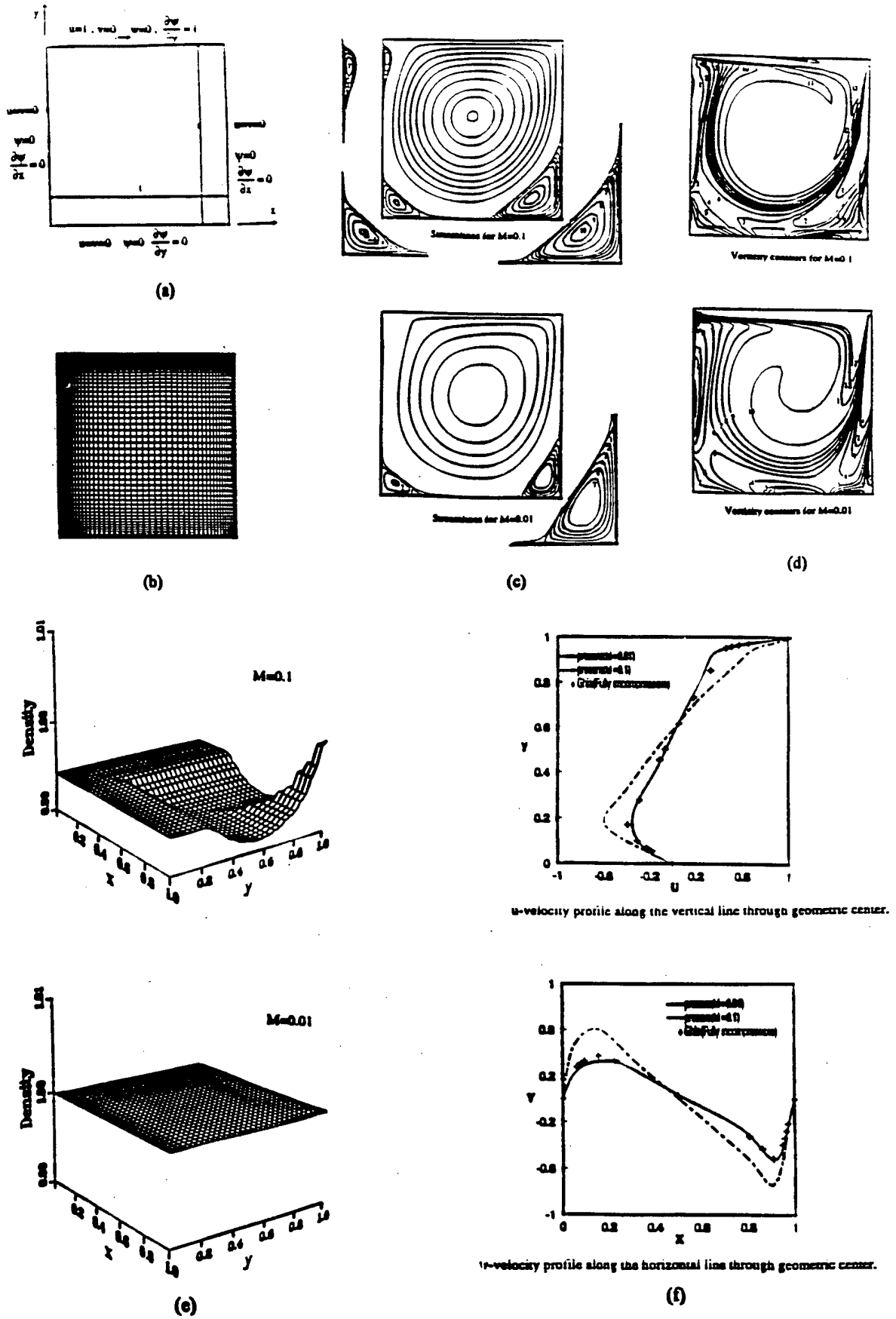

Fig. 9. Test of FDMEI scheme to solve incompressible flows-lid-driven cavity problem: (a) Geometry and boundary conditions; (b) mesh configuration; (c) streamline contours; (d) vorticity contours; (e) density distribution; (f) u- and v-velocity comparisons with Ghia et al. [19]; (g) stagnation pressure at M = 0.01 and M = 0.1.

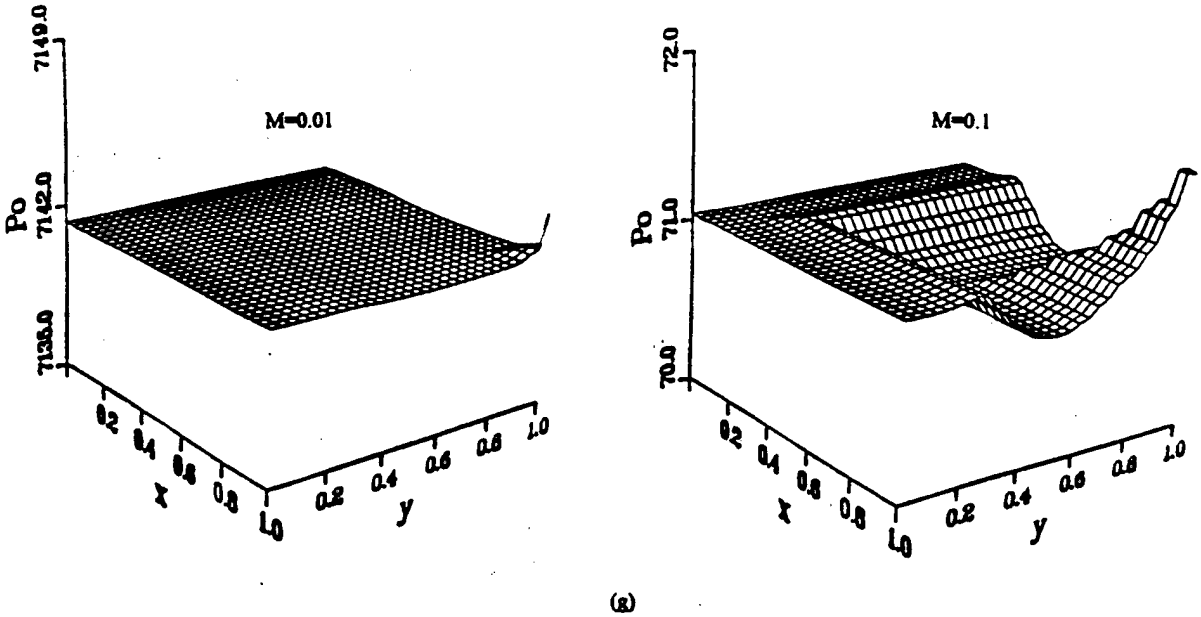

(g)

Fig. 9. (Continued)

5. Concluding remarks

The validity of the proposed new approach to computational fluid dynamics has been demonstrated through some example problems. Excluded from these examples are reacting flows which are reported elsewhere [16]. Also excluded is the effect of additional spectral modes of Legendre polynomials which are described in [15]. None of the example problems have been carried out with mesh refinements required for resolving turbulent microscales due to the limitation of computer time. The following concluding remarks are provided:

(a) The flowfield-dependent implicitness parameters as calculated from the current flowfield information are indicative of the magnitude of gradients of all variables and adjust the computational schemes accordingly for every nodal point or element, rather than dictated by arbitrarily selected constant parameters throughout the domain.

(b) The first-order implicitness parameters s_1, s_3, and s_5 as calculated from Mach numbers, Reynolds or Peclet numbers, and Damköhler numbers, respectively, ensure the solution accuracy, whereas the second-order implicitness parameters s_2, s_4 and s_6 which are determined as compliances of s_1, s_3 and s_5, respectively, assist in the solution stability.

(c) The FDMEI method is capable of resolving mutual interactions and transition between viscous and inviscid flows, compressible and incompressible flows, and laminar and turbulent flows, in all speed regimes. Further research on FDMEI is required in order to investigate many other physical phenomena including hypersonic and high temperature flows in 3D.

Appendix A. Analogies of FDMEI to currently available FDM and FEM schemes

Analogies of FDMEI to currently available computational schemes of FDM and FEM are summarized below.

A.1. Analogies of FDMEI to FDM

Some of the FDM schemes are compared with FDMEI in Table A.1.

Table A.1

	s_1	s_2	E	E	Q^n	Truncation error
Beam–Warming [1]	$\frac{\theta}{1+\xi}$	$\frac{\theta}{1+\xi}$	$\frac{\theta\,\Delta t}{1+\xi}(a_i+b_i)$	$\frac{\theta\,\Delta t}{1+\xi}c_{ij}$	$\frac{\Delta t}{1+\xi}W^n-\frac{\xi}{1+\xi}\Delta U^n$	$O\left[\left(\theta-\frac{1}{2}-\xi\right)\Delta t^2,\Delta x^2\right]$
Euler explicit	0	0	$\frac{\theta\,\Delta t}{1+\xi}(a_i+b_i)$	$\frac{\theta\,\Delta t}{1+\xi}c_{ij}$	$\frac{\Delta t}{1+\xi}W^n-\frac{\xi}{1+\xi}\Delta U^n$	$O(\Delta t^2)$
Euler implicit	1	1	$\frac{\theta\,\Delta t}{1+\xi}(a_i+b_i)$	$\frac{\theta\,\Delta t}{1+\xi}c_{ij}$	$\frac{\Delta t}{1+\xi}W^n+\frac{\xi}{1+\xi}\Delta U^n$	$O(\Delta t^2)$
Three-point implicit	$\frac{2}{3}$	$\frac{2}{3}$	$\frac{\theta\,\Delta t}{1+\xi}(a_i+b_i)$	$\frac{\theta\,\Delta t}{1+\xi}c_{ij}$	$\frac{\Delta t}{1+\xi}W^n+\frac{\xi}{1+\xi}\Delta U^n$	$O(\Delta(\Delta t^3))$
Trapezoidal implicit	$\frac{1}{2}$	$\frac{1}{2}$	$\frac{\theta\,\Delta t}{1+\xi}(a_i+b_i)$	$\frac{\theta\,\Delta t}{1+\xi}c_{ij}$	$\frac{\Delta t}{1+\xi}W^n+\frac{\xi}{1+\xi}\Delta U^n$	$O(\Delta t^3)$
Leap frog explicit	0	0	$\frac{\theta\,\Delta t}{1+\xi}(a_i+b_i)$	$\frac{\theta\,\Delta t}{1+\xi}c_{ij}$	$\frac{\Delta t}{1+\xi}W^n+\frac{\xi}{1+\xi}\Delta U^n$	$O(\Delta t^3)$

Other schemes of FDM are compared with FDMEI as follows:

(a) *Lax–Wendroff scheme*

The Lax–Wendroff scheme without artificial viscosity takes the form

$$\Delta U_i^{n+1} = -\frac{\Delta t}{\Delta x}(F_{i+1/2} - F_{i-1/2}) - \frac{\Delta t}{2\,\Delta x^2}[a_{i+1/2}F_{i+1} - (a_{i+1/2} - a_{i-1/2})F_i + a_{i-1/2}F_{i-1}] \tag{A.1}$$

This scheme arises if we set in FDMEI

$$a_{i+1/2} = a_{i-1/2} = a\,, \qquad s_1 = 0\,, \qquad s_2 = 0\,, \qquad s_3 = 0\,, \qquad s_4 = 0$$

(b) *Lax–Wendroff scheme with viscosity*

The Lax–Wendroff scheme with viscosity is given by

$$\Delta U_i^{n+1} = -\frac{\Delta t}{\Delta x}(F^*_{i+1/2} - F^*_{i-1/2}) \tag{A.2}$$

with

$$F^*_{i+1/2} = \frac{F_{i+1} + F_i}{2} - \frac{\Delta t}{2\,\Delta x}a_{i+1/2}(F_{i+1} - F_i) + D_{i+1/2}(U_{i+1} - U_i)$$

$$F^*_{i-1/2} = \frac{F_i + F_{i-1}}{2} - \frac{\Delta t}{2\,\Delta x}a_{i-1/2}(F_i - F_{i-1}) + D_{i-1/2}(U_i - U_{i-1})$$

This scheme arises if we set

$$D_{i+1/2} = D_{i-1/2} = as_1\,, \qquad s_2 = 0\,, \qquad s_3 = 0\,, \qquad s_4 = 0$$

This implies that as_1 in FDMEI plays a role of artificial viscosity which is manually implemented in the Lax–Wendroff scheme.

(c) *Explicit McCormack scheme*

Combining the predictor corrector steps of McCormack scheme we write

$$\Delta U_i^{n+1} = -\frac{\Delta t}{\Delta x}(F_{i+1}^n - F_i^n) - \frac{\Delta t}{\Delta x}(F_i^{n+1} - F_{i-1}^{n+1}) - D$$

$$= -\frac{\Delta t}{\Delta x}(F_{i+1}^n - F_i^n) - \frac{\Delta t}{\Delta x}(F_{i+1/2}^{n+1} - F_{i-1/2}^{n+1})$$

$$-\frac{\Delta t}{\Delta x^2}[a_{i+1/2}F_{i+1} - (a_{i+1/2} + a_{i-1/2})F_i + a_{i-1/2}F_{i-1}] - D \tag{A.3}$$

The FDMEI becomes identical to this scheme with the following adjustments:

$$a_{i+1/2} = a_{i-1/2} = a$$

$$F_i^n - F_{i-1}^n = F_{i+1}^n - F_i^n + F_{i+1/2} - F_{i-1/2}$$

$$s_1 = 0, \quad s_2 = 0, \quad s_3 = 0, \quad s_4 = 0$$

and the s_2 term in the FDMEI method is equivalent to

$$D_i = \frac{\omega}{8}(U_{i+1/2}^n - 4U_{i+1}^n + 6U_i^n - 4U_{i-1}^n + U_{i-2}^n)$$

This again is a manifestation that shows the equivalent of the s_2 terms is manually supplied in the McCormack method.

(d) *First-order upwind scheme*

This scheme is written as

$$\Delta U_i^{n+1} = -\frac{\Delta t}{\Delta x}(F_{i+1/2}^* - F_{i-1/2}^*)$$

$$= -\frac{\Delta t}{\Delta x}\left\{\left[\frac{1}{2}(F_i^n + F_{i+1}^n) - \frac{1}{2}|a|(U_{i+1}^n - U_i^n)\right] - \left[\frac{1}{2}(F_i^n + F_{i-1}^n) - \frac{1}{2}|a|(U_i^n - U_{i-1}^n)\right]\right\} \tag{A.4}$$

The FDMEI analogy is obtained by setting

$$F_i^n = \frac{1}{2}F_{i+1}^n, \qquad F_{i-1}^n = \frac{1}{2}F_{i-1}^n$$

$$s_2 aC(\Delta U_i^{n+1} - 2\Delta U_{i-1}^{n+1} + \Delta U_{i-2}^{n+1}) = |a|(U_{i+1}^n - U_{i-1}^n)$$

where C is the Courant number.

(e) *Implicit McCormack scheme*

With all second-order derivatives removed from (11) we obtain the implicit McCormack Scheme by setting $s_1 = 1$, $s_2 = 0$, $s_3 = 0$, $s_4 = 0$. However, it is necessary to divide the process into the predictor and corrector steps. Once again, the flowfield-dependent implicitness parameters for FDMEI will allow the computation to be performed in a single step.

(f) *PISO and SIMPLE*

The basic idea of PISO and SIMPLE is analogous to FDMEI-FEM in that the pressure correction process is a separate step in PISO or SIMPLE, whereas the concept of pressure correction is implicitly embedded in FDMEI-FEM by updating the implicitness parameters based on the upstream and downstream Mach numbers and Reynolds numbers within an element.

The elliptic nature of the pressure Poisson equation in the pressure correction process resembles the terms embedded in the $B_{\alpha\beta rs}$ terms in (3.6). Specifically, examine the s_2 terms involving $a_{irq}a_{jsq}$ and $b_{irq}a_{jsq}$ and s_4 term involving $a_{irq}b_{jsq}$. All of these terms are multiplied by $\Phi_{\alpha,i}\Phi_{\beta,j}$ which provide dissipation against any pressure oscillations. Question: Exactly when is such dissipation action needed? This is where the importance of implicitness parameters based on flowfield parameters comes in. As the Mach number becomes very small

(incompressibility effects dominate) the implicitness parameters s_2 and s_3 calculated from the current flowfield will be indicative of pressure correction required. Notice that a delicate balance between Mach number (s_2 is Mach number dependent) and Reynolds number or Peclet number (s_3 is Reynolds number or Peclet number dependent) is a crucial factor in achieving convergent and stable solutions. Of course, on the other hand, high Mach number flows are also dependent on these implicitness parameters. In this case all implicitness parameters, s_1, s_2, s_3, s_4 will play important roles.

A.2. Analogies of FDMEI to FEM

(a) *Generalized Taylor Galerkin (GTG) with convection and diffusion Jacobians*

Earlier developments for the solution of Navier–Stokes system of equations were based on GTG without using the implicitness parameters. They can be shown to be special cases of FDMEI-FEM.

In terms of both diffusion Jacobian and diffusion gradient Jacobian, we write

$$\frac{\partial \boldsymbol{G}_i}{\partial t} = \boldsymbol{b}_i \frac{\partial \boldsymbol{U}}{\partial t} + \boldsymbol{c}_{ij} \frac{\partial \boldsymbol{V}_j}{\partial t}$$

with

$$\boldsymbol{b}_i = \frac{\partial \boldsymbol{G}_i}{\partial \boldsymbol{U}}, \qquad \boldsymbol{c}_{ij} = \frac{\partial \boldsymbol{G}_i}{\partial \boldsymbol{V}_j}, \qquad \boldsymbol{V}_i = \frac{\partial \boldsymbol{U}}{\partial x_j}$$

Thus, it follows from (10) with $s_1 = s_3 = s_4 = s_5 = s_6 = 0$ and $s_2 = 1$ that

$$\Delta \boldsymbol{U}^{n+1} = \Delta t \left(-\frac{\partial \boldsymbol{F}_i}{\partial x_i} - \frac{\partial \boldsymbol{G}_i}{\partial x_i} + \boldsymbol{B} \right)^n + \frac{\Delta t^2}{2} \frac{\partial}{\partial t} \left(-\frac{\partial \boldsymbol{F}_i}{\partial x_i} - \frac{\partial \boldsymbol{G}_i}{\partial x_i} + \boldsymbol{B} \right)^{n+1} - \mathrm{O}(\Delta t^3) \tag{A.5}$$

Using the definitions of convection, diffusion, and diffusion rate Jacobians discussed in Section 2, the temporal rates of change of convection and diffusion variables may be written as follows:

$$\begin{aligned}
\frac{\partial \boldsymbol{F}_i^n}{\partial t} &= \left(\boldsymbol{a}_i \frac{\partial \boldsymbol{U}}{\partial t} \right)^n = \left[\boldsymbol{a}_i \left(-\frac{\partial \boldsymbol{F}_j}{\partial x_j} - \frac{\partial \boldsymbol{G}_j}{\partial x_j} + \boldsymbol{B} \right) \right]^n \\
\frac{\partial \boldsymbol{F}_i^{n+1}}{\partial t} &= \boldsymbol{a}_i \left[\left(-\boldsymbol{a}_j \frac{\partial}{\partial x_j} (\boldsymbol{U}^{n+1} - \boldsymbol{U}^n) - \frac{\partial \boldsymbol{F}_j^n}{\partial x_j} - \frac{\partial \boldsymbol{G}_j^{n+1}}{\partial x_j} + \boldsymbol{B}^{n+1} \right) \right] \\
\frac{\partial \boldsymbol{G}_i^{n+1}}{\partial t} &= \left(\boldsymbol{b}_i \frac{\partial \boldsymbol{U}}{\partial t} \right)^{n+1} + \left[\boldsymbol{c}_{ij} \frac{\partial}{\partial t} \left(\frac{\partial \boldsymbol{U}}{\partial x_j} \right) \right]^{n+1}
\end{aligned} \tag{A.6}$$

or

$$\frac{\partial \boldsymbol{G}_i^{n+1}}{\partial t} = \left(\boldsymbol{b}_i - \frac{\partial \boldsymbol{c}_{ij}}{\partial x_j} \right) \frac{\Delta \boldsymbol{U}^{n+1}}{\Delta t} + \frac{\partial}{\partial x_j} \left(\boldsymbol{c}_{ij} \frac{\Delta \boldsymbol{U}}{\Delta t} \right)^{n+1} \tag{A.7}$$

Substituting (A.6) and (A.7) into (A.5) yields

$$\begin{aligned}
\Delta \boldsymbol{U}^{n+1} = \Delta t \left(-\frac{\partial \boldsymbol{F}_i}{\partial x_i} - \frac{\partial \boldsymbol{G}_i}{\partial x_i} + \boldsymbol{B} \right)^n + \frac{\Delta t^2}{2} \Bigg\{ \frac{\partial}{\partial x_i} \Bigg[-\boldsymbol{a}_i \left(-\boldsymbol{a}_j \frac{\partial \Delta \boldsymbol{U}^{n+1}}{\partial x_j} - \frac{\partial \boldsymbol{F}_j^n}{\partial x_j} - \frac{\partial \boldsymbol{G}_j^{n+1}}{\partial x_j} + \boldsymbol{B}^{n+1} \right) \\
+ \left(\boldsymbol{e}_i + \frac{\partial \boldsymbol{c}_{ij}}{\partial x_j} \right) \frac{\Delta \boldsymbol{U}^{n+1}}{\Delta t} + \frac{\partial \boldsymbol{B}^{n+1}}{\partial t} \Bigg] \Bigg\}
\end{aligned} \tag{A.8}$$

Assuming that

$$\boldsymbol{e}_i = \boldsymbol{b}_i - \frac{\partial \boldsymbol{c}_{ij}}{\partial x_j} \cong 0$$

and neglecting the spatial and temporal derivatives of $\boldsymbol{B}$, we rewrite (A.8) in the form

$$\left\{1 - \frac{\Delta t^2}{2}\frac{\partial}{\partial x_i}\left(a_i a_j - \frac{c_{ij}}{\Delta t}\right)\frac{\partial}{\partial x_j}\right\}\Delta U^{n+1} = H^n$$

$$H^n = \Delta t\left(-\frac{\partial F_i}{\partial x_i} - \frac{\partial G_i}{\partial x_i} - B\right)^n - \frac{\Delta t^2}{2}\frac{\partial}{\partial x_i}\left(a_i\frac{\partial F_j}{\partial x_j}\right)^n \tag{A.9}$$

Here, the second derivatives of G_i are neglected and all Jacobians are assumed to remain constant within an incremental time step but updated at subsequent time steps.

Applying the Galerkin finite element formulation, we have an implicit scheme.

$$(A_{\alpha\beta}\delta_{rs} + B_{\alpha\beta rs})\,\Delta U^{n+1}_{\beta s} = H^n_{\alpha r} + N^{n+1}_{\alpha r} - N^n_{\alpha r} \tag{A.10}$$

where

$$B_{\alpha\beta rs} = \frac{\Delta t^2}{2}\int_\Omega\left[\left(a_{irq}a_{jsq} + \frac{c_{ijrs}}{\Delta t}\right)\Phi_{\alpha,i}\Phi_{\beta,j}\right]\mathrm{d}\Omega$$

$$H^n_{\alpha r} = \Delta t\int_\Omega\left[\Phi_{\alpha,i}\Phi_\beta(F^n_{\beta ir} - G^n_{\beta ir}) - \Phi_\alpha\Phi_\beta B^n_{\beta r} - \frac{\Delta t^2}{2}a_{isr}\Phi_{\alpha,i}\Phi_{\beta,j}F^n_{\beta js}\right]\mathrm{d}\Omega$$

$$N^{n+1}_{\alpha r} = \frac{\Delta t^2}{2}\int_\Gamma\left(a_{irq}a_{jsq} - \frac{c_{ijrs}}{\Delta t}\right)\Phi_{\alpha,i}\,\Delta U^{n+1}_{js}\,n_i\,\mathrm{d}\Gamma$$

$$N^n_{\alpha r} = -\int_\Gamma\left[\Delta t\,\Phi_\alpha(F^n_{ir} - G^n_{ir}) - \frac{\Delta t^2}{2}a_{isr}\Phi_\alpha F^n_{js,j}\right]n_i\,\mathrm{d}\Gamma$$

Here, we note that the algorithm given by (A.10) results from (33) by setting $s_1 = s_3 = s_4 = 0$, $s_2 = 1$, $b_{irq}a_{jsq} = c_{ijrs}/\Delta t$, and neglecting the terms with b_{jrs} and derivatives of G_i and B, the form identical to that reported by Hassan et al. [13].

(b) *GTG with convection Jacobians*

Diffusion Jacobians may be neglected if their influences is negligible. In this case the Taylor–Galerkin finite element analog may be derived using only the convective Jacobian from the Taylor series expansion

$$U^{n+1} = U^n + \Delta t\frac{\partial U^n}{\partial t} + \frac{\Delta t^2}{2}\frac{\partial^2 U^n}{\partial t^2} + \mathrm{O}(\Delta t^3) \tag{A.11}$$

where

$$\frac{\partial U}{\partial t} = -\frac{\partial F_i}{\partial x_i} - \frac{\partial G_i}{\partial x_i} + B = -a_i\frac{\partial U}{\partial x_i} - \frac{\partial G_i}{\partial x_i} + B$$

$$\frac{\partial^2 U}{\partial t^2} = -\frac{\partial}{\partial t}\left(a_i\frac{\partial U}{\partial x_i} + \frac{\partial G_i}{\partial x_i} - B\right) \tag{A.12}$$

or

$$\frac{\partial^2 U}{\partial t^2} = \frac{\partial}{\partial x_i}\left(a_i a_j\frac{\partial U}{\partial x_i}\right) + \frac{\partial}{\partial x_i}\left(a_i\frac{\partial G_j}{\partial x_j}\right) - \frac{\partial}{\partial x_i}(a_i B) + \frac{\partial B}{\partial t} \tag{A.13}$$

Substituting (A.12) and (A.13) into (A.11), we obtain

$$\Delta U^{n+1} = \Delta t\left\{-\frac{\partial F_i}{\partial x_i} - \frac{\partial G_i}{\partial x_i} + B + \frac{\Delta t}{2}\left[\frac{\partial}{\partial x_j}\left(a_i a_j\frac{\partial U}{\partial x_i}\right) + \frac{\partial^2(a_i G_j)}{\partial x_i\,\partial x_j} + \frac{\partial}{\partial x_i}(a_i B) + \frac{\partial B}{\partial t}\right]\right\}^n \tag{A.14a}$$

Expanding $\partial F_j/\partial t$ at $(n+1)$ time step

$$\frac{\partial F^{n+1}_j}{\partial t} = \left[a_i\left(-\frac{\partial F_j}{\partial x_j} - \frac{\partial G_j}{\partial x_j} + B\right)\right]^{n+1} = a^{n+1}_i\left[-a_j\frac{\partial\Delta U^{n+1}}{\partial x_j} - \frac{\partial F^n_j}{\partial x_j} - \frac{\partial G^{n+1}_j}{\partial x_j} + B^{n+1}\right]$$

and substituting the above into (A.11)–(A.13), we arrive at ΔU^{n+1} in a form different from (A.14a).

$$\Delta U^{n+1} = \Delta t\left(-\frac{\partial F}{\partial x_i} - \frac{\partial G}{\partial x} - B \right)^n - \frac{\Delta t^2}{2}\left\{ \frac{\partial}{\partial x_i}\left(a_i a_j \frac{\partial \Delta U^{n+1}}{\partial x_j} - a_i \frac{\partial F^n}{\partial x_j} \right) - \frac{\partial^2 (a_i G_i)^{n+1}}{\partial x_i \partial x_i} - \frac{\partial}{\partial x_i}(a_i B)^{n+1} - \frac{\partial B^{n+1}}{\partial t} \right\} \tag{A.14b}$$

$$H^n = \left[1 - \frac{\Delta t^2}{2}\frac{\partial}{\partial x_i}\left(a_i a_j + \frac{c_{ij}}{\Delta t} \right)\frac{\partial}{\partial x_j} \right] \Delta U^{n+1}$$

$$H^n = \Delta t\left(-\frac{\partial F_i}{\partial x_i} - \frac{\partial G_i}{\partial x_i} + B \right)^n + \frac{\Delta t^2}{2}\frac{\partial}{\partial x_i}\left(a_i \frac{\partial F}{\partial x_j} \right)^n \tag{A.14c}$$

where second derivatives of G_i is assumed to be negligible and B is constant in space and time, arriving at an implicit finite element scheme.

$$(A_{\alpha\beta}\delta_{rs} + B_{\alpha\beta rs})\,\Delta U^{n+1}_{\beta s} = H^n_{\alpha r} + N^{n+1}_{\alpha r} + N^n_{\alpha r} \tag{A.15}$$

where

$$A_{\alpha\beta} = \int_\Omega \Phi_\alpha \Phi_\beta \, d\Omega$$

$$B_{\alpha\beta rs} = \frac{\Delta t^2}{2}\int_\Omega \left[\left(a_{irq} a_{jsq} + \frac{c_{ijrs}}{\Delta t} \right) \Phi_{\alpha,i} \Phi_{\beta,j} \right] d\Omega$$

$$H^n_{\alpha r} = \Delta t \int_\Omega \left[\Phi_{\alpha,i} \Phi_\beta (F^n_{\beta ir} + G^n_{\beta ir}) - \Phi_\alpha \Phi_\beta B^n_{\beta r} - \frac{\Delta t^2}{2} a_{irs} \Phi_{\alpha,i} \Phi_{\beta,j} F^n_{\beta js} \right] d\Omega$$

$$N^{n+1}_{\alpha r} = \frac{\Delta t^2}{2}\int_\Gamma \left(a_{irq} a_{jsq} + \frac{c_{ijrs}}{\Delta t} \right) \overset{*}{\Phi}_\alpha \, \Delta U^{n+1}_{sj} n_i \, d\Gamma$$

$$N^n_{\alpha r} = -\int_\Gamma \left[\Delta t \, \overset{*}{\Phi}_\alpha (F^n_{ir} + G^n_{ir}) - \frac{\Delta t^2}{2} a_{irs} \overset{*}{\Phi}_\alpha F^n_{js,j} \right] n_i \, d\Gamma$$

It should be noted that the form (A.15) arises from (23) with $s_1 = s_3 = s_4 = b_i = 0$ and $s_2 = 1$, an algorithm similar to Hassan et al. [13].

(c) *Generalized Petrov–Galerkin (GPG)*

The Generalized Petrov–Galerkin (GPG) method can be identified by setting $s_1 = s_2 = 1$, $s_3 = s_4 = 0$, $b_i = c_{ij} = d = 0$, $Q^n = 0$, $E_i = a_i$ and $E_{ij} = \frac{1}{2}\Delta t^2 a_i a_j$, so that (10) takes the form

$$\frac{\Delta U}{\Delta t} + a_i \frac{\partial \Delta U}{\partial x_i} - \frac{\Delta t}{2} a_i a_j \frac{\partial^2 \Delta U}{\partial x_i \partial x_j} = 0 \tag{A.16}$$

For the steady state non-incremental form in 1-D we write (A.16) in the form

$$a\frac{\partial u}{\partial x} - \Delta t \frac{a^2}{2}\frac{\partial^2 u}{\partial x^2} = 0 \tag{A.17}$$

Taking the Galerkin integral of (A.17) leads to

$$\int \Phi_N^{(e)}\left(a\frac{\partial u}{\partial x} - \Delta t \frac{a^2}{2}\frac{\partial^2 u}{\partial x^2} \right) dx = 0$$

or

$$\int W_N^{(e)} a \frac{\partial u}{\partial x} \, dx = 0 \tag{A.18}$$

for vanishing Neumann boundaries. Here, $\Psi_N^{(e)}$ is the Petrov–Galerkin test function,

$$\Psi_N^{(e)} = \Phi_N^{(e)} - \alpha h \frac{\partial \Phi_N^{(e)}}{\partial x} \tag{A.19}$$

with $\alpha = C/2$ and $C = a\,\Delta t/\Delta x$ being the Courant number.

For isoparametric coordinates in two dimensions, the Petrov–Galerkin test function assumes the form

$$\Psi_N^{(e)} = \Phi_N^{(e)} + \beta g_i \frac{\partial \Phi_N^{(e)}}{\partial x_i} \tag{A.20}$$

with

$$\beta = \frac{1}{4}(\bar{\alpha}_\xi h_\xi + \bar{\alpha}_\eta h_\eta)\,,$$

$$\bar{\alpha}_\xi = \coth\left(\frac{R_\xi}{2}\right) - \frac{2}{R_\xi}, \qquad \bar{\alpha}_\eta = \coth\left(\frac{R_\eta}{2}\right) - \frac{2}{R_\eta}$$

$$g_i = \frac{v_i}{\sqrt{v_j v_j}}$$

where R_ξ is the Reynolds number of Peclet number in the direction of isoparametric coordinates (ξ, η). Note that the GPG process given by (A.16)–(A.20) leads to the Streamline Upwinding Petrov–Galerkin (SUPG) scheme as a special case.

(d) *Characteristic-based Zienkiewicz–Codina scheme*

This scheme arises from Eq. (8) by splitting the FDMEI Navier–Stokes system of equations into three parts for continuity, momentum and energy, separately. The governing equations for FDMEI given by Eq. (8) with all diffusion terms neglected can be written in the form,

$$\Delta \boldsymbol{U}^{n+1} = -\Delta t\left[\frac{\partial \boldsymbol{F}^n}{\partial x_i} + s_1 \frac{\partial \boldsymbol{a}_i\,\Delta \boldsymbol{U}^{n+1}}{\partial x_i} - \frac{\Delta t}{2}\left(\frac{\partial^2 \boldsymbol{a}_i F_i^n}{\partial x_i\,\partial x_j} + s_2 \frac{\partial^2 \boldsymbol{a}_i \boldsymbol{a}_j\,\Delta \boldsymbol{U}^{n+1}}{\partial x_i\,\partial x_j}\right)\right] \tag{A.21}$$

Continuity

The continuity equation can be extracted from (A.21) by setting as follows:

$$\Delta \boldsymbol{U}^{n+1} \to \Delta \rho^{n+1}$$

$$\boldsymbol{F}_i^n \to \rho v_i^n \to U_i^n$$

$$s_1 \boldsymbol{a}_i\,\Delta \boldsymbol{U}^{n+1} \to s_1\,\Delta \rho\, v_i^n \to \theta_1\,\Delta U_i^n$$

$$1/2 \boldsymbol{a}_i \boldsymbol{F}_j^n \to \theta_1 p^n \delta_{ij}$$

$$1/2 s_2 \boldsymbol{a}_i \boldsymbol{a}_j\,\Delta \boldsymbol{U}^{n+1} \to \theta_1 \theta_2\,\Delta p^{n+1}\,\delta_{ij}$$

These substitutions to (A.21) lead to

$$\Delta \rho^{n+1} = \left(\frac{1}{a^2}\Delta \rho\right)^{n+1} = -\Delta t\left[\frac{\partial (\rho v_i)^n}{\partial x_i} + \theta_1 \frac{\partial (\Delta \rho v_i)^{n+1}}{\partial x_i} - \Delta t\,\theta_1\left(\frac{\partial^2 p^n}{\partial x_i\,\partial x_j} + \theta_2\left(\frac{\partial^2 \Delta p^{n+1}}{\partial x_i\,\partial x_j}\right)\right)\right] \tag{A.22}$$

which is identical to Eq. (33) in [14] with $(\Delta \rho v_i)^{n+1}$ being the intermediate step. This represents the pressure correction process in case the flow is incompressible.

Momentum

A similar procedure can be applied to (A.21) for the momentum equations.

$$(\Delta \rho v_j)^{n+1} = -\Delta t\left[\frac{\partial (\rho v_i v_j)^n}{\partial x_i} - \frac{\partial \tau_{ij}^n}{\partial x_i} + \theta_2 \frac{\partial \Delta p^{n+1}}{\partial x_j}\right] - (1-\theta_2)\left[\frac{\Delta t^2}{2} v_k \frac{\partial^2}{\partial x_k\,\partial x_i}(\rho v_i v_j + p\delta_{ij})^n\right] \tag{A.23}$$

which is equivalent to Eq. (30) in [14] with $a = v_i$, $1 - \theta_2 = s_1$, and all terms of s_2, b_i and c_j being neglected in FDMEI.

Energy

Again, from (A.21), neglecting all $n+1$ terms of the FDMEI equation, we obtain

$$(\Delta\rho E)^{n+1} = -\Delta t\left[\frac{\partial(\rho E v_i + v_i p)^n}{\partial x_i} - \frac{\partial}{\partial x_i}\left(k\frac{\partial T}{\partial x_i} - \tau_{ij}v_j\right)^n\right] - \frac{\Delta t}{2}v_j\frac{\partial^2}{\partial x_j\,\partial x_i}(\rho E v_i + v_i p)^n \tag{A.24}$$

which corresponds to Eq. (40) of [14]. The solution steps begin with (A.23), followed by (A.21) and (A.24), and continue iteratively until convergence. Note that the pressure corrections for incompressibility are internally carried out in FDMEI as the pressure second derivatives arise in Eq. (10). Note also that in FDMEI all implicit terms may be retained for computational accuracy and efficiency for any physical situation.

References

[1] R.M. Beam and R.F. Warming, An implicit finite-difference algorithm for hyperbolic systems in conservation law form, J. Comput. Phys. 22 (1978) 87–110.

[2] A. Harten, High resolution schemes for hyperbolic conservation laws, J. Comput. Phys. 49 (1983) 357–393.

[3] R.W. MacCormack, Current status of numerical solutions of the Navier–Stokes equations, AIAA Paper 88-0513, 1988.

[4] W.R. Briley and H. McDonald, On the structure and use of linearized block implicit schemes, J. Comput. Phys. 34 (1980) 54–73.

[5] A. Jameson, W. Schmidt and E. Turkel, Numerical simulation of the Euler equations by finite volume methods using Runge–Kutta time stepping schemes, AIAA Paper 81-1259, AIAA 5th Computational Fluid Dynamics Conference, 1981.

[6] C. Hirsch, Numerical Computation of Internal and External Flows, Vol. I: Fundamentals of Numerical Discretization (Wiley, New York, 1988).

[7] C. Hirsch, Numerical Computation of Internal and External Flows, Vol. II: Computational Methods for Inviscid and Viscous Flows (Wiley, New York, 1990).

[8] T.J. Chung, Finite Element Analysis in Fluid Dynamics (McGraw-Hill, New York, 1978).

[9] I. Babuska and M. Suri, The *h-p* version of the finite element method with quasi-uniform meshes, Math. Model. Numer. Anal. (RAIRO) 21 (1987) 235.

[10] J. Oden, L. Demkowicz, W. Rachowicz and T. Westermann, Toward a universal *h-p* adaptive finite element strategy: Part II: A posteriori error estimation, Comput. Methods Appl. Mech. Engrg. 77 (1989) 113–1989.

[11] T.J.R. Hughes, L. Franca and M. Mallet, A new finite element formulation for computational fluid dynamics: I. Symmetric forms of the compressible Euler and Navier–Stokes equations and the second law of thermodynamics, Comput. Methods Appl. Mech. Engrg. 54 (1986) 223–234.

[12] J.T. Oden, Theory and implementation of high-order adaptive *hp*-methods for the analysis of incompressible viscous flows, in: S.N. Atluri, ed., Computations in Nonlinear Mechanics in Aerospace Engineering, AIAA Progress (1993).

[13] O. Hassan, K. Morgan and J. Peraire, An implicit explicit element method for high-speed flows, Int. J. Numer. Methods Engrg. 32(1) (1991) 183.

[14] O. Zienkiewicz and R. Codina, A general algorithm for compressible and incompressible flow—Part I. The split, characteristic-based scheme, Int. J. Numer. Methods Fluids 20 (1995) 869–885.

[15] K.T. Yoon and T.J. Chung, Three-dimensional mixed explicit–implicit Galerkin spectral element methods for high speed turbulent compressible flows, Comput. Methods Appl. Mech. Engrg. 135 (1996) 343–367.

[16] S.Y. Moon, K.T. Yoon and T.J. Chung, Numerical simulation of heat transfer in chemically reacting shock wave turbulent boundary layer interactions, Numer. Heat Trans. 30 (1996) Part A, 55–72.

[17] J.E. Carter, Numerical solutions of the Navier equations for the supersonic laminar flow over a two-dimensional compression corner, NASA TR-R-385 (1972).

[18] P. Ardonceau, D.H. Lee, T. Alziary de Roguefort and R. Goethals, Turbulence behavior in a shock wave/boundary layer interactions, AGARD CP-271, Paper No. 8 (1980).

[19] U. Ghia, K. Ghia and C.T. Shin, High resolution for incompressible flow using the Navier–Stokes equations and a multigrid method, J. Comput. Phys. 48 (1982) 387–411.